High Energy K_L Calibration at Belle II using Initial State Radiation

Lachlan Vaughan-Taylor
University of Sydney
Faculty of Science
Particle Physics

A thesis submitted to fulfil requirements for the degree of
Master of Philosophy
2019

Abstract

This thesis presents a feasibility study of a method for K_L calibration at the Belle II experiment, using initial state radiation (ISR) production of the $K_S K_L$ final state. By reconstructing the ISR photon, and the K_S and subtracting their energy-momentum 4-vectors from that of the known e^+e^- initial state, the 4-vector of the K_L may be determined.

Due to the loss of second order ISR photons and lost photon energy from incomplete electromagnetic shower reconstruction, a correction is applied to the photon energy.

The expected efficiency, after all of the appropriate selections to isolate signal events were applied, was found to be of order 1%. This corresponds to roughly 100 well-reconstructed events per fb^{-1} of integrated luminosity produced at Belle II, with the difference between the MC generated and reconstructed K_L energy found to be of the order of 5 MeV and with the angle between the truth and determined K_L vector found to be of the order 0.02 radians=1.1°. At this production rate, the currently available early Belle II data, which have an integrated luminosity of only $472pb^{-1}$, are likely not large enough for a meaningful K_L calibration, however, Belle II is expected to produce $50ab^{-1}$ of integrated luminosity. As Belle II produces more data this method will become more and more feasible.

Declaration

This is to certify that to the best of my knowledge, the content of this thesis is my own work. This thesis has not been submitted for any degree or other purposes. I certify that the intellectual content of this thesis is the product of my own work and that all the assistance received in preparing this thesis and sources have been acknowledged. Specific areas of outside contribution are as follows:

- The Belle II detector description found in Chapter 3 is primarily taken from the Belle II Technical Design Report [1].
- The Monte-Carlo data analysed in this thesis was produced by me using Phokhara [2]. Phokhara was modified by my primary supervisor, Kevin Varvell, to correctly pipe the $K_S K_L$ final state to the Geant4 [3] package.
- The Belle II analysis software framework (basf2) [4] was used by me to write analysis scripts for the purpose of interpreting the output of the simulation.
- Also analysed in this thesis is: a sample of Monte-Carlo $B\overline{B}$ events produced by the Belle II collaboration and stored at KEK, and a sample of real experimental data produced during the running of phase II of the Belle II experiment and processed by the Belle II collaboration.
- A simulation of $B \to J/\psi K_L$ decays produced by me using the EvtGen [5] package was also analysed.
- This thesis was edited with the help of my primary supervisor Kevin Varvell

The plots presented in this thesis, unless otherwise cited, were produced by me, using ROOT [6]. Post submission editing of text/titles in some plots was done by Lisa Collins.

Lachlan Vaughan-Taylor

Acknowledgements

Thanks go first and foremost to my primary supervisor Kevin Varvell, whose feedback and advice was invaluable to this analysis and thesis, and whose leadership has shaped the University of Sydney Particle Physics Group into the flourishing community that it is today. Thanks also go to my secondary supervisor Andrew Bakich, who often provided the insight, encouragement and alternative perspective needed to tackle a variety of problems encountered along the way.

Much of the work presented here was discussed in the Sydney-Adelaide Belle II conference meetings, where valuable feedback was provided by Bruce Yabsley, Frank Meier, Chia-Ling, Nadia Toutounji, Bernanda Telalovic Paul Jackson and Sophie Hollitt. Without their perspective, there are many problems I would likely have not solved.

This analysis was also presented in different stages to the Belle II collaboration performance group meeting, where I received valuable feedback. I was also counseled on the specific status of the relevant parts of Belle II reconstruction by two other Belle II performance group collaboration members: Torben Ferber and Jo-Frederick Krohn.

Thanks must also go to the University of Sydney School of Physics, in particular, to the Particle Physics Group, which exists as a welcoming environment for students that is as much a community as it is a workplace. Particular thanks to Carl Suster, who was always willing to help with coding questions and whose guidance was especially helpful in developing my own skills.

After my time spent here I consider it a second home and have forged friendships that I know will last long into the future.

Last and certainly not least, I must thank my family and friends, who provided unending love and support that kept me going through tough times and painful periods of writers block.

Thanks guys!

Contents

“In the beginning the Universe was created. This has made a lot of people very angry and been widely regarded as a bad move.”

— Douglas Adams

Chapter 1.

Introduction

In a sense, the field of particle physics spans back to the ancient Greeks. Around 400 BCE, Democritus' proposition of a smallest, indivisible particle, the atom, set the precedent for pursuit of small scale, fundamental physics. From that point in time onward, physicists have been narrowing in on smaller scales, but it wasn't until 1897 when J.J. Thomson measured the charge to mass ratio of the electron that what would become the field of particle physics was truly observing the fundamental, indivisible, building blocks of matter. What we now call the atom, once thought indivisible, has since proven to be comprised of smaller particles: protons, neutrons and electrons; the protons and neutrons, themselves, being comprised of quarks.

120 years after J.J. Thomson's discovery, the Standard Model (SM) of particle physics contains a zoo of particles, able to describe and predict nearly all subatomic particle interactions observed in experiment; and with striking precision, but the puzzle is not yet complete. There are still a range of problems for which the SM has no solution; one of these being an explanation for the matter antimatter asymmetry of the universe. To explain this, there needs to be a greater violation of the combined symmetry of charge-parity (CP) than that predicted by the SM.

To test CP violation, the Belle experiment (1999-2010) collided electrons and positrons at the rest energy of an $\Upsilon(4S)$ meson. The $\Upsilon(4S)$ decays to a pair of B mesons 96% of the time, allowing the probing of CP violation in B meson oscillations, whilst also providing a high luminosity dataset for the study of rare B decays. This experiment, in combination with BaBar, was able to discover CP violation in B systems and produce the current best measurements of CP violation in B meson mixing. [7]

Now, the upgraded Belle II experiment is set to produce roughly 40 times the luminosity, and 50 times the data of Belle. With this increase in data size, Belle II presents a fantastic opportunity for studying various rare decays that would not be seen in a detector with a lower data volume output. Recent hints that lepton universality may be violated could provide possible pathways to discovering new physics [8]. These decay channels will be explored with high statistics at Belle II.

Many important decay channels of the B meson include a K_L meson in the final state, for example, comparing the $B \to J/\psi K_L$ and $B \to J/\psi K_S$ channels is especially useful for measuring CP violation [9], but the Belle II detector's response to the K_L meson is far from ideal [1]. A proper calibration for the Belle II detector response to the K_L meson is needed as a step towards improving the CP violation measurements and the sensitivity to various rare decays at Belle II.

In this thesis a method of calibrating the Belle II detector's response to the K_L meson via the use of initial state radiation (ISR) production of the $K_L K_S$ final state is presented and a Monte-Carlo (MC) simulation of this channel is studied. The following chapter outlines the theoretical background of the Standard Model (SM) of particle physics, the motivation for the Belle II experiment and the background of ISR as a tool for studying low mass resonances. The 3rd chapter outlines the necessary technical information relating to the SuperKEKB accelerator and Belle II experiment, and then provides a description of the different forms of beam background seen at Belle II. The 4th chapter includes the details of the software used to produce the simulation of the ISR channel and describes the observed kinematics of the MC truth particles. In the 5th chapter, the expected efficiency and accuracy of determination of the properties of the K_L for a variety of cuts are determined. Then, a method of countering efficiency losses and correcting the determined K_L energy-momentum 4-vector is outlined. Chapter 6 concludes this thesis with the expected accuracy of K_L energy determination and the number of expected well-reconstructed events for calibration per unit of integrated luminosity.

Chapter 2.

Standard Model Overview

The current reigning theory of particle physics is the Standard Model (SM), which, since its inception, has accurately predicted (almost) all emergent phenomena observed in particle physics experiments. The SM describes the interaction between subatomic point-like particles and the fundamental forces; the electromagnetic force, the strong nuclear force and the weak nuclear force. The SM currently does not incorporate gravitational interactions as there is no current accepted quantum theory of gravity. The SM is a quantum field theory describing fundamental, point like particles, with no observed internal structure, as quantizations of fields. The interactions of the SM are described by the gauge group $\mathrm{SU}(3)_C \times \mathrm{SU}(2)_L \times \mathrm{U}(1)_Y$. The $\mathrm{SU}(3)_C$ component represents the strong force colour symmetry, the $\mathrm{SU}(2)_L$, the weak isopspin symmetry, and the $\mathrm{U}(1)_Y$, weak hyper-charge. The L in $\mathrm{SU}(2)_L$ indicates that the weak force only couples to left handed particles. The SM contains 12 Fermion fields, the quantization of which results in the six quarks and six leptons. From the quarks and leptons we can construct all visible matter in the observable universe. Fermions have half integer spin and obey Fermi-Dirac statistics, and as such, will obey Pauli's exclusion principle.

2.1. Fermions

The Fermions are classified based on how they interact with the fundamental forces. Based on their interaction with the $\mathrm{SU}(3)_C$ strong nuclear force, the Fermions are divided into two categories: the leptons and the quarks. The quarks feel the strong nuclear force, whereas the leptons do not. Both the quarks and leptons are divided into three generations of $\mathrm{SU}(2)_L$ weak isopin doublets. Each Fermion has an associated anti-particle, that is identical but with opposite sign charge and flavour quantum numbers.

2.1.1. Leptons

The three left-handed lepton generations are the electron, muon and tau, paired with their corresponding neutrino (Equation 2.1), each particle in the doublet carries lepton number of the corresponding flavour i.e. an electron and an electron neutrino have electron number of 1, a muon and muon neutrino have muon number of 1 and a tau and tau neutrino have tau number of 1. The electron, muon and tau all carry negative integer charge. Their masses are 0.510 MeV, 106 MeV and 1780 MeV respectively. The right-handed leptons do not interact via the weak force so form right-handed weak isospin singlets (Equation 2.2).

One of the assumptions of the SM is that aside from their masses, the leptons behave identically [8]. This is called lepton universality. There have recently been measurements that challenge lepton universality. The current global average measurement of the ratio of the decay of a B meson to a D^0 or D^* meson with an associated τ compared with an electron or muon is 3.78σ away from the SM prediction [10]. If these results are confirmed with more data, then this is a strong indication of new physics.

$$\begin{pmatrix} \nu_e \\ e^- \end{pmatrix}_L, \begin{pmatrix} \nu_\mu \\ \mu^- \end{pmatrix}_L, \begin{pmatrix} \nu_\tau \\ \tau^- \end{pmatrix}_L \tag{2.1}$$

$$(e^-)_R, (\mu^-)_R, (\tau^-)_R, (\nu_e)_R, (\nu_\mu)_R, (\nu_\tau)_R \tag{2.2}$$

2.1.2. Quarks

The quarks, which feel the strong force, are divided into three $\mathrm{SU}(2)_L$ doublets, each containing one up type and one down type quark. The quarks carry a $\frac{1}{3}$ integer of the magnitude of the electron charge. The up type carrying positive $\frac{2}{3}$ and the down type carrying negative $\frac{1}{3}$. The proton is comprised of two up quarks and one down quark, resulting in a charge sum of 1; whereas the neutron is comprised of two down quarks and one up quark, resulting in charge sum of 0.

The three generations of quarks are the down and up quark, the strange and charm quark and the bottom and top quark, increasing in mass in that order (Equation 2.3). The top quark has such a large mass that it decays before hadronising.

$$\begin{pmatrix} u \\ d \end{pmatrix}_L, \begin{pmatrix} c \\ s \end{pmatrix}_L, \begin{pmatrix} t \\ b \end{pmatrix}_L \tag{2.3}$$

As with the leptons, the right-handed quarks do not interact via the weak force so form right-handed, weak isospin singlets (Equation 2.4).

$$u_R, d_R, c_R, s_R, t_R, b_R \tag{2.4}$$

Bound states of quarks are called hadrons, 3 quark states are baryons and bound states of a quark and an anti-quark are mesons. Due to the nature of the gluon fields between them, quarks have never been directly observed outside of bound states. This is called quark confinement.

2.2. Symmetries

All of the forces and laws of conservation in the SM are a result of fundamental symmetries in nature, specifically a symmetry in the SM Lagrangian. A Lagrangian describes the dynamics of a system. It is a function of space-time coordinates and space-time derivatives, equal to the difference between the kinetic energy and potential energy of a system. The relationship between symmetry and conserved quantities was first shown by Emmy Noether in 1918 [11]. Noether's theorem states that for any transformation of a Lagrangian that leaves the Lagrangian invariant, there exists a corresponding conserved quantity. By requiring that the choice of coordinate system does not affect the underlying physics, true conservation laws are a natural consequence. The SM Lagrangian has 10 space-time symmetries, the combination of which form the Poincaré group. This is comprised of the translations in space-time, which are responsible for energy-momentum conservation, and the sub-group of the Poincaré group, the Lorentz group, consisting of 3 rotational symmetries and 3 boosts. Invariance under this group leads to relativistic invariance.

2.2.1. Gauge Symmetry

In 1928 Paul Dirac derived an equation to re-express the Schrödinger equation in a relativistic framework.

$$(i\gamma^{\mu}\partial_{\mu} - m)\psi = 0 \tag{2.5}$$

ψ is a Fermion field of mass m, γ^{μ} is the set of gamma matrices and ∂_{μ} is the space-time derivative. The Dirac equation (Equation 2.5) was able to describe the behaviour of all Fermions, and predicted the existence of anti-matter: the partner of each particle, possessing opposite charge and flavour quantum numbers. Equation 2.6 is the Dirac term in the SM Lagrangian.

$$\mathcal{L}_{Dirac} = \overline{\psi}(i\gamma^{\mu}\partial_{\mu} - m)\psi \tag{2.6}$$

Equation 2.7 shows a U(1) phase transformation of ψ, where θ is any real number.

$$\psi \rightarrow e^{i\theta}\psi \tag{2.7}$$

This is a global phase transformation. If θ depends on x, a space-time coordinate, then this becomes a local U(1) phase transformation (Equation 2.8).

$$\psi \rightarrow e^{i\theta(x)}\psi \tag{2.8}$$

If the Dirac term is required to be invariant under local U(1) phase transformations, then it requires the addition of a new gauge field, A_{μ} , to the Lagrangian. Gauge invariance is preserved by replacing the derivatives in the Lagrangian with covariant derivatives (Equation 2.9).

$$\partial_{\mu} \rightarrow D_{\mu} = \partial_{\mu} + iqA_{\mu} \tag{2.9}$$

q is the charge of the Fermion and A_{μ} is the electromagnetic potential.

The quantization of this new gauge field is in fact, the photon, the gauge boson associated with electromagnetic interactions. Elegantly, in an analogous process to requiring U(1) electromagnetic local gauge invariance, by requiring invariance under SU(2) and SU(3) local gauge transformations, the SM generates the weak interaction and strong interaction respectively. The SU(2) transformation requires the addition of 3 new gauge fields. These mix with the U(1) hypercharge group to generate the massive $W^{\pm}$ and Z^0 bosons and the massless photon. The SU(3) symmetry results in 8 gauge fields. These are 8 different gluon fields which describe the strong nuclear force.

2.3. Forces and Exchange Bosons

In the SM framework, forces are described by interactions. In an interaction, an initial state with some momentum transitions to a final state with a different momentum. This may also involve changes in the number and identity of particles through annihilation and creation. The framework for these particle interactions in the SM takes the form of the exchange of a mediating force carrying particle, a boson; the integral spin, quantization of the vector fields produced by requiring local gauge invariance. The interactions of SM are all predicted using the SM Lagrangian, an equation of fields, their derivatives and potentials. Interaction terms in the SM Lagrangian represent the coupling of particles to each other. This is best understood with the use of a Feynman diagram.

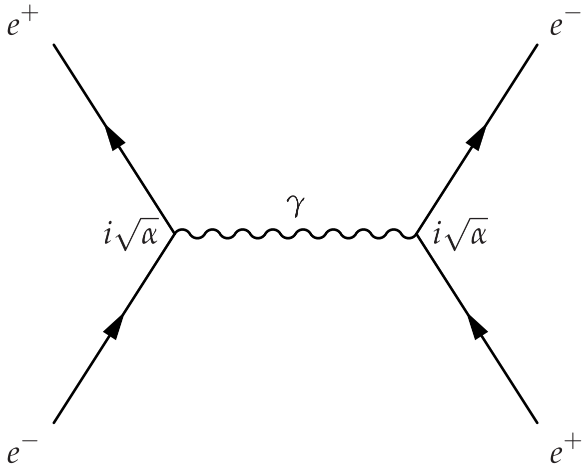

Figure 2.1.: A Feynman diagram of an electron positron electromagnetic interaction

2.3.1. Electromagnetism

Figure 2.1 shows the Feynman diagram that represents the electromagnetic interaction between an electron and a positron. The electron and positron have some initial momenta and after an annihilation into an intermediate "virtual" photon state, they are recreated in a final state with different momenta. The strength of the quantum electrodynamic coupling at the vertices is $i\sqrt{\alpha}$, where α is the fine structure constant. This is one of the experimentally determined input parameters of the SM.

Each Feynman diagram represents a term in an expansion of the S-matrix of QFT that contributes to the complex sum of transition amplitudes between initial and final states. The probability of a given process occurring is this amplitude integrated over the possible momentum phase space, then squared.

2.3.2. The Strong Force

The Strong Force was first used to describe the interaction between nucleons that holds the nucleus together. For the nucleus to be stable, the inter-nucleon force must be orders of magnitude stronger than the electromagnetic force repelling the protons at a small distance, hence the name. In 1935 Hideki Yukawa postulated the existence of an exchange boson for the strong nuclear force, dubbed the meson [12].

The following year, cosmic rays with a mass close to Yukawa's prediction were discovered, and initially thought to be Yukawa's strong meson. The prediction was however, incongruous with the lifetime and strength of the nucleon interaction of these newly discovered "μ mesons" [13]. It was not until 1947 that it was determined that these cosmic rays were comprised of both the muon (a heavy lepton) and the true Yukawa meson, the pion [14].

The exchange of pions describes the residual strong force, the collective effect of the force between quarks. The mediator of the strong force between quarks is the gluon, and the strong force analogue of electric charge is the colour charge. Analogous to a positive and a negative charge forming a neutral U(1) bound state, the addition of the three colour charges: red, green and blue, results in an SU(3) colour singlet state.

The quarks each carry a colour charge and the anti-quarks carry anti-colour charge. The 8 different gluon fields that are a result of the SU(3) gauge symmetry can be

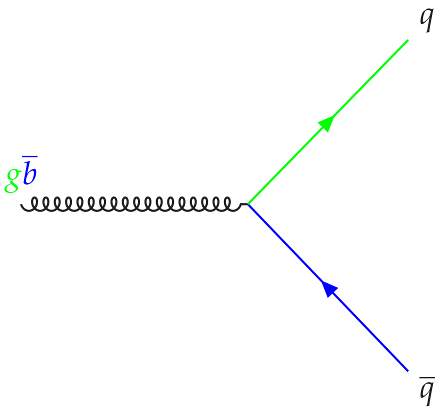

Figure 2.2.: A green anti-blue quark coupling to a quark anti quark pair.

represented as the following colour configurations: $r\overline{g}$, $r\overline{b}$, $g\overline{b}$, $g\overline{r}$, $b\overline{g}$, $b\overline{r}$, $\frac{1}{\sqrt{2}}(r\overline{r}+g\overline{g})$, $\frac{1}{\sqrt{6}}(r\overline{r}+g\overline{g}-2b\overline{b})$. Figure 2.2 shows the Feynman diagram of a strong coupling of a green anti-blue gluon to two quarks, conserving colour at the vertex.

A hadron must form a neutral colour singlet. For this reason nature produces hadrons of either three quarks in a baryon, three antiquarks in an anti-baryon or the pairing of a quark and an anti quark in a meson. The combination of red, green and blue is a neutral colour singlet and likewise the superposition of all possible colour anti-colour pairings is also a neutral colour singlet (equation 2.10).

$$\frac{1}{\sqrt{3}}(r\overline{r}+g\overline{g}+b\overline{b}) \tag{2.10}$$

A quark may swap colour with another quark in a hadron via the exchange of a gluon. Colour is then conserved at each vertex and the colour singlet of the hadron is preserved. The Feynman diagram representing this process between quarks in a proton is displayed in Figure 2.3. In this example a blue quark swaps colour with a red quark via the exchange of a $r\overline{b}$ gluon. The superposition of all of these possible exchanges in a hadron is the gluon field that holds the hadron together.

The fact that gluons possess a colour charge means that gluons may couple to one another. This effect leads to the formation of gluon loops. At greater distances the quark-anti-quark interaction will allow more loops to be able to form, which results in an increasing strength with distance (see Figure 2.4). This also applies to quarks in a baryon.

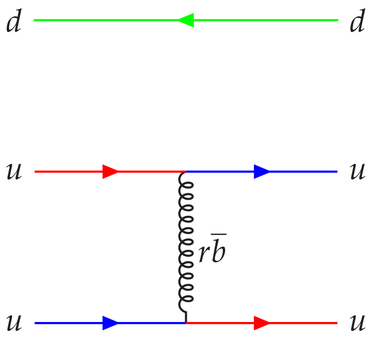

Figure 2.3.: Quark colour changing via the exchange of a red-anti-blue gluon.

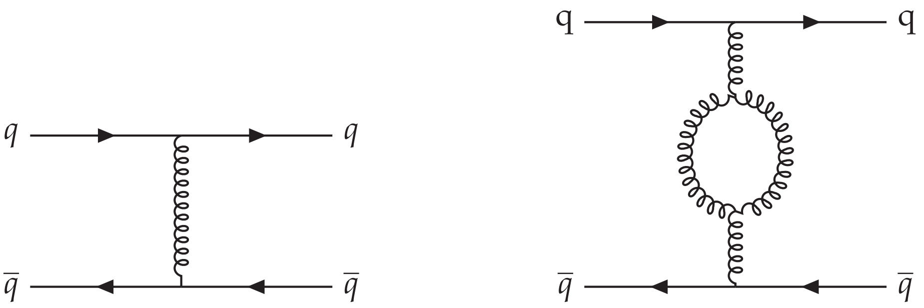

(a) At close range.

(b) At a distance.

Figure 2.4.: The quark-anti-quark strong interaction. As distance increases, more gluon loops can form.

This effect means that the chromodynamic potential between two quarks bound in a hadron, effectively contains a linear term. This is equivalent to an attractive force of roughly 16 tonnes at all distances [15]. For this reason quarks have never been observed outside of a bound hadron. As quarks are stretched further apart to greater distances, more energy is added to the colour field between them. At some point it becomes energetically favourable to produce a quark anti-quark pair from that field, which will result in new, separate, colour singlets being formed.

2.3.3. Electro-Weak Mixing

The electromagnetic force and the weak force are considered separately at low temperatures, but at higher energies, such as those seen during the early universe, they are unified into one electro-weak force, governed by the $SU(2)_L \times U(1)_Y$ group. Requiring $SU(2)_L \times U(1)_Y$ local gauge symmetry generates 4 fields. An isotriplet of vector bosons, W^1, W^2, W^3, from the weak isospin SU(2)$_L$, and an isosinglet, B, from the weak hypercharge U(1)$_Y$.

The electro-weak fields are expressed as linear combinations of the W and B fields as the W^+, the W^-, the Z^0 and the photon field, γ.

$$W^{\pm} = \frac{1}{\sqrt{2}}(W^1 \mp iW^2)$$

$$\gamma = B^0 \cos(\theta_W) + W^3 \sin(\theta_W)$$

$$Z^0 = -B^0 \sin(\theta_W) + W^3 \cos(\theta_W)$$

The angle θ_W is referred to as the weak mixing angle and is one of the input parameters of the SM. To first order, $\cos(\theta_W) = \frac{m_W}{m_z}$ where m_W and m_Z are the masses of the W and Z bosons respectively.

Requiring local gauge invariance leads to the requirement that these bosons are massless. While this holds true for the photon, based on the experimentally observed strength and short range of the weak force, the $W^{\pm}$ and Z^0 bosons must have mass.

The Higgs mechanism was an addition to the SM that was able to explain this. A doublet of complex scalar fields was added to the SM Lagrangian. The non-zero vacuum state of the field acquires some complex phase at low energies, which leads to electro-weak symmetry breaking. This is able to generate mass whilst preserving local gauge invariance. This mechanism introduces four, spin zero, scalar boson fields: 1 massive, the Higgs field, and three massless Goldstone bosons. By choosing a particular gauge transformation, the Lagrangian can be written with the Goldstone bosons reinterpreted as longitudinal polarization states of the weak gauge bosons. This leaves only the massive Higgs. In this gauge, the weak bosons acquire a mass term through coupling with the Higgs, while the photon remains massless.

The Z^0 boson and the charged W^+ an W^- bosons couple to both quarks and leptons. In 1983, CERN discovered high energy electrons with large missing energy in $p\overline{p}$ collisions at the Super Proton Synchrotron (which now feeds into the Large Hadron Collider). These events were $W^{\pm} \rightarrow e^{\pm}\nu_e$ decays, the first direct observation of the massive W boson [16] [17]. The massive Higgs boson was then discovered at the LHC in 2012 [18] [19].

2.4. CP Symmetry and Baryogenesis

2.4.1. CP Symmetry

The symmetries mentioned above are continuous symmetries, but there also exists a set of discrete symmetries, such as charge conjugation (C) and parity (P). Charge conjugation is invariance under the swapping of all particles for the equivalent antiparticle; while parity is a reflection through the origin of spatial coordinates (Equation 2.11).

$$\begin{pmatrix} x \\ y \\ z \end{pmatrix} \overset{\hat{\mathrm{P}}}{\to} \begin{pmatrix} -x \\ -y \\ -z \end{pmatrix} \tag{2.11}$$

The quantum numbers C and P characterize a system's behaviour under these transformations and where these symmetries (or their combined symmetry) hold, the quantum numbers C and P are conserved.

2.4.2. The Sakharov Conditions

One of the reasons there is such interest in CP violation is that the matter anti-matter asymmetry of the universe is expected to be closely related to CP violation during the early universe. It is natural to assume equal amounts of matter and antimatter were produced by the Big Bang, however, assuming CP symmetry, the two would then collide and annihilate in equal proportions, leaving no matter or antimatter left over, from which the matter dominated universe we see could form. Given this is not what we observe i.e. we exist [20], there must be some source of asymmetry that would lead to the preference of matter over antimatter. The process whereby the matter anti-matter imbalance is generated is called "baryogenesis".

In 1967 Andrei Sakharov established three conditions necessary for baryogenesis [21]:

1. A process for Baryon number violation.
2. CP asymmetry.
3. Interactions outside of thermal equilibrium.

To generate an asymmetry between baryons and anti-baryons, a baryon number violating process is required, however, without CP violation the CP conjugate process will occur with the same frequency, reversing the generated asymmetry. Current models of inflation (rapid expansion of space in early universe) are a candidate for a period of thermal non-equilibrium.

2.4.3. Baryon Number Violation

Charge conservation is based on the local U(1) gauge invariance of the electromagnetic field. The electron's stability is guaranteed by charge conservation, the electron being the lightest charged particle. Baryon number holds very well in nature, but is a global symmetry, not a true local symmetry. Many leading theories offer sources of baryon number violation [22]. For example, the SM is able to predict baryon number violation via nonperturbative quantum tunnelling between different electroweak vacuum states [23]. During the early universe, these fluctuations can be caused by thermal fluctuations and so are not suppressed [24]. This leads to baryon number violation during the thermal non-equilibrium period of early universe inflation.

This leaves CP violation.

2.5. CP Violation

2.5.1. Strong CP Violation

The SM has two theoretical sources of CP violation. The first of these is strong CP violation. The pseudoscalar nature of the QCD Lagrangian (2.12) makes it P and CP violating. [25]

$$\mathcal{L}_{CP,Strong} = \theta \frac{\alpha_S}{8\pi} G^{\mu\nu,a} \tilde{G}^{a}_{\mu\nu} \tag{2.12}$$

$G^{\mu\nu,a}$ is the gluon field strength tensor (a is the ath gluon field, summing from $a = 1$ to 8) and θ is the experimentally determined input parameter for the strength of strong CP violation in the SM. This term in the Lagrangian will however, have a great effect on the neutron electric dipole moment. The neutron dipole moment has an experimentally determined upper limit of $d_N < 0.29 \times 10^{-25}$ e cm [26]. There is currently no theoretical explanation for why d_N, and by extension, strong CP violation is so small. This limit sets a harsh constraint on the level of strong CP violation (θ) and as such, it is, for practical purposes, equal to 0 [25].

2.5.2. Weak Sector CP violation

The second source of SM CP violation comes from the charged current interaction term of the weak sector (Equation 2.13). The Feynman diagram representing the charged weak current term is shown in Figure 2.5.

$$\mathcal{L}_{CP,Weak} = \left(\bar{u}_L \bar{c}_L \bar{t}_L\right) V_{CKM} \gamma^{\mu} \begin{pmatrix} d_L \\ s_L \\ b_L \end{pmatrix} W^{+}_{\mu} \xrightarrow{\widehat{CP}} \left(\bar{d}_L \bar{s}_L \bar{b}_L\right) V^{T}_{CKM} \gamma^{\mu} \begin{pmatrix} u_L \\ c_L \\ t_L \end{pmatrix} W^{-}_{\mu} \tag{2.13}$$

V_{CKM} is the CKM matrix (Equation 2.14), u_L,c_L,t_L,d_L,s_L and b_L, are the left handed quark fields and W^{-}_{μ} and W^{+}_{μ} are the W boson fields.

$$V_{CKM} = \begin{pmatrix} V_{ud} & V_{us} & V_{ub} \\ V_{cd} & V_{cs} & V_{cb} \\ V_{td} & V_{ts} & V_{tb} \end{pmatrix} \tag{2.14}$$

For this term to be CP invariant, it is required that $V^{\dagger}_{CKM} = V^{T}_{CKM}$ (this equivalent to requiring real entries).

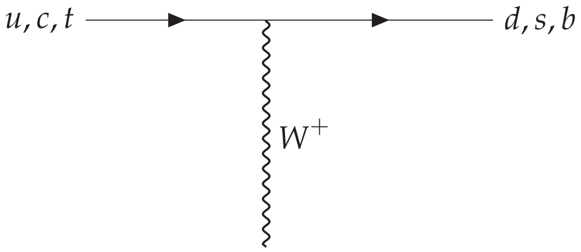

Figure 2.5.: Feynman diagram of a charged current interaction.

Each element of the CKM matrix (Equation 2.14) describes the coupling of an up type quark to a down type quark through a W boson (Figure 2.5). The respective strength of this coupling is an input parameter of the SM, which is determined by experiment. The condition of unitarity allows the CKM matrix to be reduced from nine complex parameters, to four: three rotations and a complex CP-violating phase.

$$V_{ud}V_{ub}^* + V_{cd}V_{cb}^* + V_{td}V_{tb}^* = 0 \tag{2.15}$$

Equation 2.15 is one of the equations resulting from the unitarity condition. By dividing equation 2.15 by $V_{cd}V_{cb}^*$, the unitarity condition can be expressed as a triangle in the complex plane with a base of unit length (see Figure 2.6), where η characterizes the amount of SM CP violation.

$$\bar{\rho} + i\bar{\eta} = -\frac{V_{ud}V_{ub}^*}{V_{cd}V_{cb}^*} \tag{2.16}$$

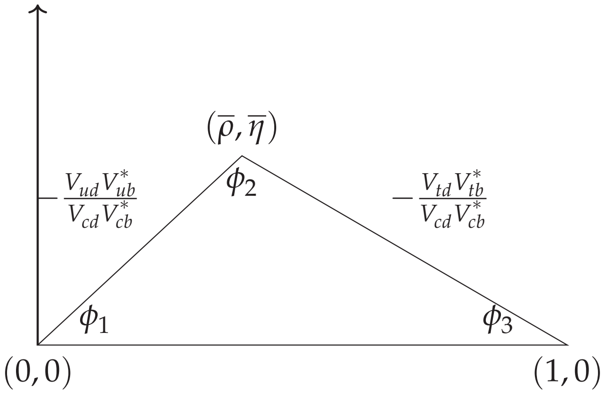

Figure 2.6.: The Unitary Triangle

If the angles of this 'unitary triangle' were found not to sum to π, it would imply breaking of unitarity. In the SM, the CKM matrix is unitary, so if breaking of unitarity were found experimentally, then there must be some beyond SM contributions to the experimental measurement of CP violation.

The simplest form of weak CP violation is direct CP violation, which presents itself as a difference between the rates of a decay channel, $X \to f$, and its conjugate process $\overline{X} \to \overline{f}$, where X is some initial state and f is some final state [27]. There are, however, other ways that SM weak sector CP violation presents itself.

2.5.3. Weak Mixing in Neutral Mesons

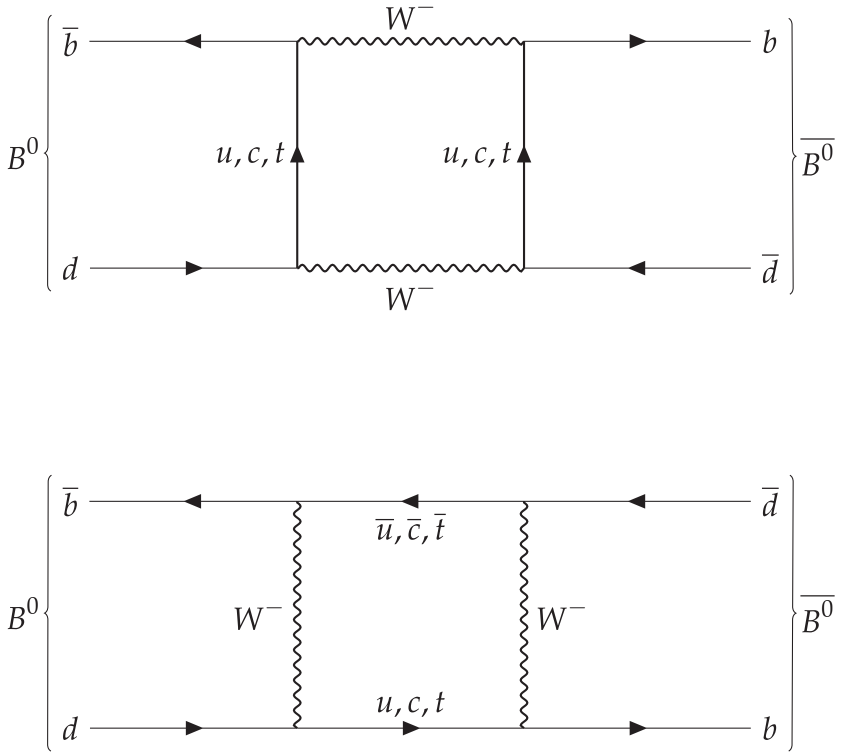

Figure 2.7.: Feynman diagrams of B meson mixing

Figure 2.7 shows the Feynman diagrams for the process of neutral B meson mixing. Neutral mixing can occur only for mesons containing open flavour (not $q\overline{q}$, where quark and anti-quark are the same flavour, as these states have identical anti-particles) and allows these neutral mesons to mix into their antiparticle. Meson mixing can occur in B^0, D^0, K^0 and B_S^0 mesons. The coupling strengths of the vertices in the diagrams that represent these processes are proportional to the corresponding elements of the

CKM matrix. CP violation in mixing arises when the mass eigenstates are not an equal mixture of the flavour eigenstates [27], CP violation arising from mixing is referred to as indirect CP violation. CP violation in neutral B meson mixing can be observed as a difference in the rates of the transitions $B \to \overline{B}$ and $\overline{B} \to B$ [27].

Around the turn of the century, to measure CP violation in meson mixing, two B factories were built, the BaBAR experiment, fed by the PEP-II collider at the SLAC National Accelerator Laboratory and Belle fed by the KEKB collider at KEK. These were particle collider experiments designed to produce pairs of B mesons en masse.

2.5.4. CP violation in $B \to J/\psi K_S$ and $B \to J/\psi K_L$ Decays

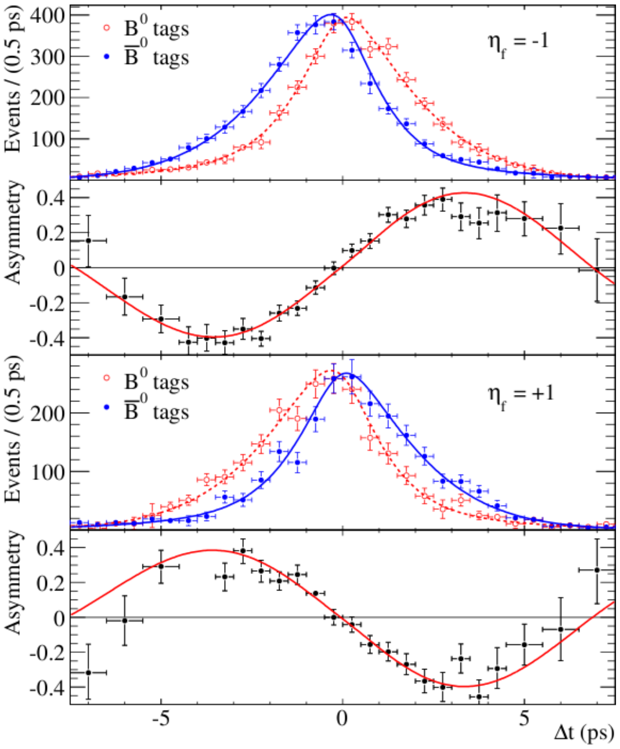

Figure 2.8.: The time difference between the first B decay and the second B decay at Belle. Events where the B^0 decays first are in red and events where the $\overline{B^0}$ decays first are in blue. The plots labelled η_f=-1 correspond to decays to CP=-1 eigenstates (e.g. $B \to J/\psi K_S$) The plots labelled η_f=+1 correspond to decays to the CP=+1 eigenstate $B \to J/\psi K_L$ [25]

CP violation may also occur via interference between direct decays and those where mixing occurs. When both a B and $\overline{B}$ can decay into the same final state then there can be interference between $B \to f$ and $B \to \overline{B} \to f$. This is the case for both the $B \to J/\psi K_S$ and the $B \to J/\psi K_L$ decays. There is close to no direct CP violation in the $B^0 \to J/\psi(K_S/K_L)$ decay so the interference of $B^0 \to J/\psi(K_S/K_L)$ and $B^0 \to \overline{B^0} \to J/\psi(K_S/K_L)$ results in a CP violating time difference between the decay time of B^0 and $\overline{B}^0$ [28]. This time difference was used to measure one of the interior angles of the unitary triangle, ϕ_1. Defined as $\phi_1 = \pi - arg(\frac{V_{tb}^* V_{td}}{V_{cb}^* V_{cd}})$, the size of the measurement of $\sin(2\phi_1)$ indicates the amount of CP violation.

The B factories, Belle and BaBar, were able to perform a measurement of $\sin(2\phi_1)$ in a range of B channels, including $B \to J/\psi\ K_S$ and $B \to J/\psi\ K_L$ [9] [29]. Figure 2.8 shows the CP violation plots from Belle. The current measurements of CP violation are consistent with SM predictions [28], however, the SM predictions are not enough to satisfy the requirements for early universe baryogenesis.

The $B \to J/\psi(K_S/K_L)$ channel is often referred to as the golden channel for CP violation. Belle II is set to produce a much larger data set in the coming years which will be used to repeat the analysis of this channel with higher statistics and will also be used to measure other decay channels that will likely produce K_L mesons. Knowing this, a method of calibrating the Belle II detector response to K_L is needed. The Initial State Radiation production of a $K_S K_L$ final state is a promising avenue for producing a clean sample of K_L for which the 4-vector can be known, and therefore used to calibrate the detectors response to the K_L meson.

2.6. Initial State Radiation

2.6.1. Radiative Corrections

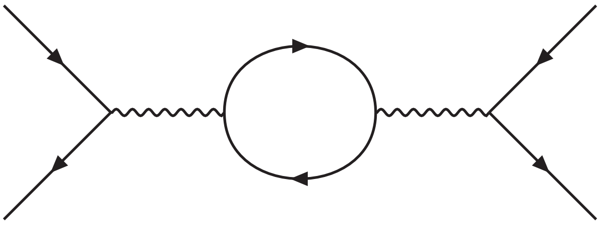

Figure 2.9.: A Feynman diagram containing a Fermion loop representing a higher order QED process.

Figure 2.9 shows the Feynman diagram for a QED loop process. This represents higher order terms in the QED amplitude. In this diagram the virtual photon couples to a virtual fermion loop. The strength of the QED coupling, $i\sqrt{\alpha}$, has a magnitude smaller than 1, meaning as more vertices are added to a Feynman diagram, the less that diagram contributes to the final amplitude. Higher-order QED diagrams are suppressed by powers of α. These loop diagrams are referred to as radiative corrections.

2.6.2. Low Mass Spectroscopy Using Initial State Radiation

In 1968, when calculating the higher-order, radiative corrections to electron-positron collider cross sections, V.N. Baier and V.S.Fadin [30] asserted that since the radiative corrections contained significant contributions from real photons, produced collinear with the incident collision beams, these events could be used to examine properties of resonances lower than the centre-of-mass-system (CMS) energy of the collider. These real photons emitted from the initial state are referred to as initial state radiation (ISR) photons.

With the advent of high luminosity e^+e^- B factories, such as Belle, BaBar and CLEO-III, this became a field of its own, as it allowed the study of lower mass resonances, without the need for changing the beam configuration. Figure 2.10 shows the generic Feynman diagrams for an ISR process of two colliding fermions emitting an initial state photon from either fermion, where V is an intermediate resonance with the same quantum numbers as the photon, and f is some final state.

Figure 2.10.: Feynman diagram of a generic ISR process. [31]

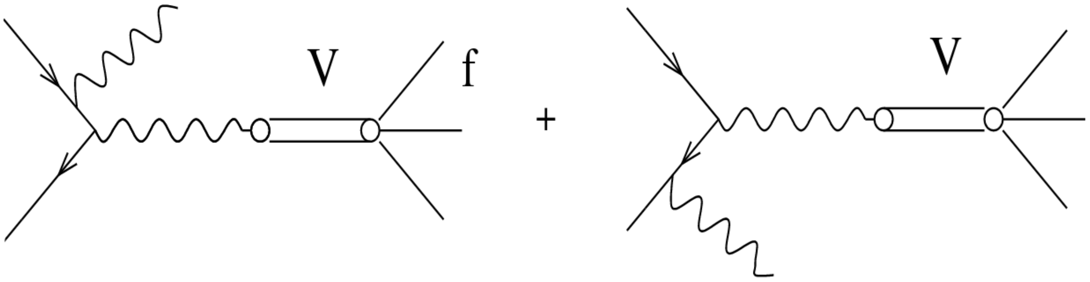

ISR events have already been effectively used to study low energy cross sections with high luminosity e^+e^- colliders [32] [33]. In 1999, M. Benayoun et al. (Ref. [31])

presented a prediction of the ISR cross sections for different resonances at B factories. The ISR production of the ϕ meson was used for determination of K_L efficiency of the BaBar detector [32], which is the justification for the same process to be used to study the behaviour of K_L at Belle II. The feasibility of using the same process for K_L calibration of the Belle detector was discussed in early stages of the Belle experiment but was never pursued.

ISR is not limited to single photon emission. A higher order version of the same process may occur, with the emission of two ISR photons, one from each incoming particle or two from a single particle. Higher order ISR also includes events where one of the two ISR photons is a virtual photon that is then reabsorbed by the final state fermions. These single real photon, higher-order processes contribute to a correction in the total cross section, but behave identically to first-order processes kinematically.

2.6.3. ISR $K_S K_L$ Production at Belle II

The beams of the Belle II detector are tuned to a CMS energy of 10.58 GeV, the mass of the $\Upsilon(4S)$ meson, so as to maximize the cross section for its production. At this CMS energy, the ϕ meson resonance, the dominant resonance for the $K_S K_L$ final state which will be studied in this thesis, is expected to be produced with a cross section of $\sigma = (0.0241 \pm 0.0003) nb$ [34], which is roughly one ϕ meson produced for every 40 $\Upsilon(4S)$ events.

Chapter 3.

The Belle II experiment

This chapter will outline the motivation and necessary technical background of the Belle II experiment. This will in turn motivate the K_L calibration proposed in this thesis. Belle II is an upgrade to the Belle experiment that ran from 1999-2010. Belle II began first data taking collisions in April of 2018. The design features of Belle II and SuperKEKB described here are taken from the Belle II technical design report [1].

3.1. Belle II Motivation

The Belle experiment was designed to produce a large sample of $B\overline{B}$ meson pairs. This was done by tuning the CMS energy of e^+e^- collisions to the rest mass of the $\Upsilon(4S)$, as the $\Upsilon(4S)$ will decay to a pair of B mesons 96% of the time. Figure 3.1 shows how the cross section for meson production from e^+e^- evolves with CMS energy. It can be seen that the cross section of meson production greatly increases at the CMS energy of a meson's rest mass. As such the Belle II chosen CMS energy is the $\Upsilon(4S)$ rest mass. The CMS frame is the rest frame of the $\Upsilon(4S)$ (or the equivalent frame for events where an $\Upsilon(4S)$ is not produced).

3.1.1. CP violation

The primary purpose of the Belle experiment was to measure CP violation with a large data set of $B\overline{B}$ decays. This (in conjunction with the BaBar data) successfully provided the highest precision measurement of CP violation in B mixing to date. The Belle II experiment, having just finished the so called "phase II" of its initial run at the time of

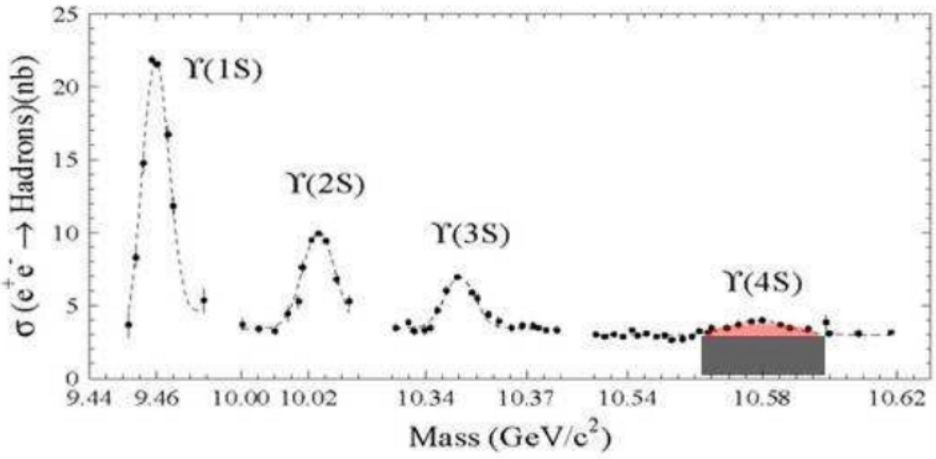

Figure 3.1.: The annihilation cross section of e^+e^- to hadrons over the range of the Υ ($b\bar{b}$) resonances [35]. The region where the $\Upsilon(4S)$ is produced is highlighted in red. The darker shading indicates the level of continuum background (annihilation to other states) in this region.

writing of this thesis, will essentially function the same as Belle but with much higher luminosity. The total integrated luminosity for Belle was 1 ab^{-1} of data, whereas Belle II is expected to collect 50 ab^{-1}. This will allow Belle II to provide data for a much higher precision measurement of CP violation in B mixing.

3.1.2. Rare Decays

The high luminosity of the Belle II experiment also makes it perfect for studying rare B decays, that in a lower luminosity collider, have too low a number of events to perform a proper analysis. For example, there is currently particular interest in lepton universality. The SM predicts no preference in which lepton a given decay path would favour, other than suppression from kinematics due to differing lepton mass. Studies into a variety of lepton channels have shown potential evidence for violation of lepton universality [8]. As mentioned previously, the current measurement of the ratio of B mesons decaying to D^0 or D^* mesons with an associated tau, versus decays with associated muons or electrons is 3.78σ away from the SM prediction [10]. If lepton universality is violated, it could point to new physics beyond the SM. There is currently not enough data to determine if this anomaly is reflective of the underlying physics or the result of a statistical fluctuation. 5σ is generally considered to be the required interval for accepting an anomaly as not the result of statistical fluctuations. Belle

II will likely provide the data required to make conclusive statements about these anomalies.

3.2. SuperKEKB

SuperKEKB is an upgrade to the KEKB accelerator in Tsukuba, Japan. KEKB was the ring accelerator that provided the electron and positron beams for the Belle experiment. The experiment collides a 7 GeV electron beam with a 4 GeV positron beam. The adoption of a "nano beam scheme", which aims to reduce the longitudinal size of the beam overlap at the interaction point (IP) and thereby reduce the vertical beta function, will allow for a much higher luminosity at Belle II.

The bunch length at SuperKek-B is 5-6 mm, with a vertical beta function of 32/0.27 mm for the positron beam and 25/0.30 mm for the electron beam. On average each positron bunch contains 9.04 positrons and each electron bunch contains 6.53 electrons.

Background events can be caused by elastic collisions of the beams or the beams interacting with detector elements, gas or material in the beam pipe. When the beams misbehave and produce extra background signals, this is referred to as beam background. The beam current is doubled from KEKB to SuperKEKB, which, whilst dramatically increasing the beam background, will allow Belle II to reach the goal of an instantaneous luminosity of $8 \times 10^{35} cm^{-2} s^{-1}$, 50 times that seen at Belle.

3.3. Belle II Detector

Belle II consists of multiple, compartmentalized detector elements in a longitudinal, 1.5 Tesla magnetic field. Figure 3.2 shows a cross section of the elements of Belle II detector. The coordinate system used in this thesis defines the positive z direction to be the Belle II electron beam axis (the 7 GeV beam). θ is the polar angle with respect to the forward z direction and ϕ is the azimuthal angle. Given the radial symmetry of the Belle II detector elements, and the collinear emission of ISR with the beam line, focus will be on the θ distribution. When something is described as being forward, unless otherwise stated, this will be in reference to the positive z direction. The Interaction Point (IP) is defined to be the collision point of the beams at $(x, y, z) = (0, 0, 0)$. When discussing the vector of a particle, this refers to its energy momentum 4-vector: $p = (E, p_x, p_y, p_z)$

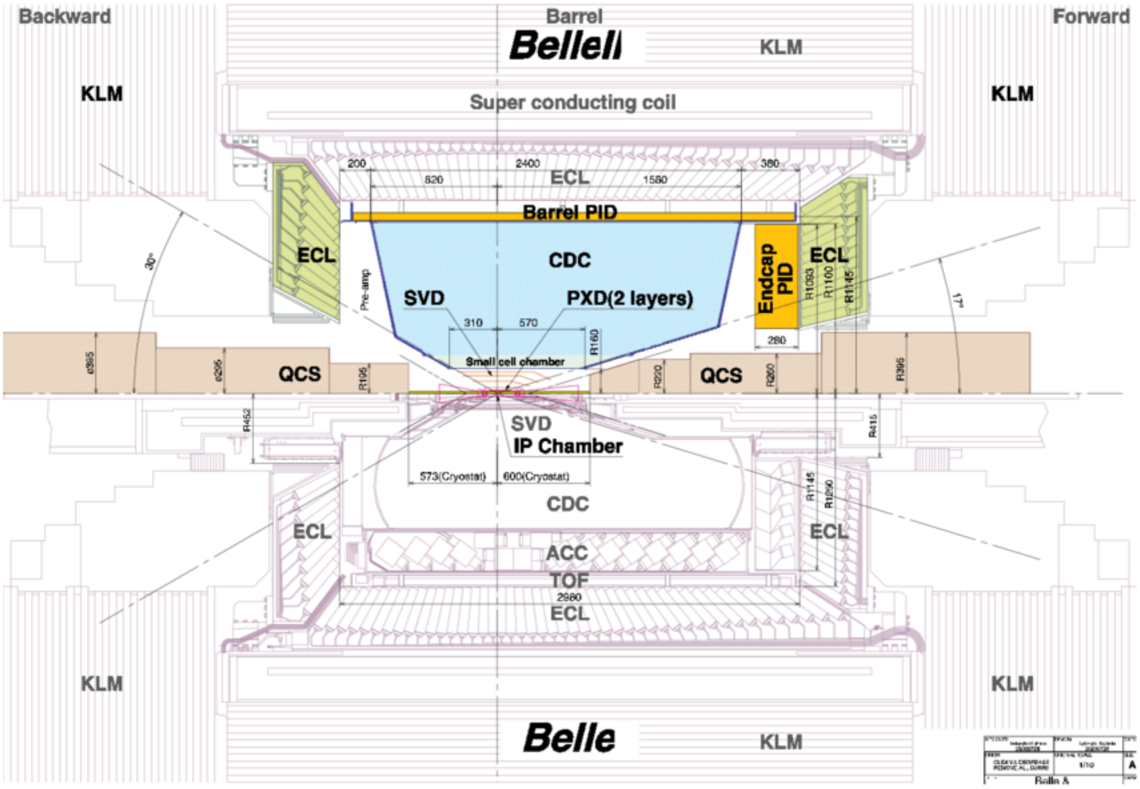

Figure 3.2.: A diagram of the Belle II detector components and geometry. [36]

3.3.1. Interaction Region (IR)

The Belle II detector was designed to precisely measure differences in the decay times of pairs of $B\overline{B}$ mesons, and so has an inbuilt asymmetry in the energy of the collision beams. This is because the $\Upsilon(4S)$ mass is just at the threshold of open beauty, producing near at rest, B mesons in the CMS frame. The beam asymmetry leads to the creation of B mesons with a large lab frame momentum, allowing for more precise determination of decay time, that is, the B mesons will travel further in the time it takes them to decay in the lab frame, leading to greater spatial separation of their respective decay vertices. The interaction region of Belle II uses quadrupole magnets to focus the positron and electron beams to a fixed interaction point with a non-zero crossing angle of 83 milliradians. This is so that the beams will separate quickly, keeping the interaction point localised.

The 4-vector of the CMS, in the lab frame, is p_{CMS} =(11.0 GeV,0.457 GeV,0 GeV, 3.03 GeV). The large z momentum component is due to the asymmetry in beam energy and the x momentum component is due to the nonzero crossing angle of the beams.

In Figure 3.2 it can be seen that the components of Belle II are built with an asymmetry to compensate for the asymmetry in beam energy. The positive z direction is to the right of Figure 3.2.

3.3.2. Pixel Detector (PXD) and Silicon Vertex Detector (SVD)

The PXD and SVD are designed to provide high precision vertexing information for B decays, allowing, for example, accurate determination of mixing induced CP asymmetry. Combined, the SVD and PXD have an impact parameter resolution of $20\mu m$.

At distances very close to the IR, the high luminosity of SuperKEKB means that beam background effects prevent a silicon strip system (used at Belle) from being effective at reconstructing a B vertex. To achieve the required resolution, Belle II uses a greater number of smaller silicon pixels. This increases the number of channels that must be processed, but provides a gain in resolution. Past a radius of 38 mm, silicon strips are sufficient, and are used instead of pixels so as to reduce cost and number of readout channels. This is the SVD.

When a sufficiently high energy charged particle is incident on a silicon pixel or strip, a shift in potential across the silicon causes a current that can be measured. This is a nondestructive measurement that allows for high resolution particle tracking. The potential shift is the result of an electron hole pair formation, which needs to be reset after measurement, so the pixels run on a $20\mu s$ cycle that includes a 100 ns period of dead time during reset.

3.3.3. Central Drift Chamber

Further out from the IP is the Central Drift Chamber (CDC). In this region, the precision need not be as high as in the SVD, as at this radius, the B mesons will have well and truly decayed. The CDC consists of 14 336 sensing wires submerged in an equal parts mix of helium and ethane gas. Charged particles will ionise the gas, causing the freed electrons to drift towards the nearest active sensing wire. This will change the potential of the wire. By measuring the drift time, a precise position of the charged particle interaction can be determined. A mixture of axial and small angle sensing wires allows for a high resolution in the beam direction. Once a charged track is constructed, the curvature of the track in the magnetic field can be used for identification and determining momentum. The CDC has an $r\phi$ resolution of $100\mu m$ and a z resolution of 2 mm. The CDC spans a polar angle of 17° to 150°, as can be seen in Figure 3.2.

3.3.4. TOP and ARICH

The barrel region has a set of Time Of Propagation (TOP) counters, labelled in Figure 3.2 as Barrel PID. These consists of quartz bars placed around the barrel, running along the z axis. Traveling charged particles incident on those quartz bars generate Cerenkov radiation. The quartz bars cause total internal reflection, focusing all of the Cerenkov light onto the photon detectors at the bar's end. Reconstructing the time and spatial coordinates of Cerenkov light cones formed in the quartz bars allows for the precise determination of time and spatial coordinates of the incident charged particles. By measuring the characteristics of the Cerenkov light, the TOP is also able to effectively separate charged kaons from pions.

In the endcaps, the same information is determined with the Aerogel Ring-Imaging Cherenkov detector (ARICH), labelled in Figure 3.2 as Endcap PID. This consists of a large aerogel disc, to allow the formation of Cerenkov radiation; and an array of photon detectors. The TOP and ARICH serve the same purpose, but the geometry of Belle II means that a large disk of aerogel is more appropriate for the endcaps than the quartz bars that are used in the barrel would be.

3.3.5. Electromagnetic Calorimeter (ECL)

The Electromagnetic Calorimeter (ECL) is designed to measure electromagnetic energy. The ECL destructively identifies photons and electrons and measures their energy. The ECL consists of 8736 CsI scintillating crystals, spanning a polar angle of $12.4^{\circ} < \theta < 155.1^{\circ}$, with a 1° gap between the barrel and endcap. Glued to the back of each crystal is a photodiode that will absorb and measure the energy of photons produced from scintillation within the crystal.

Both electrons and photons incident on the CsI crystals will produce an electromagnetic shower, a cascade of electron positron pairs, which in turn produce Bremsstrahlung radiation, leading to more, lower energy, electron-positron pairs, repeating this process until the energy of the photons produced is below the threshold required for electron positron pair production. If the incident particle is an electron or photon, then by collecting all the components of the EM shower, the energy of the original incident particle can be determined. The CsI crystals have a radiation length of 1.86 cm, meaning nearly all photons will be absorbed by the ECL.

The showering does not allow the distinction between an electron signal or photon, both appear as a cluster in the ECL. The discriminating factor is the presence of a charged track in the CDC for the electron. This can lead to misidentification between electrons and photons when, for example, a photon is along the same trajectory as an unrelated charged track.

3.3.6. K_L and Muon Detector (KLM)

The K_L and Muon detector (KLM) consists of alternating layers of iron plates and glass electrode resistive plate chambers. The steel plates provide 3.9 hadronic interaction lengths for K_L to shower hadronically. This is in addition to the 0.9 hadronic interaction lengths in the ECL. Shower components can be detected in KLM, ECL or both, allowing for K_L detection using a combination of the two detector elements.

Hits in the KLM within 5° of each other (measuring the angle from the IP) are grouped into a cluster. The separation of K_L from muons is done, as with electron/photon separation, via a charged track veto on K_L candidates. Charged tracks are extrapolated to their entry point into the KLM. If the line from the entry point to the IP makes an angle with the centre of the KLM cluster that is less than 15°, then the cluster is considered not to be a K_L. The K_L candidate must then have hits in at least 2 layers of the KLM or one in the KLM and one in the ECL. A KLM cluster matched to a charged track that is consistent with a muon is considered a muon candidate. The KLM spans a polar angle of $20^\circ < \theta < 155^\circ$.

3.3.7. Triggering

If Belle II were to record every event, its data output would be enormous, and mostly uninteresting. Limits on data storage and readout speed make this unfeasible, so, to reduce the volume of data and select for events of interest, there are a set of “triggers”. These are hardware based selections that must be passed before an event is stored. The first level trigger consists of five subtriggers (CDC, ECL, KLM, BarrelPID, Endcap PID) that record clusters, track multiplicity, timing, etc. This information is then passed to the Global Decision Logic (GDL), which will either discard or pass the event to the next level. The higher levels of computing make further selections based on more complete event reconstruction. At each stage of triggering, the data volume being processed is reduced, allowing for more complex cuts to be applied at the next stage without a pileup queue of events.

3.4. Beam Background

The term beam background is a used to refer to the background signals that are produced by elastic collisions of the beams and beam collisions with material in the beam pipe and detector. Beam background represents the effects of the incident beams misbehaving. Beam background is especially important to consider at Belle II due to the high luminosity, given most forms of beam background are produced proportionally to luminosity. The different kinds of beam background are presented below.

3.4.1. Touschek Scattering

The filling of the beams is done in bunches of leptons. The Touschek effect refers to Coulomb interactions between leptons in the same bunch in a storage ring [37]. This leads to the increase in energy of one particle and the decrease in another. The lepton energy is then not the design energy of the accelerator, so these particles are subsequently lost at the beam pipe wall. If this takes place near the detector it will result in a shower of particles that may be picked up by the detector elements.

The Touschek effect is expected to be especially pronounced in the Belle II experiment as it is proportional to the number of bunches, the square of the beam current, the cube of the energy and inversely proportional to the beam size. The high luminosity and small beam width of the beams at SuperKEKB will lead to a significant incidence of Touschek events.

3.4.2. Beam-Gas Scattering

The vacuum inside the beam-pipe cannot be perfect, as there will always be some residual gas inside the beam-pipe. This means that the incoming beams can interact with gas molecules in either Coulomb scattering, changing the direction of the particle; or Bremsstrahlung scattering, reducing the energy. The Bremsstrahlung events will then behave the same as Touschek scattering events, showering and colliding with the beam wall. The rate of Bremsstrahlung gas scattering is expected to be negligible compared to the Touschek rate. The Coulomb scattering rate, however, is expected to be high due to the small beam-pipe radius inside the Belle II detector.

To counter both Touschek and beam-gas scattering, heavy metal shields are placed at the edges of the detector, in combination with collimators, used to stop particles that deviate from the expected beam trajectory.

3.4.3. Synchrotron Radiation

Magnetic fields are used to maintain the orbit of the electron and positron beams around the SuperKEKB rings. The acceleration of the beams around the SuperKEKB ring with these magnetic fields results in the emission of synchrotron radiation. The power of the radiation emission is proportional to the beam energy squared, so the main source of synchrotron radiation is from the higher energy, electron beam. The synchrotron radiation photons range from roughly 1 to 10 keV in energy. These photons may land in the detector, producing extra photon signals.

3.4.4. Radiative Bhabha Processes

Radiative Bhabha scattering refers to the e^+e^- interaction described by the Feynman diagram in Figure 3.3. These are events where a photon is emitted by one of the beams before or after the interaction between the positron and electron beams. This is similar to an ISR process but preserves the electron and positron in the final state. The photons produced in radiative Bhabha processes interact with iron in the detector and through the giant nuclear resonance mechanism [38] can produce neutron radiation, which is the primary background for the KLM.

Figure 3.3.: Feynman diagram of radiative Bhabha scattering

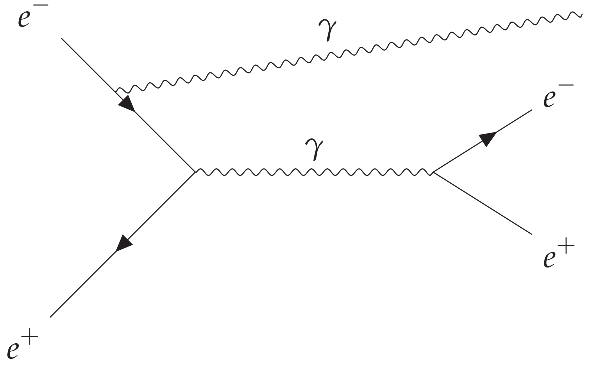

The magnetic fields in the beam pipe are designed to maintain a stable beam path for the specific design energies of the collider. After the emission of a photon through a radiative Bhabha process, the electron and positron are then lower in energy than the energies designed for the beam pipe, so the beam particles will be curved by the magnetic field more or less than is required to preserve a stable beam and will collide with the beam-pipe, leading to showering.

3.4.5. Two Photon Processes

A two photon process, $e^+e^- \to e^+e^-e^+e^-$, is a higher order electromagnetic process which can generate very low momentum electrons and positrons. Given the low momentum, these electrons and positrons will spiral around the magnetic field, with a small synchrotron radius, leaving hits in the inner detectors.

3.4.6. Beam Background Summary

Of these background processes, the most important are radiative Bhabha scattering, Touschek scattering, and beam gas interactions [38]. The combined dominant effect of these background processes is to generate large numbers of extra charged tracks and deposits in the ECL which are generally collinear with the beam line.

3.5. K_L Measurement

The Belle II detector currently has an imperfect K_L reconstruction method. The Belle II Technical Design Report states that "due to large fluctuations in the shower development of a K_L nuclear collision the number of hits within a cluster is a poor measure of K_L energy" [1]. Due to this, the KLM clusters are currently used only to determine the direction and position of the K_L. It could however, be possible to use the timing information of these clusters as a measure of the velocity, and therefore momentum and energy of the K_L. The shape of cluster formation is another area that is currently being studied within the Belle II collaboration as a possible avenue for determining more accurate information about the K_L.

To be able to carry out a calibration, first, a sample of K_L for which the energy is known must be acquired. A process that provides a clean channel of K_L with known energies is the initial state radiation (ISR) production of a $K_L K_S$ final state, dominated by the ϕ meson resonance, as described in the previous chapter.

3.6. Initial State Radiation (ISR) at Belle II

The cross section for $\Upsilon(4S)$ production at the resonance energy is 1.2 nb [1]. The total cross section for electron-positron annihilation is 8 nb. These and the remaining remaining background processes are summarized in Table 3.1. One of these background processes is the emission of initial state radiation (discussed in the previous

Table 3.1.: Cross Sections at $\Upsilon(4S)$ Resonance [1]

	cross section (nb)
$\Upsilon(4S) \rightarrow B\overline{B}$	1.2
$q\overline{q}$ continuum	2.8
$\tau^-\tau^+$	0.8
$\mu^-\mu+$	0.8
Bhabha ($\theta_{lab} \geq 17^\circ$)	$\sim$44
$\gamma\gamma$ ($\theta_{lab} \geq 17^\circ$)	2.4
2γ processes[1] ($\theta \geq 17^\circ$,$p_t \geq 0.1$ GeV/c)	$\sim$80
Total	$\sim$130

chapter). As indicated previously, ISR presents an opportunity for K_L calibration via the ISR production of the K_SK_L final state, dominated by the ϕ meson intermediate state, with a cross section of $\sigma = (0.0241 \pm 0.0003)\ fb$ [34].

A ϕ meson will decay to a $K^0\overline{K^0}$ final state 34% of the time [26]. This final state will undergo neutral mixing and produce a K_SK_L final state. If the ISR photon and the K_S can be correctly reconstructed, then by subtracting their energy-momentum 4 vectors from that of the known initial state 4-vector, the 4 vector of the K_L meson can be predicted. There are other processes that produce K_L that may be useful, D^* decays for example, however the $e^+e^- \to K_SK_L\gamma$ channel is particularly promising as, in this ISR channel we expect a 5.24 GeV ISR photon recoiling against a ϕ meson, is well over the energy that is expected to be seen in photons produced in the dominant, $B\overline{B}$ events or charmonium continuum events seen at Belle II. That is this process produces a very high energy photon and is a low multiplicity event. By selecting for a high energy photon, almost all background can be eliminated.

Chapter 4.

Simulation

This chapter includes a description of the simulation used to study the ISR $K_S K_L$ production channel and the Monte-Carlo generated kinematics of the particles in this channel.

4.1. Monte-Carlo Methods

Particle interactions are inherently probabilistic. Each particle passing through a given detector element may or may not interact, meaning some percentage of particles will pass through the detector and not leave enough of a signal to reconstruct.

The topology of each decay is likewise, a process governed by probabilities, with those probabilities fixed by the underlying physics. In the rest frame of a parent particle, the daughter particles of a two body decay must be back to back to conserve momentum. Over many events, the 4-vectors of the decay products will map out the allowed phase space of the decay. For parent particles with with no preferred direction, the unit vector in the direction of momentum will map out the unit sphere. This is a uniform distribution in ϕ and in $\cos(\theta)$. The ϕ meson is a spin 1, vector meson, so will not decay uniformly, but will have a preferred direction of production of its daughter mesons. This can be seen in Figure 4.3.

For each event, there is some probability that the particles that one wishes to observe will have a trajectory that lies outside the detector region. There is no chance of reconstructing these particles as there will be no signal within the detector to reconstruct. To remove background events, restrictions are often made on energy, transverse momentum and various other discriminating factors that select for events of interest. These cuts are designed to remove background events and preferably select for the desired signal.

To make it into the useful signal sample, each event must have enough required particles within the detector that interact with the detector elements to produce tracks and clusters that are sufficient for each particle's reconstruction, and then, that event must pass trigger and analysis cuts. To be able to interpret the data produced by a particle physics experiment, first one must know what fraction of the total events the reconstructed sample represents. This fraction is called the efficiency (ϵ).

$$\epsilon = \frac{\text{the number of signal events passing all requirements}}{\text{the total number of signal events}} \tag{4.1}$$

To interpret the data produced by a particle physics experiment, the efficiency must be known so that the final data set can be reverse engineered to determine the underlying physics. To determine this efficiency, we perform a Monte-Carlo (MC) generation of simulated events, simulate their passage through the detector, then apply the same cuts that would be applied to real data, but with knowledge of the underlying truth. From an MC simulation, the effects of detector interactions and analysis cuts can be determined.

For this project the goal was to determine if the ISR $K_L K_S$ channel will provide enough well-reconstructed events to make up a sample that can be used for K_L calibration. For an event to be well-reconstructed in K_L calibration there must be: a correctly reconstructed K_S, a correctly reconstructed ISR photon and a K_L within the geometric acceptance of the KLM in θ_{lab}, ($20^\circ < \theta_{lab} < 155^\circ$). From this point forward, events that pass all of these requirements are referred to as well-reconstructed.

4.2. Software

4.2.1. basf2

The Belle II analysis software framework, basf2 [4], is a complex system of modular functions that have been developed by the Belle II collaboration to simulate events, detector interactions and particle reconstruction. The software utilizes C++, among other languages at various stages of simulation and analysis, called through an analysis framework constructed in python. As the analysis code is still in development a significant focus of this project was probing and testing the validity of the analysis code. For example the first iteration of this code tested, did not include the KLM endcaps in the simulation. This was amended in the subsequent release. The basf2 release used to produce the final data sets in this thesis was release-01-02-11.

4.2.2. ROOT

The standard code framework for particle physics is ROOT [6]. ROOT is an object oriented, C++ based code library that contains tools useful for advanced statistical analysis (e.g. fitting and histogram plotting) and elements useful for manipulation of high level objects related to particle properties, such as Lorentz vectors. As the Belle II software uses a python based interface, ROOT was imported as a module. ROOT was used to produce all plots in this thesis [6].

4.2.3. Phokhara

The simulation here is broken into multiple stages. The first stage of the simulation randomly generates a set of particle vectors according to a model of the underlying physics. For Belle II, initial MC generation is generally done with EvtGen [5]. In all cases it was found that EvtGen produced 3 initial state photons, 2 of which had an energy of zero. This is not an example of the simulation of second order ISR, as EvtGen does not simulate second order ISR, but instead appears to be an artifact of the way that EvtGen simulates first order ISR.

For our purposes it was found that Phokhara was the superior generator. This is because Phokhara is the benchmark in ISR simulation and capable of simulating higher order ISR [2]. For the simulation here, Phokhara 9.1 was used. At the time of writing, two new versions of Phokhara have been released, but with no relevant update to the simulation of the $K_L K_S$ final state.

Phokhara includes both one and two ISR photon events, but does not produce events with more than two real ISR photons, as the cross section for these events is very small. Phokhara does take into account up to 2-loop diagrams and corrections from events where one real and one virtual ISR photon is produced [2].

Phokhara does not generate a $K_S K_L$ pair but instead pipes a $K^0\overline{K^0}$ final state (which is dominated by the ϕ resonance) and the ISR photon(s) to GEANT4. It was found that the next stage of the simulation would then carry out the kaon mixing without preserving the entanglement of the two kaons, which would result in unphysical final states of either two K_S or two K_L. Phokhara was modified to output a $K_S K_L$ final state to amend this.

4.2.4. GEANT4

The following stage evolves the MC particles through the detector. This stage uses GEANT4 [3], a toolkit for simulating the passage of particles through matter. GEANT4 generates the simulated hits in the relevant detector elements and decays particles that decay away from the interaction point (this stage performs the decay of the K_S), whilst also generating particles from secondary physics processes such as detector interactions and electromagnetic showers. The output of this stage is then the matching of tracks, clusters and MC particles. This is also the stage where beam background is simulated.

4.2.5. Reconstruction

The final stage uses the output of GEANT4 to construct lists of candidate particles with the associated probabilities of correct identification. In this stage, higher level reconstruction of decay chains is performed. In the case of this simulation, the photon candidate list is generated from ECL clusters and then the K_S candidate list is generated from pairs of oppositely charged pion candidates. This uses the clusters and tracks in the same way one would with real data, but also includes the addition of matching of candidates to MC generated particles.

For this analysis, two data sets of 500 k ISR $K_S K_L$ events were produced, one data set with beam background and one without. Both samples included the simulation of second order ISR events. 64% of events contained two ISR photons, and as such, the sample of 500 000 events without beam background contained 819 005 ISR photons in total due to the 319 005 events with two ISR photons.

There were multiple possible settings for beam background that could have been chosen, as the beam background has not yet been studied at the new luminosity. The nominal estimate for beam background was chosen for this analysis[1]. The following section will only consider the sample without beam background. The sample generated with beam background will be discussed later.

4.3. Generated Kinematics

To be able to use an event for calibration of the K_L, the entirety of the rest of the event is required. This means that the ISR photon and the K_S must be correctly reconstructed. The K_L must also be within the geometric acceptance of the KLM. We would still be able to estimate its 4-vector without this, but will have no detector interactions for comparison, making the event useless for calibration. The photon must also be within the geometry of the CDC ($17^\circ < \theta_{lab} < 150^\circ$). The ECL is larger than this and clusters will be left in the ECL by photons outside of this geometry, but outside of the CDC, there is no way to veto electrons by the presence of a charged track. The K_S is reconstructed from the $K_S \to \pi^+\pi^-$ channel, which has a branching fraction of 69.2%. The less likely $K_S \to \pi^0\pi^0$ channel, which accounts for 30.69% of K_S decays, is not used.

Before reconstruction efficiency is considered, the effects of detector geometry must be understood.

4.3.1. ISR Photon Kinematics

Figure 4.1 shows the kinematics of the MC generated ISR photons. A primary ISR event has the same kinematic constraints as a 2 body decay, so momentum conservation fixes the energy of both the ϕ meson and the ISR photon. In a primary ISR event, to produce a ϕ meson, which has a mass of 1.019 GeV, from a system with a CMS energy equal to the mass of an $\Upsilon(4S)$, 10.58 GeV, one of the two incoming particles must emit a single ISR photon with an energy of 5.24 GeV in the CMS frame.

The ISR photon energy distribution in Figure 4.1 (b) exhibits two large peaks at roughly 4 and 7 GeV and a peak close to zero. The two larger peaks are a result of

---

[1] The beam background setting labelled BGx1

the energy asymmetry of the positron and electron beams. These photons have the same energy in the CMS frame, 5.24 GeV (see Figure 4.1 (c)), but when boosted into the lab frame, the photon energy is shifted based on whether the photon is forward or backward relative to the boost. The low energy distribution and peak is a result of soft, second order ISR photons.

A uniform distribution on the unit sphere has a flat distribution in $\cos(\theta_{lab})$. In Figure 4.1 (a) it can be seen that the $\cos(\theta_{lab})$ distribution of the ISR photon has a striking skew towards the positive and negative z direction, i.e ISR photons are produced collinear to the beam line. This is due to the fact that the CMS energy comes from the incoming beams' very large z momentum. For the production of an ISR photon to reduce that CMS energy enough to produce a ϕ meson, the beams z

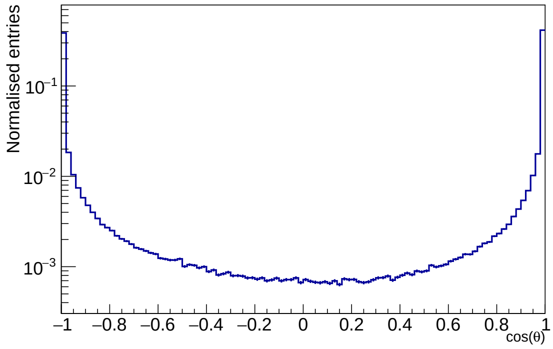

(a) Normalised MC generated $\cos(\theta_{lab})$ distribution for ISR photons

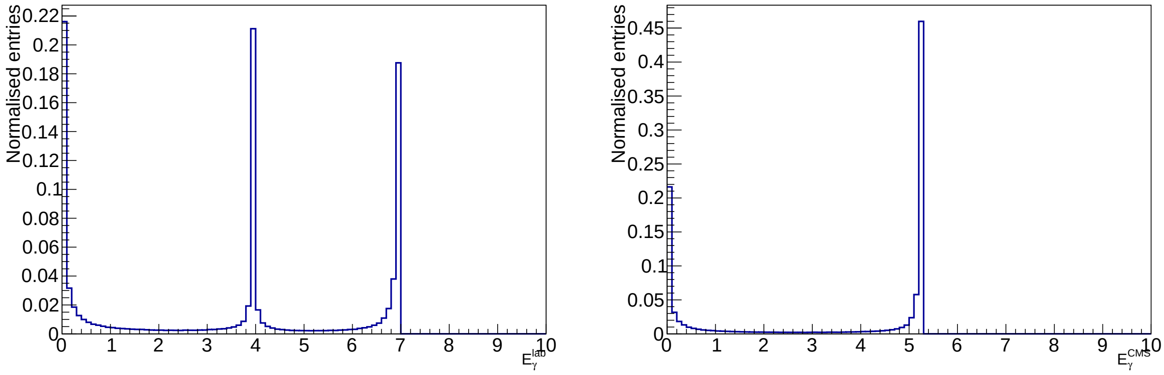

(b) Normalised MC generated lab frame energy for ISR photons.

(c) Normalised MC generated CMS energy distribution for ISR photons.

Figure 4.1.: ISR photon MC generated kinematics in the sample of 500 k ISR $K_S K_L$ events with no beam background.

momentum must be reduced. Momentum must be conserved, so the resultant ISR photon must then have a very high z momentum.

4.3.2. K_L and K_S Kinematics

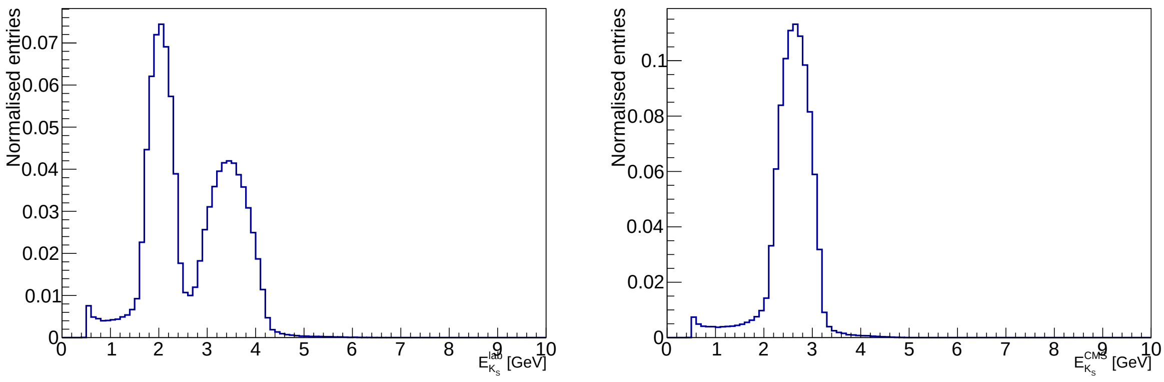

(a) Normalised MC generated energy for K_S in the lab frame.

(b) Normalised MC generated energy for K_S in the CMS frame.

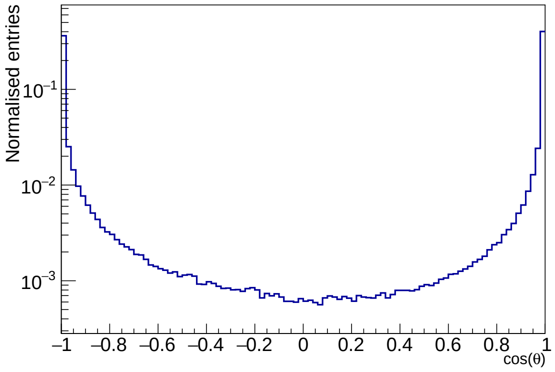

(c) Normalised MC generated $\cos(\theta_{lab})$ distribution for K_S

Figure 4.2.: K_S generated kinematics in the sample of 500 k ISR K_SK_L events with no beam background.

Given the K_L and K_S have an almost identical mass, there is a symmetry with respect to the permutation of the two particles. Due to this, the two particles behave the same in terms of kinematics. The generated distributions for both K_L and K_S are identical, and as such, only the K_S distributions are shown in Figure 4.2.

In Figure 4.2 (c), the K_S shows a similar $\cos(\theta_{lab})$ distribution to the ISR photon. To balance the z momentum of the ISR photon, the ϕ meson must also have the same skew in the z direction. The ϕ mass is close to the mass sum of the kaon pair. This means that in the ϕ meson rest frame, the kaons will have a low momentum, so the kaon momentum distribution is dominated by the ϕ momentum boost and not the ϕ rest mass energy. This means that the kaons also have a $\cos(\theta_{lab})$ distribution that is skewed towards the beam line, similar to the photon $\cos(\theta_{lab})$ distribution. As with the photon, the kaon energy distribution shows the split of a single peak in the CMS energy into two peaks in the lab frame energy, based on whether the CMS frame 4-vector points forward or backward. This is shown in Figure 4.2 (a) and (b).

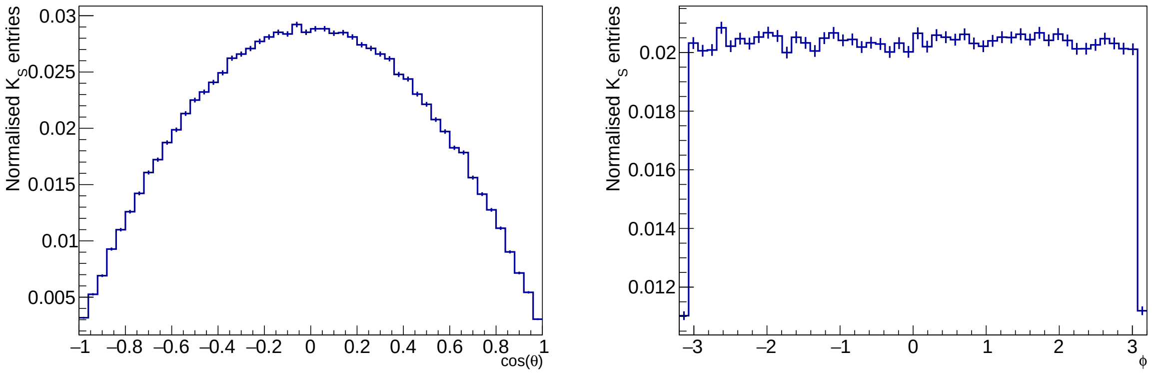

(a) The normalised distribution of the K_S $\cos(\theta)$ in the ϕ meson rest frame

(b) The normalised distribution of the K_S azimuthal angle in the *phi* meson rest frame

Figure 4.3.: K_S angular distributions in the rest frame of the ϕ meson.

The kaon CMS energy distribution is broader than the sharp spike seen in the photon energy distribution. This is because, in the ϕ meson rest frame, the K_L and K_S 4-vector direction will map out the phase space of the ϕ (a spin-1 parent) decaying with its axis collinear to the beam line, with the kaons receiving a different momentum boost depending on the angle between their ϕ meson rest frame 4-vector and the boost vector. The kaon's energy would be a single peak in the ϕ meson rest frame. The angular distributions of the K_S in the ϕ meson rest frame are shown in Figure 4.3. The component of the kaon ϕ frame momentum vector parallel to the boost from the ϕ meson momentum will then depend on the ϕ meson rest frame decay axis. This results in the broadening of the distribution of the K_S energy seen in Figure 4.2 (b).

4.3.3. Two Photon Events

The secondary soft ISR photons, seen at low energies in Figure 4.1 (b), are a result of events where higher order ISR processes take place. In these events two photons are emitted reducing the beam energy enough to produce the ϕ meson.

Figures 4.4 (a) and (b) show the MC generated energy of the higher energy, primary, ISR photon plotted against the energy of the lower energy, secondary ISR photon, both in the CMS frame. Both (a) and (b) are the same plot displayed in different forms. In (a) it can be seen that the vast majority of events exhibit one high energy photon, close to 5.24 GeV, and a second photon with very low energy. (b) is included to display the distribution of the less common events, where the energy is more evenly shared between the two photons. This distribution maps out a diagonal line where the energy sum of the two photons is 5.24 GeV and a curved vertical line just below 5.24 GeV. The diagonal line corresponds to events where the photons are emitted from the same beam and effectively function as two photons that sum to give the same kinematics as the single ISR photon case.

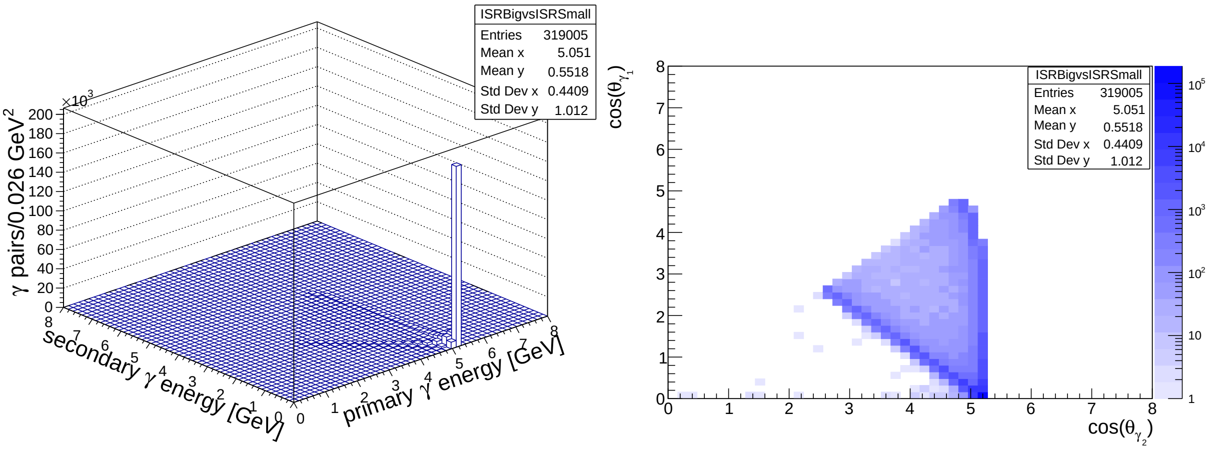

(a) Lego plot

(b) Colour plot

Figure 4.4.: The energy of the higher energy ISR photon vs the energy of the lower energy ISR photon, both in the CMS frame. (a) is a lego plot to illustrate that most second order events contain one high energy photon close to 5.24 GeV and one very low energy photon. (b) is a colour plot that better illustrates the relationship between the energy of the two photons in the less common cases where energy is shared more evenly.

First order ISR events have the same kinematic constraints as a 2-body decay, the restrictions on the recoil of momentum between the photon and the lower energy state

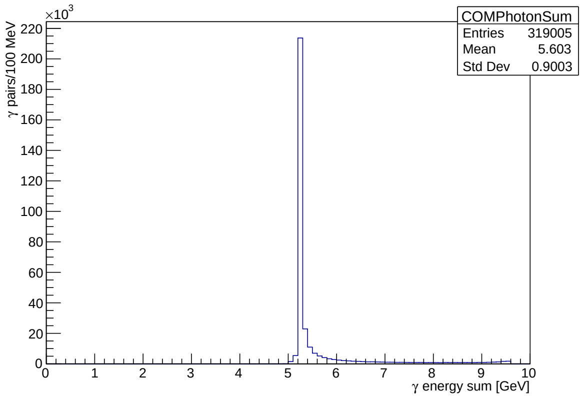

Figure 4.5.: The sum of the MC generated energy of both ISR photons in the CMS frame for events where 2 ISR photons are produced in the simulation of 500 k ISR $K_S K_L$ events with no beam background.

result in both an ISR photon and a recoiling state with momentum collinear to the beam. Two photon events, however, behave kinematically like a three body decay, so it is possible to produce a ϕ that is close to rest in the CMS frame. The vertical curved part of the distribution in Figure 4.4 (b) corresponds to events where one photon is radiated from each incoming beam, back to back, meaning the ϕ meson mustn't necessarily be collinear with the beam line.This produces a ϕ meson with an energy closer to its rest mass. The photons, therefore, can sum up to an energy of 9.56 GeV, equal to the difference between the ϕ and $\Upsilon(4S)$ mass. The sum of the energy of the two photons is displayed in Figure 4.5.

4.4. Reconstruction

To produce the photon candidate list, a track veto is performed on clusters in the ECL. If there are no CDC tracks that can be extrapolated to the ECL cluster (as this would imply the ECL cluster is the result of an electron) it is considered a photon candidate. This also means that photon candidates are restricted to the geometry of the CDC so that the track veto can be performed. The list of K_S candidates is constructed by performing a vertex fit on pairs of oppositely charged pions, rejecting candidates with an invariant mass outside of a 100 MeV window around the K_S mass, $(0.450 < M < 0.550)$ GeV.

4.4.1. Purity

ISR channels are different to the majority of Belle II channels studied, which would in general focus on $B\overline{B}$ decays. In an analysis of a $B\overline{B}$ channel a considerable effort would be spent determining the purity, the purity being defined as the percentage of events in an analysis that pass all cuts and are also not the result of background sources or misidentification i.e what fraction of the events in the final sample are correctly identified as being from the channel of interest. With this particular ISR channel, a cut requiring a high energy photon, is able to remove nearly all of the non ISR events produced at Belle II, isolating the ISR events of interest. This is explained by the fact that 5.24 GeV (the CMS energy of a primary ISR photon in the channel being studied) is only 39 MeV below the B mass, and since a B meson can not decay into a single photon, $B\overline{B}$ events can effectively be completely removed with a photon cut. To test this, a sample of 90 million $B\overline{B}$ MC events was examined[2]. It was found that a photon energy cut as low as 3 GeV removed all reconstructed photons from the sample. The highest energy photon found in MC generated particles of MC7 had an energy of 3.5 GeV. This was part of the motivation behind the choice of the ISR channel, as it provides a very clean sample.

4.4.2. Number of Well-Reconstructed Events

To test the number of expected well-reconstructed events, MC generated information was used to cut out effects from incorrectly reconstructed events and extra false events from background, allowing the analysis of a best case scenario. The MC generated output variables used here required that the particle was correctly identified, that its parent particle was correct (technically, the ISR particles return a value of zero, indicating no parent) and that it was not the result of a secondary physics process.

Table 4.1 shows the cut flow of 500 k simulated ISR $K_S K_L$ events without beam background. These cuts require that:

- A photon be correctly reconstructed and matched to an MC generated ISR photon and within the CDC geometry ($17^\circ < \theta_{lab} < 150^\circ$).

---

[2] The Belle II collaboration produces large samples of MC $B\overline{B}$ events and stores them locally at KEK. This was a sample of files from the official production known as MC7 at KEKCC.

Table 4.1.: The events with correctly reconstructed particles for 500 k simulated ISR $K_S K_L$ events without beam background.

Events with:	# Events	efficiency %	Events with:	# Events	efficiency %
-	500 000	-	ISR γ and K_S	26 170	8.9
ISR γ	88 910	18	ISR γ and K_L	54 668	11
K_S	37 963	7.6	K_S and K_L	28 888	5.8
K_L	143 917	29	γ and K_S and K_L	24 517	4.9
			2γ and K_S and K_L	1 794	0.36

- A K_S candidate in the K_S list be correctly reconstructed and matched to the MC generated K_S.
- The MC generated K_L trajectory fall within the KLM geometry ($20^\circ < \theta_{lab} < 155^\circ$).

The cut applied to the K_S candidate is the most restrictive, which is understandable given that to reconstruct the K_S, both its daughter pions need to fall within the detector and be reconstructed. In practice, if one particle is within the detector geometry then conservation of momentum means that the others are also likely to have a large enough transverse momentum to also be within the geometry of the detector.

4.4.3. Reconstruction of Two Photon Events

In the two photon events mentioned previously, there is no correlation between the angle of the two ISR photons. Figure 4.6 shows the generated $\cos(\theta)$ distribution of the primary ISR photon compared with the generated $\cos(\theta)$ distribution of the secondary ISR photon. It can be seen that most events have both photons lying along the beam line either parallel or anti-parallel (at the corners of the lego plot in Figure 4.6 (b)). The anti-parallel case is slightly more likely.

The photon angular distribution means that most ISR photons fall outside the geometric acceptance of the ECL and CDC. It is therefore unlikely that one photon is reconstructed. Since both photons are likely to be emitted along the beam line, capturing both is extremely unlikely. As a result, only 1 794 events out of the 319 005 two photon events, contain two correctly reconstructed ISR photons and all other required particles. This corresponds to a 0.56% efficiency.

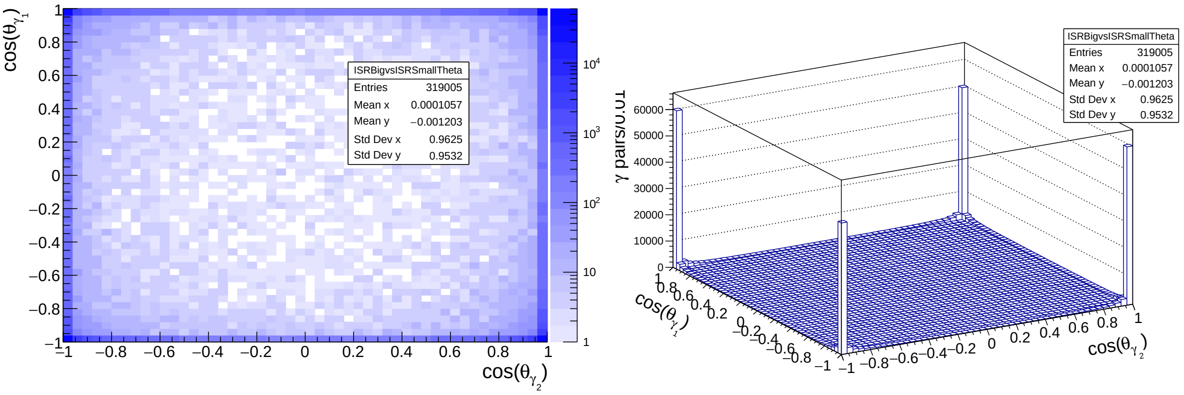

(a) Colour plot **(b)** Lego plot

Figure 4.6.: The cosine of the polar angle of the primary ISR photon vs that of the secondary ISR photon in MC generated particles for the simulation of 500 k ISR $K_S K_L$ events with no beam background.

4.5. Effect of Beam Background on Reconstruction

The simulation discussed up until now was carried out without beam background. Beam background is simulated by GEANT4 at the second stage of the simulation, adding extra hits in the detector. The beam background therefore does not have associated MC generated particles and exists only as deposits in the detector elements. This was most likely done to save on file size as there are a very large number of beam background photons.

The addition of beam background in a sample of 500 k ISR events, led to an additional 32 million reconstructed photon candidates. The number of correctly reconstructed ISR photon candidates dropped from 88 910 to 30 049. Figure 4.7 compares the energy distribution of photon candidates from beam background to those from ISR photons. The most obvious effect of the beam background is that the low energy photons from signal ISR events become hard to distinguish from beam background. An energy cut of 3 GeV is sufficient to remove almost all the photons that arise from beam background. This same cut applied to a set of MC $B\overline{B}$ events removes all events.

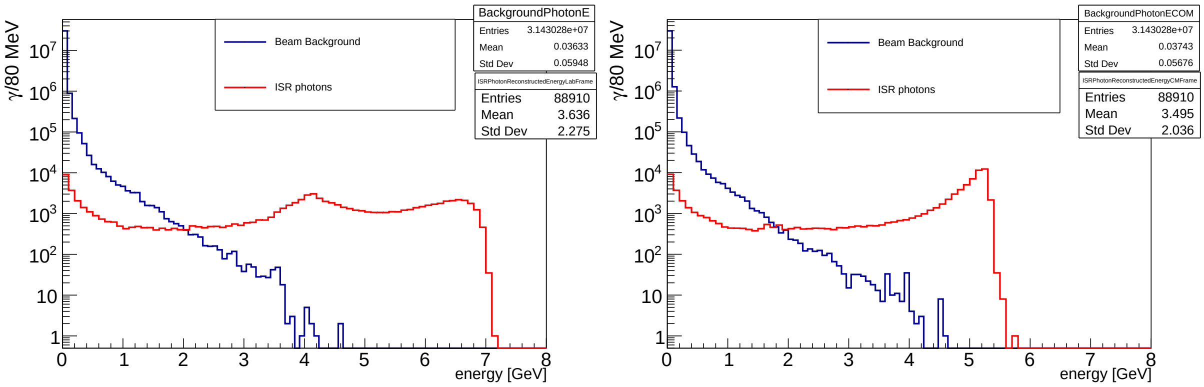

(a) Lab frame energy

(b) CMS frame energy

Figure 4.7.: A comparison between the reconstructed energy of beam background photon candidates and ISR photon candidates from the simulation of 500 k ISR $K_S K_L$ events with beam background. (a) shows the lab frame photon energy and (b) shows the CMS frame photon energy.

4.5.1. Cluster Timing

Cluster timing refers to the time measurement associated with the highest energy crystal in a cluster, this is then corrected for time-of-flight through the detector. After corrections, a photon from the IP should have a cluster timing equal or close to 0 ns. The cluster timing was considered as a method of removing photon candidates caused by beam background, as one would expect the arrival of background candidate photons to be uncorrelated with the timing of the collision. Figure 4.8 shows the cluster timing distributions, both for photon candidates caused by ISR and those caused by beam background. The beam background distribution is much broader than that of the ISR, spanning a range of ± 800 ns, whereas the ISR candidates span a range of ± 200 ns. Even a liberal cut on cluster timing is able to remove a significant percentage of beam background without removing true ISR photons.

The reason for implementing the cluster timing cut would be to extract the low energy ISR photons from the beam background candidates as, above a 3 GeV CMS photon energy cut, effectively all photon candidates in the sample are from ISR (see Figure 4.7). Table 4.2 shows the effect of a cluster timing cut on the number of photon candidates with a CMS energy below 3 GeV, from both beam background and from ISR photons.

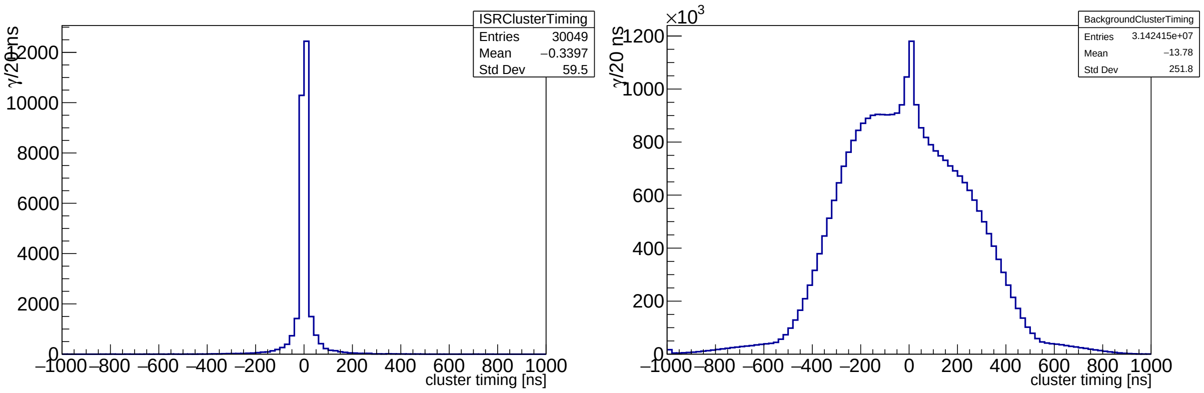

(a) Cluster timing for photon candidates from ISR photons.

(b) Cluster timing for photon candidates from beam background.

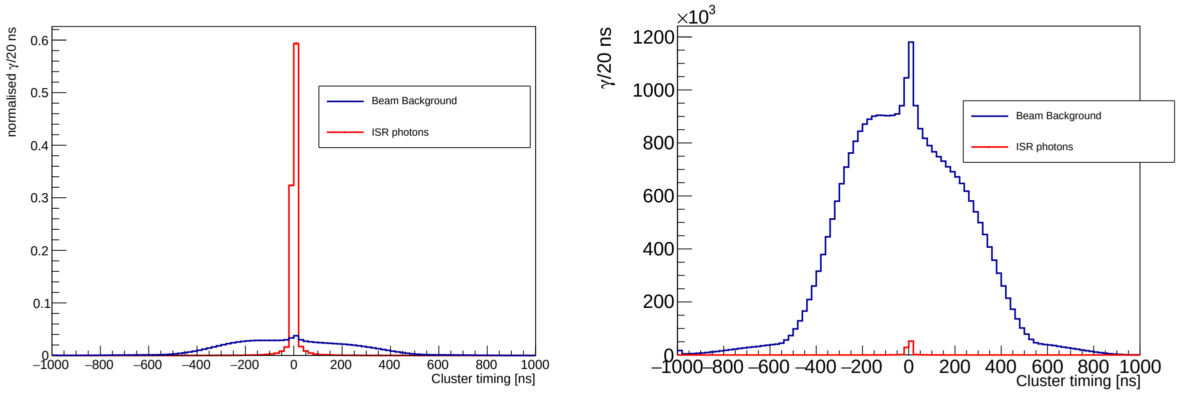

(c) Normalised cluster timing.

(d) unnormalised cluster timing.

Figure 4.8.: ECL Cluster timing for reconstructed photon candidates in the simulation of 500 k ISR $K_S K_L$ events with beam background. (a) shows candidates from ISR and (b) shows photon candidates from beam background. (c) shows the two plots normalised on the same plot while (d) shows them unnormalised.

Although a very large percentage of beam background candidates can be removed with a cut on cluster timing, the number of remaining photon candidates caused by beam background in the low energy range is still very large when compared to the number of reconstructed ISR photon candidates. As the cluster timing cut is made tighter it successfully removes more beam background candidates, but also removes many true ISR photon candidates as well.

Table 4.3 shows the number of events with a correctly reconstructed K_S, a K_L predicted to be in the acceptance of the KLM geometry and 2 reconstructed photons, where only the lower energy photon is required to pass cluster timing cuts. MC truth

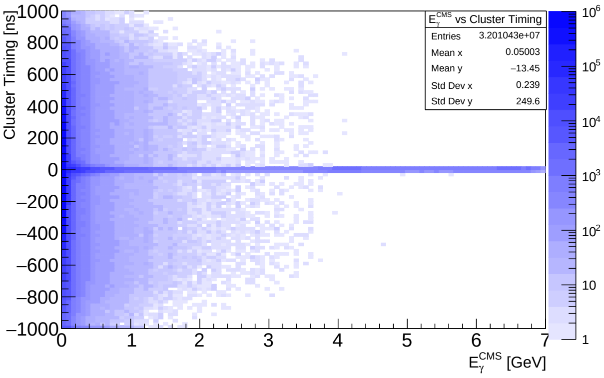

Figure 4.9.: The photon energy vs cluster timing. There is no correlation between photon energy and cluster timing.

Table 4.2.: Reconstructed photon candidates with $E_\gamma^{CMS} < 3$ GeV for 500 k events with beam background

Cluster timing cut	ISR candidates	Background candidates
No cut	30 049	31 424 150
$\lvert 200ns \rvert$	29 498	17 401 680
$\lvert 100ns \rvert$	28 436	9 284 568
$\lvert 50ns \rvert$	26 548	5 020 753
$\lvert 10ns \rvert$	19 443	1 219 017
$\lvert 1ns \rvert$	7897	207 512

Table 4.3.: The number of well-reconstructed events with two photons reconstructed from 500 k events with beam background.

Cluster timing cut	well-reconstructed two γ events	efficiency ϵ
No cut	1156	0.23%
$\lvert 200ns \rvert$	1149	0.23%
$\lvert 100ns \rvert$	1117	0.22%
$\lvert 50ns \rvert$	1046	0.21%
$\lvert 10ns \rvert$	826	0.17%
$\lvert 1ns \rvert$	368	0.07%

is used to select true ISR photons. Although cluster timing is able to remove beam background candidates at a greater rate than ISR candidates, requiring that cluster timing$< \lvert 1 \rvert\ ns$ for the lower energy ISR photon results in an efficiency of 0.07%, yet this cut still leaves a remaining 207 512 background photons in the sample. Although the cluster timing is initially effective at removing beam background photons over ISR, there is no cut that can be made that will result in more true ISR candidates than beam background candidates. It can be inferred that this will not allow the separation of low energy ISR photons from background, so instead, a lower bound energy cut of 3 GeV was used, as this effectively removes all beam background from the sample. Any lower energy ISR photons were treated as an energy loss in the rest of the event used to calculate the K_L 4-vector (more in Chapter 5).

4.5.2. K_S Reconstruction with Beam Background

Beam background has a dramatic effect on K_S reconstruction. Figure 4.10 shows the $\cos(\theta_{lab})$ distribution for successfully reconstructed K_S, both with and without beam background. The asymmetry in the distribution is a combined result of both the beam energy asymmetry and the asymmetry in the construction of the Belle II detector (this asymmetry can be seen in Figure 3.2).

To make it into the reconstructed K_S candidate list, it is required that the daughter pions of the K_S are both successfully reconstructed. Daughter pions of a K_S with a trajectory outside of the ECL may be reconstructed from tracks alone, or they may be bent into the ECL by the magnetic field. The events that are most likely to have a successfully reconstructed K_S have a K_S trajectory within the acceptance of the ECL. The red distribution seen in Figure 4.10, $\cos(\theta_{lab})$ for reconstructed K_S without beam background, is a result of the generated K_S distribution (Figure 4.2) filtered through the ECL geometry. K_S within the ECL acceptance are reconstructed with a high efficiency, whereas those outside this geometric acceptance are reconstructed with a very low efficiency. Even with this low efficiency, the two largest peaks in Figure 4.10 are close to the beam line, at the extreme bins, as this is where the majority of K_S lie in the generated distribution.

The barrel distribution (within the ECL) has an efficiency of roughly 10%, while the peaks at the edges of the distribution have an efficiency of roughly 1% (comparing Figure 4.10 to Figure 4.2). The rising distribution on the right hand side of the barrel distribution, peaking at roughly 0.9, is due to the increase in the number of K_S in the generated distribution closer to the edges of $\cos(\theta_{lab})$. The distribution then sharply falls at the boundary of the ECL (the second to last bin on the right hand side of Figure

4.10, corresponding to $\cos(\theta) = 0.98$). This same effect is visible in the backward direction, as a slow rise peaking at $\cos(\theta_{lab}) = -0.8$, but this is less pronounced due to the beam energy asymmetry pointing in the forward direction and the asymmetry in the construction of the ECL. The minimum on the left hand side of Figure 4.10, roughly corresponds to $\cos(\theta) = -0.91$, which is the boundary of the ECL in the backward direction.

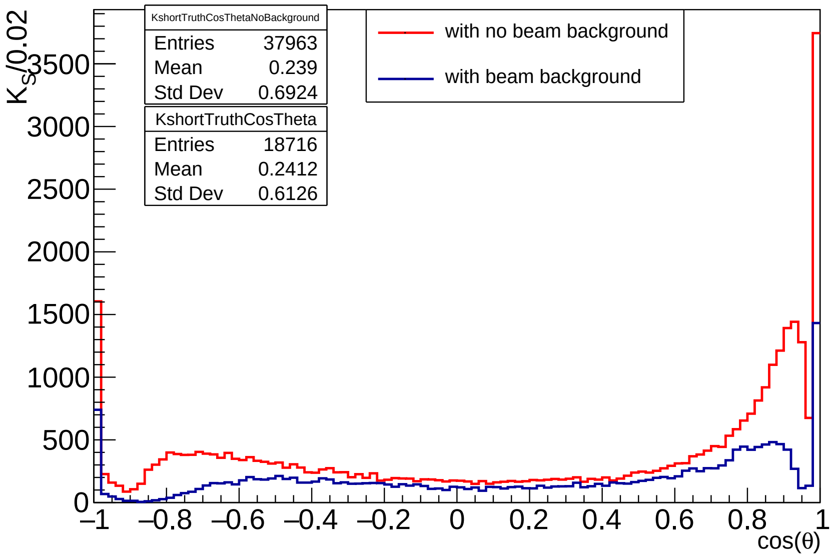

Figure 4.10.: The generated $\cos(\theta_{lab})$ distribution for correctly reconstructed K_S from the simulation with beam background (blue) and without beam background (red).

The effect of the addition of beam background can also be seen in Figure 4.10. The signals from beam background will tend to point close to the beam line. This means that the K_S, which are produced primarily at the edges of the $\cos(\theta_{lab})$ distribution, are likely to have beam background overlapping with the charged tracks and clusters from the K_S daughter pions, preventing clean pion reconstruction. Figure 4.10 shows a similar reconstruction efficiency with and without beam background for K_S in the middle of the $\cos(\theta_{lab})$ distribution, however there is a substantial drop in K_S efficiency due to beam background for K_S closer to the beam line. Where the sample with no beam background has 37 963 K_S reconstructed, the sample with beam background simulated only has 18 716 K_S reconstructed. 51% of previously reconstructable K_S are lost due to the effects associated with the addition of beam background.

Due to the reduction in ISR photon and K_S efficiency the number of well-reconstructed events decreases significantly when beam background is added. The beam background also introduces effects that mean the introduction of a lower level photon energy cut to separate photon candidates from beam background is required. This will also cause a reduction in well-reconstructed events. This will be further explored in Chapter 5.

Chapter 5.

Efficiency and Efficacy

This chapter will discuss the validity of this method of K_L energy determination and possible methods of increasing efficiency whilst maintaining energy determination accuracy.

It is important to consider how accurate this method of energy determination will be. In Equation 5.1 E_{K_L} is the K_L energy, $E_{e^+e^-}$ is the energy sum of the two incoming beams, E_γ is the energy of the emitted ISR photon and E_{K_S} is the K_S energy, all of which are lab frame energies. Naively, one might use equation 5.1 to determine the lab frame energy of the K_L, and for first order ISR events we would expect this to be effective, but given we expect that there will be missing energy due to unreconstructed second order ISR photons, this will result in a reconstructed energy for the K_L that is higher than the generated MC energy.

$$E_{K_L} = E_{e^+e^-} - (E_\gamma + E_{K_S}) \tag{5.1}$$

This chapter will discuss differences between MC generated energy and the energy value determined by the constraints of the rest of the event (reconstructed energies). The plots here always display $E^{gen} - E^{reco}$.

5.1. K_L Energy Excess

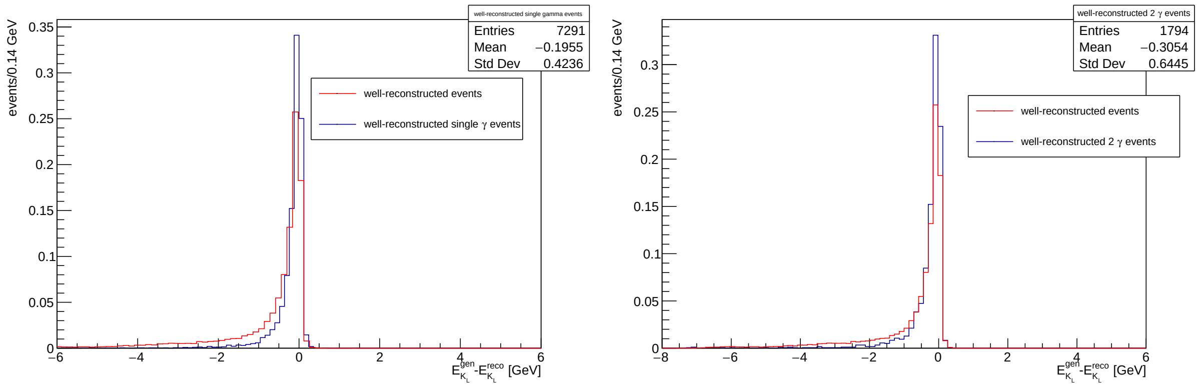

(a) All events (red) and single photon events (blue). **(b)** All well-reconstructed events (red) and events where 2 ISR photons are reconstructed (blue).

Figure 5.1.: The difference between the generated K_L energy and the reconstructed energy. These are from the sample of 500 000 events with no beam background. (a) compares all well-reconstructed events with well-reconstructed events where only one ISR photon is emitted in the MC generated sample, (b) compares all well-reconstructed events to events where 2 photons are successfully reconstructed. Both plots are normalised.

Figure 5.1 shows the difference between the generated MC value for K_L energy (E^{gen}) and the reconstructed energy (E^{reco}), for events in the simulation without beam background (the beam background was not included so that the second order ISR events could be examined, whereas with beam background the secondary lower energy ISR photons are not discernible from beam background). For the events in Figure 5.1, a K_L is required to be in the KLM, a reconstructed K_S is required in the K_S list and a correctly reconstructed ISR photon is required in the photon candidate list, but no minimum photon energy requirement is made. Figure 5.1 (b) requires 2 correctly reconstructed ISR photons. In Figure 5.1 it can be seen that the reconstructed K_L energy is systematically higher than the MC generated energy. There are two reasons for this: loss of secondary photons and incomplete electromagnetic shower reconstruction.

5.1.1. Loss of Secondary Photons

As demonstrated in the previous chapter, there is no correlation between primary and secondary photon polar angle. Given this, the second order ISR events are most likely only going to have one correctly reconstructed ISR photon. As such, the second, missing ISR photon presents itself as an energy loss in the rest of the event that is used to determine the K_L energy.

Figure 5.1 (a) shows the difference between generated and reconstructed K_L energy, comparing the distribution for all well-reconstructed events to single ISR photon events. From this, it can be seen that by selecting single photon events, there is a noticeable drop in the high K_L energy excess events in the tail of the distribution i.e. events where the reconstructed value of K_L energy is significantly larger than the generated energy. This is because selecting single photon events removes events where only the secondary, lower energy, ISR photon is reconstructed. Figure 5.1 (b) shows the distribution for events where both ISR photons are reconstructed and used to reconstruct the K_L energy. This shows a significant reduction in the tail of the distribution of K_L energy excess for the same reasons as the single photon distribution. Neither of these show the gaussian distribution that one would expect were the entirety of the rest of the event being reconstructed correctly.

Given that there is a systematic excess in reconstructed K_L energy, both for events where only a single ISR photon is emitted in MC truth, and for events where both ISR photons are reconstructed and used for determining K_L energy, it can be inferred that secondary ISR photon loss can not be the only source of energy loss. The second source of energy loss in the event is the incomplete reconstruction of the ISR photon EM shower.

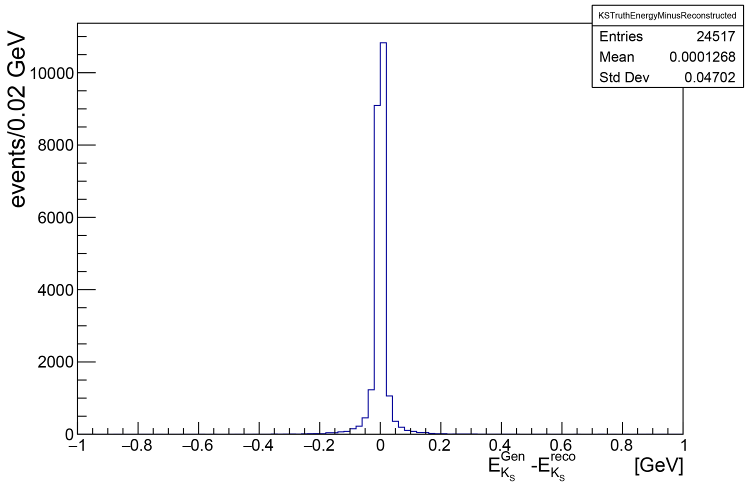

Figure 5.2.: The difference between the K_S generated energy and the reconstructed K_S energy for the simulation of 500 000 ISR K_SK_L events with beam background.

5.1.2. Photon Shower loss

Figure 5.2 shows the plot of the difference between reconstructed K_S energy and generated energy, which exhibits a gaussian around zero, so it can be inferred that the K_S is not the source of systematic K_L energy excess. The plot of $E_\gamma^{gen} - E_\gamma^{reconstructed}$ for the ISR photons, Figure 5.3 (a), is quite different, and shows a reconstructed energy that is systematically smaller than the generated energy. This is caused by a partial loss of the components of the electromagnetic shower used to reconstruct the photon, leading to a final reconstructed photon energy that is lower than the generated energy. This can be seen in Figure 5.3 (b), where the photon energy loss is most prominent at the boundaries of the ECL and at the 1 degree gap between the barrel and endcap ($\cos(\theta_{lab}) = 0.85, -0.66$). This is the region where we would expect some portion of the EM shower to be lost outside the detector geometry. This effect is particularly pronounced in this analysis because the $\cos(\theta_{lab})$ distribution of the ISR photons is essentially collinear with the beam direction. The photons in ISR processes at Belle II are far more likely to lose shower components than non ISR events, as, in ISR events, the edges of the ECL are where the photon angular distribution is maximum.

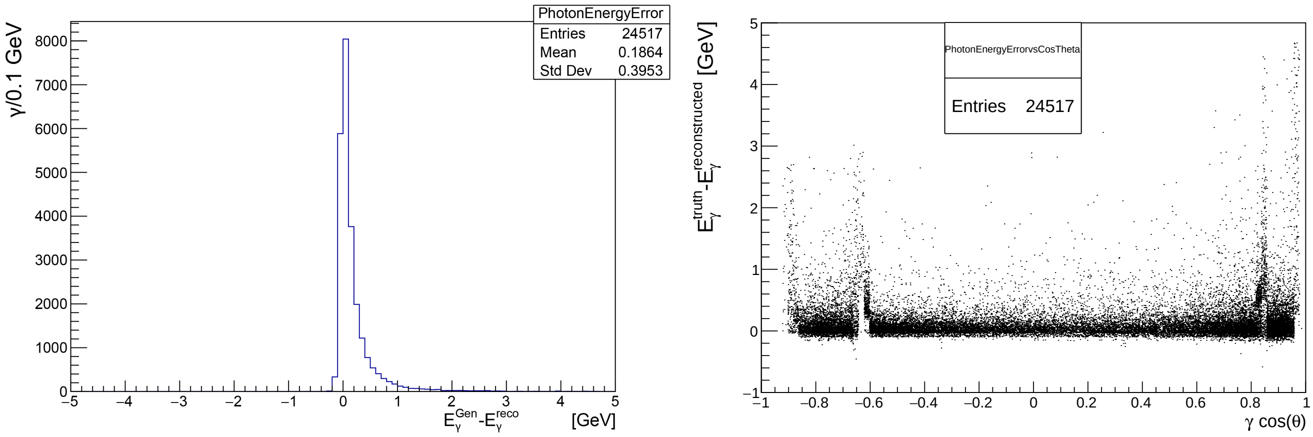

(a) The difference between the MC generated ISR photon energy and the reconstructed photon energy.

(b) The difference between the MC generated ISR photon energy and the reconstructed photon energy vs the ISR photon MC generated energy $\cos(\theta_{lab})$.

Figure 5.3.: (a) shows the MC generated photon energy minus the reconstructed energy. (b) displays the MC generated photon energy minus the reconstructed energy vs the generated $\cos(\theta)$ distribution of the ISR photon. There is a significant loss of photon energy at the edges of the ECL endcap and at the gap between the ECL endcap and barrel. The ECL edges correspond to $\cos(\theta) = 0.98, -0.91$ and the gaps correspond to $\cos(\theta) = 0.85, -0.66$.

5.2. CMS Photon Energy Cut

From this point forward, all plots are from the simulation of 500 000 ISR $K_S K_L$ events including beam background. MC truth information is only used for the cut requiring that the K_L fall within the geometry of the KLM. This is so that the accuracy of the K_L energy reconstruction can be understood in terms of real world cuts that will be applied to real data. This means reconstructed particles are not matched to MC generated particles.

Due to the beam background photon candidate energy distribution discussed in the previous chapter, an ISR photon minimum energy cut of 3 GeV is also applied. As discussed previously, the probability of reconstructing both photons in a second order ISR events is quite low, so the reconstruction of both photons in two photon ISR events is not pursued. In the CMS frame, the energy of the system needs to drop from 10.58 GeV, the $\Upsilon(4S)$ mass, to 1019 MeV, the ϕ mass. A lower bound cut on the primary ISR photon CMS energy functions effectively as an upper bound cut on the loss from secondary ISR photon energy. This removes events where there is a lost, secondary, ISR photon with a significant amount of the energy of the event.

To mitigate the loss of energy in the photon's EM shower at the edges and the gap region of the ECL, one might be tempted to implement a cut in $\cos(\theta)$. Due to the angular distribution of ISR photons, this kind of cut would remove a large percentage of the good signal photons as well. Given that the incorrectly reconstructed photons at the boundary are losing energy, by implementing the previously mentioned lower bound energy cut, the reconstructed photons that report a lower energy than the generated energy will be removed from the sample, so this instead was pursued.

5.3. Selecting for Primary ISR

For the reason described above, a 5.2 GeV CMS energy cut to ISR photons is effective in reducing the excess in reconstructed K_L energy from both missing ISR photons and from lost shower components. This cut effectively selects for primary ISR events (or events with a very small energy loss) as the CMS energy of the ISR photon in a first order ISR event is 5.24 GeV. This can be seen in Figure 5.4, which shows the K_L generated minus reconstructed energy for varying E_γ^{CMS} cuts. Whilst increasing this cut does reduce the yield of well-reconstructed events, the larger the CMS cut the lower the K_L energy excess. The yield of events for a 5.2 GeV CMS photon energy

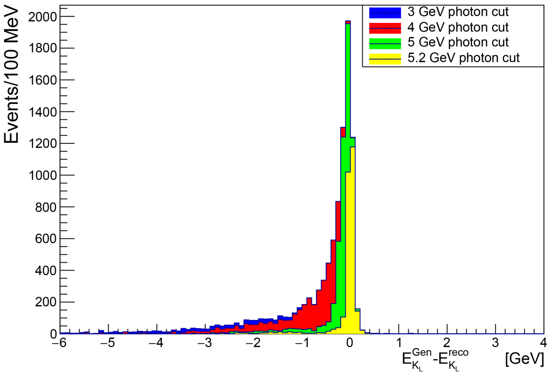

Figure 5.4.: The difference between generated and reconstructed K_L energy for differing E_γ^{CMS} cut for well-reconstructed events in 500 000 ISR $K_S K_L$ events with beam background.

cut is shown in Table 5.1 and the generated minus reconstructed K_L energy is shown in Figure 5.4. The selections that have been imposed on the data in Table 5.1, where applicable are as follows:

- A reconstructed K_S in the K_S list
- A reconstructed ISR photon with $E_\gamma > 5.2$ GeV, within the CDC geometry ($17^\circ < \theta < 150^\circ$)
- A K_L generated within the KLM geometry ($20^\circ < \theta < 155^\circ$)

Table 5.1.: The yield of events for each requirement applied to events with beam background and a 5.2 GeV ISR CMS photon cut.

Events with:	# Events	Events with:	# Events
	500 000	ISR γ and K_S	3 708
ISR γ	13 817	ISR γ and K_L	12 824
K_S	32 172	K_S and K_L	16 373
K_L	71 674	γ and K_S and K_L	3 677

Using 3 677 events out of 500 000 as the measure of efficiency (ϵ) and multiplying by the ISR ϕ production cross section and the $\phi \to K_L K_S$ branching fraction, the expected number of events per inverse femtobarn of luminosity produced at Belle II is obtained. The uncertainty in the determined value for ϵ is assumed to be equal to the Poisson fluctuations.

$\epsilon = \frac{\text{number of events that could be used for calibration}}{\text{total number of ISR events}} = \frac{3677}{500000} = (0.74 \pm 0.01)\%$. The ISR ϕ production cross section is $\sigma = (0.0241 \pm 0.0003)nb$ [34] and $B(\phi \rightarrow K_S K_L) = 0.342 \pm 0.004$ [26]. The expected number of events per inverse femtobarn of luminosity is 61 ± 3.

This is likely too a low number of events to carry out a calibration with phase II data, especially considering phase II of data production produced only 472 pb^{-1} of integrated luminosity, when the initial hope was that this phase would yield around 30 fb^{-1}.

5.4. K_L Energy Range

Another issue with the 5.2 GeV cut is that the energy range in which these K_L are produced is much higher than the K_L that are expected to be produced in Belle II $B\overline{B}$ events. Figure 5.5 (a) shows the generated $\cos(\theta_{lab})$ vs energy distribution, for K_L in well-reconstructed ISR events with $E_\gamma^{CMS} > 5.2$ GeV. The $\cos(\theta_{lab})$ distribution is included as the endcaps are designed differently to the barrel, and one would expect the signal to behave differently in different sections, so each section must be considered separately. The beam asymmetry can be seen as a rising K_L energy in the forward direction. Figure 5.5 (b) shows the generated $\cos(\theta_{lab})$ vs energy distribution of K_L in a sample of 2 million B MC events produced by the Belle II collaboration [1]. These data are comprised of 1.1 million charged B pairs and 990 000 neutral B pairs. This is to match the branching fractions of the $\Upsilon(4S)$: 51.4% for charged B pairs and 48.6% for neutral B pairs [26].

It can be seen that the energy of the K_L in the majority of the $E_\gamma^{CMS} > 5.2$ GeV sample is generally higher than that of K_L found in B meson decays. This difference in energy may be less problematic than it might initially seem. Although the lack of overlap in energy is not ideal, were one to calibrate, not with number of deposits in a cluster, but with cluster timing information, then it is intuitive that a kinematic relationship between KLM cluster timing and K_L energy could be extrapolated to lower energy K_L. This is currently being considered for the KLM endcap K_L reconstruction algorithm. To determine the nature of this kind of relationship, not only is it advantageous to determine the efficacy of the timing relationship for a sample with low K_L energy, but also with a sample with a large range in K_L energy. If there is a consistent relationship

---

[1] The sample named “MC7” available on the KEKCC system.

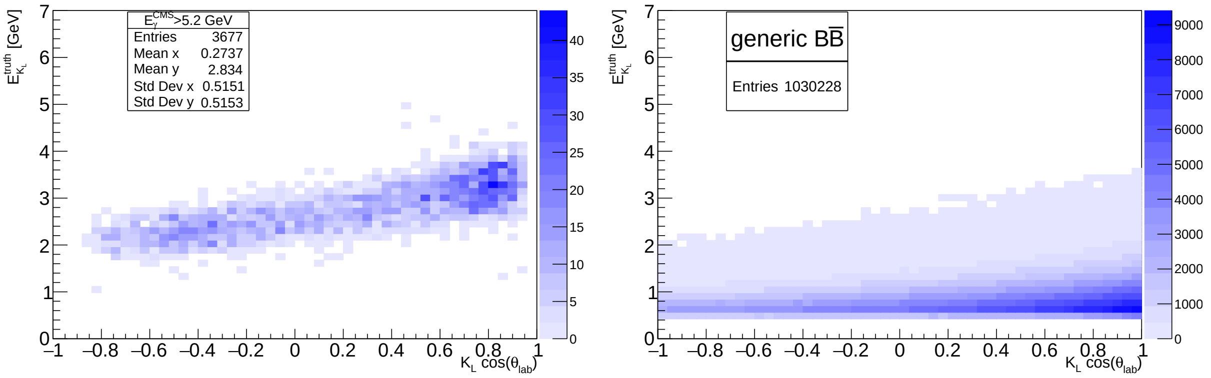

(a) Well-Reconstructed calibration K_L with $E_\gamma^{CMS} > 5.2$.

(b) K_L in generic MC $B\overline{B}$ decays

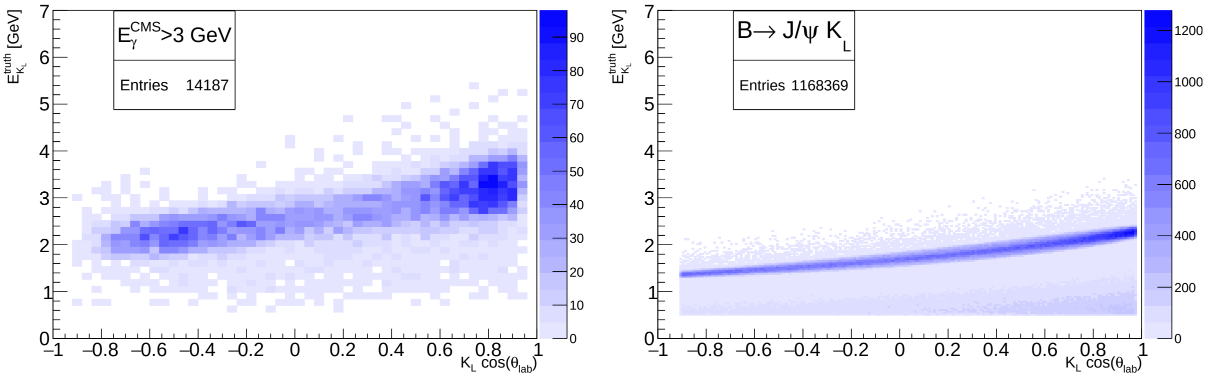

(c) well-reconstructed calibration K_L with $E_\gamma^{CMS} > 3$.

(d) K_L in $B \to J/\psi K_L$ events.

Figure 5.5.: The K_L generated $\cos(\theta)$ vs generated K_L energy. (a) and (c) show the distribution of K_L produced in 500 000 ISR $K_S K_L$ events, with an ISR CMS energy cut of 5.2 GeV and 3 GeV respectively. (b) shows the distribution for K_L produced in 2 million generic MC $B\overline{B}$ decays, with both charged and neutral B mesons. (d) shows the distribution for the K_L in a simulation of 1 million $B \to J/\psi K_L$ events.

between timing and energy, it would be expected to hold, even for larger K_L energy, making these events useful for testing the validity of the determined relationship. Lower energy K_L will still better test the efficacy of using the determined relationship for low energy K_L so it is desirable to increase the yield of low energy K_L as much as possible.

Figure 5.5 (d) shows the $\cos(\theta_{lab})$ vs energy distribution for K_L in 1 million $B \to J/\psi K_L$ events produced with EvtGen (the combination of $B \to J/\psi K_L$ and $B \to J/\psi K_S$ is often referred to as a golden channel for CP violation). This is included to show that, events of interest where the K_L is high in the decay chain, will likely include higher energy K_L than the $B\overline{B}$ events in Figure 5.5 (b), so the lack of energy overlap with the general distribution of $B\overline{B}$ events is not necessarily troublesome if one were to use this calibration for a decay channel with a K_L as a primary particle decaying from the B or $\overline{B}$. Unfortunately, the majority of events in (d) still do not overlap significantly in energy with those in (a).

5.5. Lowering the ISR Energy Cut

To increase the number of well-reconstructed calibration events, the simplest method is to lower the ISR energy cut to accept more second order ISR events. This also has the added advantage of allowing events with a lower K_L energy into the sample, as can be seen when comparing Figure 5.5 (a) and (c). This does however, reintroduce events with a large excess in the reconstructed K_L energy (see Figure 5.4). The number of well-reconstructed events for different possible ISR CMS energy cuts is displayed in Table 5.2.

Table 5.2.: The number of well-reconstructed events for different E_γ^{CMS} cuts.

E_γ^{CMS} cut [GeV]	well-reconstructed events
3	14 187
4	13 310
5	8 702
5.2	3 677

The following plots are of 500 000 events requiring a reconstructed K_S, a K_L within the KLM acceptance and an ISR photon with $E_\gamma^{CMS} > 3$ GeV within the CDC acceptance, so as to remove background photons (although some may have a higher ISR CMS cut where specified).

5.5.1. Correcting for Lost Photon Energy

The 5.2 GeV ISR energy cut is effective at removing events with an incorrectly reconstructed K_L energy, but rather than simply remove events with incorrectly reconstructed K_L energy in this way, it is possible to use the ISR photon energy to determine how much energy we expect is missing, and correct for the K_L energy excess.

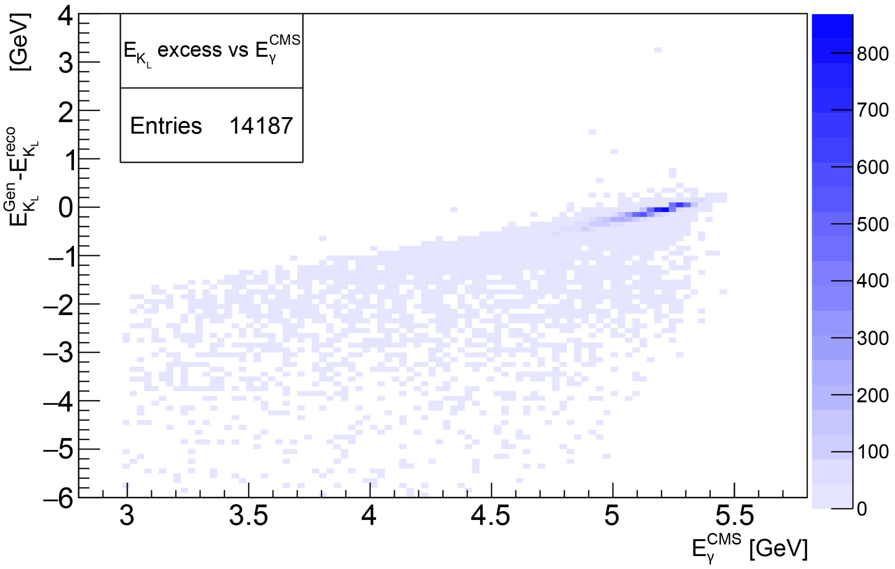

Figure 5.6.: The CMS ISR photon energy vs the difference between generated and reconstructed K_L energy, for well-reconstructed events.

There are two major sources of the energy excess that have been discussed and these both present as a lower than expected ISR photon CMS energy, and as such, can be combined into one factor, $E_{\gamma_{miss}}$.

Figure 5.6 shows the relationship between the CMS energy of the ISR photon and the reconstructed K_L energy excess. The majority of the distribution appears to follow a linear relationship. The reason for this is as follows: $E_{e^+e^-}$ is defined as the e^+e^- system energy, E_{K_S} as the K_S energy and $E_{\gamma_{vis}}$ is defined as the ISR photon energy seen in the event. $E_{\gamma_{miss}}$ is defined as the missing energy from the combined effect of missing secondary ISR photons and energy loss from incorrectly reconstructed photons. With this, the generated and reconstructed energies can be written as Equations 5.2 and 5.3. Subtracting equation 5.3 from 5.2 yields Equation 5.4. These hold true in any reference frame.

$$E_{K_L}^{gen} = E_{e^+e^-} - (E_{\gamma_{vis}} + E_{\gamma_{miss}} + E_{K_S}) \tag{5.2}$$

$$E_{K_L}^{reco} = E_{e^+e^-} - (E_{\gamma_{vis}} + E_{K_S}) \tag{5.3}$$

$$E^{gen}_{K_L} - E^{reco}_{K_L} = -E_{\gamma_{miss}} \tag{5.4}$$

In the CMS frame, assuming the production of a ϕ meson and, either primary ISR or two ISR photons emitted from the same beam, the total ISR photon energy should be 5.24 GeV, giving Equation 5.5. This is only accurate for photon energy lost from photon shower loss and secondary photon loss in the case where both ISR photons are emitted from the same initial beam. This is not accurate for events where the two ISR photons are back to back, as the total photon energy in these events may be more than 5.24 GeV.

$$E^{CMS}_{\gamma_{miss}} = 5.24GeV - E^{CMS}_{\gamma_{vis}} \tag{5.5}$$

Equation 5.5 is only true in the CMS frame, whereas the quantity of interest is the lab frame K_L energy. Based on Figure 4.1 (a), it can be assumed, in general, that the missing photon energy vector is approximately either parallel or anti-parallel to the electron beam, and therefore, to the Lorentz boost vector between the CMS and lab frame. Boosting into the lab frame, the missing energy is then given by Equation 5.6. Substituting in Equation 5.5 and 5.4 yields Equation 5.7.

$$E^{lab}_{\gamma_{miss}} = \gamma(1-\beta)(E^{CMS}_{\gamma_{miss}}) \tag{5.6}$$

$$E^{\text{lab gen}}_{K_L} - E^{\text{lab reco}}_{K_L} = \gamma(1-\beta)(E^{CMS}_{\gamma_{vis}} - 5.24GeV) \tag{5.7}$$

At Belle II the β factor describing the velocity of the boost from CMS to lab frame is given by $\beta = \frac{v}{c} = \frac{p_{e^+e^-}}{E_{e^+e^-}} = 0.276$ and the gamma factor is given by $\gamma = \frac{1}{\sqrt{1-\beta^2}} = 1.04$ If the missing energy vector is parallel to the boost, then β is positive, whereas if it is anti-parallel then β is negative.

The result is two lines, one for each possible direction of ISR emission. Figure 5.7 shows the $E^{gen}_{K_L} - E^{reco}_{K_L}$ vs E^{CMS}_{γ} distribution with these two lines plotted over the top. This Figure also has a zoomed in y axis, to better show the smaller scale behaviour

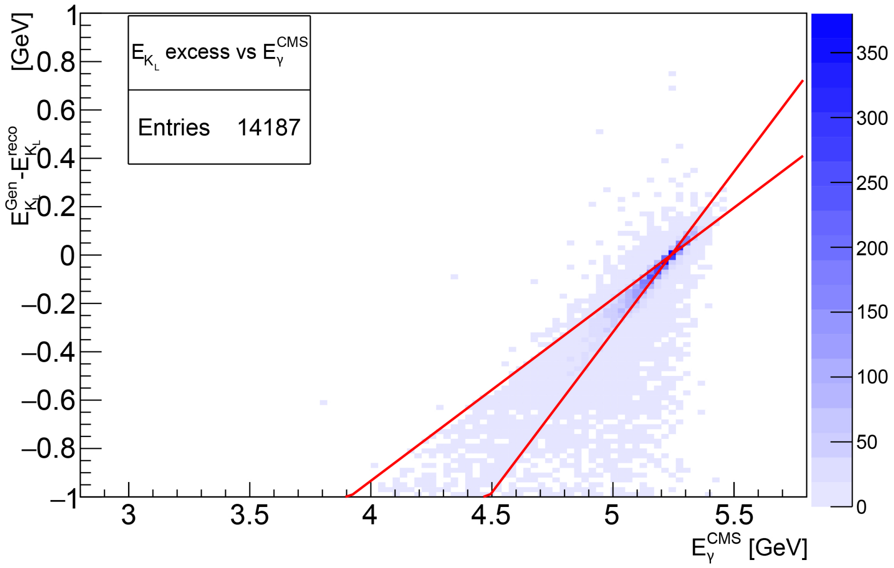

Figure 5.7.: The CMS ISR photon energy vs the difference between generated and reconstructed K_L energy, for well-reconstructed events. The two plotted lines represent the expected distribution of K_L excess and are given by $E_{K_L}^{\text{lab gen}} - E_{K_L}^{\text{lab reco}} = 1.04(1 \pm 0.276)(E_{\gamma_{vis}}^{CMS} - 5.24)$.

of the distribution. The events between these lines are the events where the missing energy vector has a non-zero component perpendicular to the boost direction.

The excess in reconstructed K_L energy from this effect can be corrected for by moving into the CMS frame, taking the ISR photon unit vector and setting the photon energy to 5.24 GeV, then boosting back into the lab frame. The corrected distribution of $E_{K_L}^{gen} - E_{K_L}^{reco}$ vs E_γ^{CMS} can be seen in Figure 5.8.

The difference between the generated and reconstructed K_L energy, before and after the lost photon energy correction, is shown in Figure 5.9. After the correction is applied there are still some events with a large excess in reconstructed K_L energy, however, the number of events with a large excess is greatly reduced and events that previously had a large excess now populate the bins with smaller K_L energy excess. Between Figure 5.9 (a) and (b), the bin with the smallest excess in K_L energy more than quadruples, from roughly 2000 events to over 9000 events after the correction is applied. As mentioned previously, this is not a perfect correction due to the events where the two ISR photons are back to back i.e. the vertical curved line in Figure 4.4 (b). In these events the total photon energy is not necessarily 5.24 GeV, and so the correction is based off of an incorrect assumption about the missing photon's

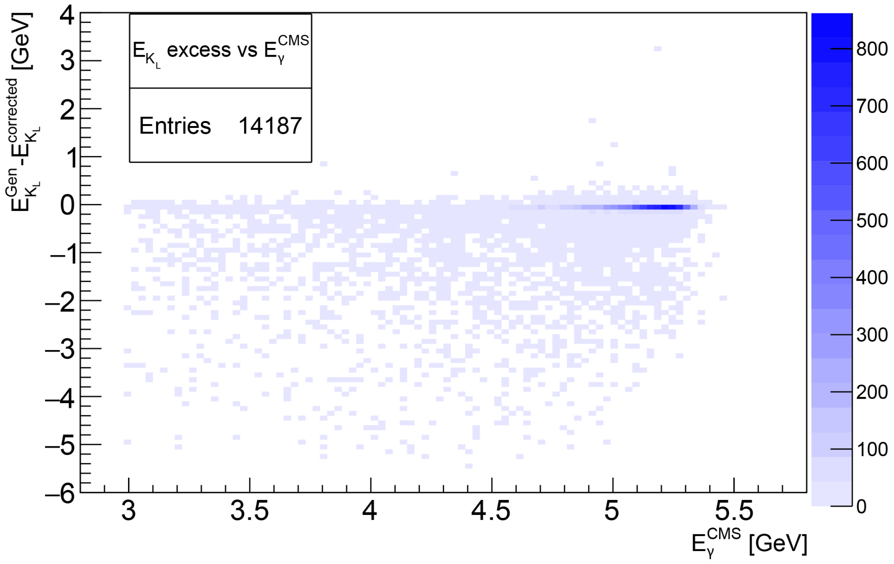

Figure 5.8.: The CMS ISR photon energy vs the difference between generated and reconstructed K_L energy, for well-reconstructed events after the photon energy correction is applied.

energy. This correction does however apply to the diagonal line in Figure 4.4 (b) and to energy loss from incomplete photon shower reconstruction. For events where the assumptions used in the correction hold true, there may still be a small error due to the nonzero angle between the reconstructed ISR photon and the missing energy vector.

5.6. Removing Events with a Large K_L Energy Excess

Figure 5.10 shows the MC generated energy of all K_L in the well-reconstructed distribution compared with the K_L energy of events with a K_L energy excess (after correction) greater than 1 GeV i.e. the events in the tail of Figure 5.9 (b). Although the tail makes up a small percentage of total events, these "tail" events constitute the majority of the events with a K_L energy below 2 GeV. This is because the low K_L energy events are most likely the events with photons back to back, thus the correction method described above is incorrectly assuming a total CMS ISR photon energy of 5.24 GeV and consequently, a lower than expected missing ISR photon energy. Most of these events will present themselves in the upper range of the corrected energy distribution. In Figure 5.10 (b) the events with a corrected K_L energy greater than 5 GeV are almost entirely events in the tail distribution. This means the incorrect reconstructed K_L

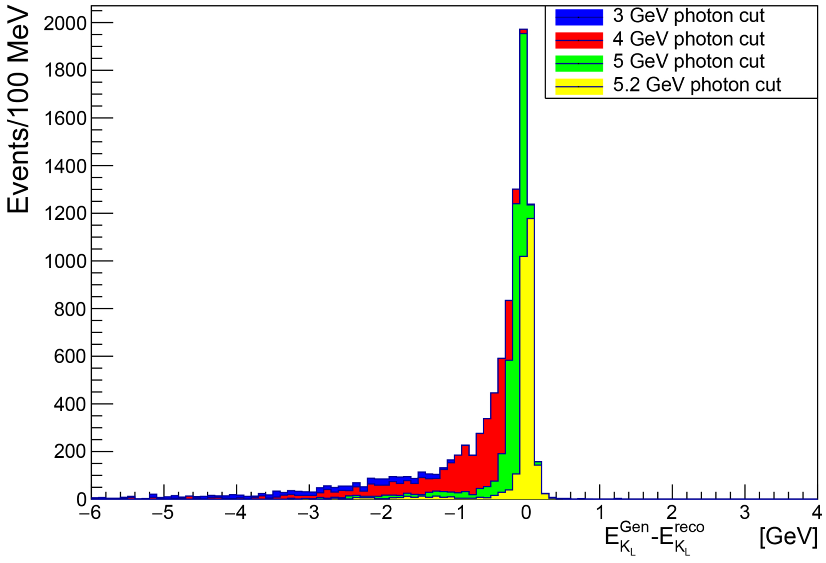

(a) Before the photon CMS energy correction is applied

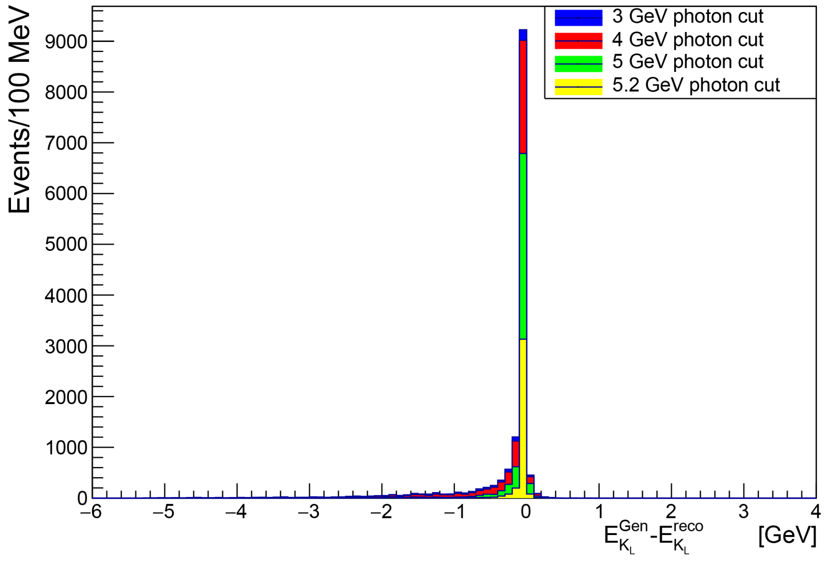

(b) After the photon CMS energy correction is applied

Figure 5.9.: The difference between the generated and reconstructed K_L lab frame energy, for different E_γ^{CMS} cuts, before (a) and after (b) the photon CMS energy correction is applied.

energy is returning low K_L generated energy events as high K_L reconstructed energy events. This is motivation for an upper level cut on reconstructed K_L energy. This is especially attractive as we would already be less interested in K_L with high energy for analyses involving $B\overline{B}$ decays.

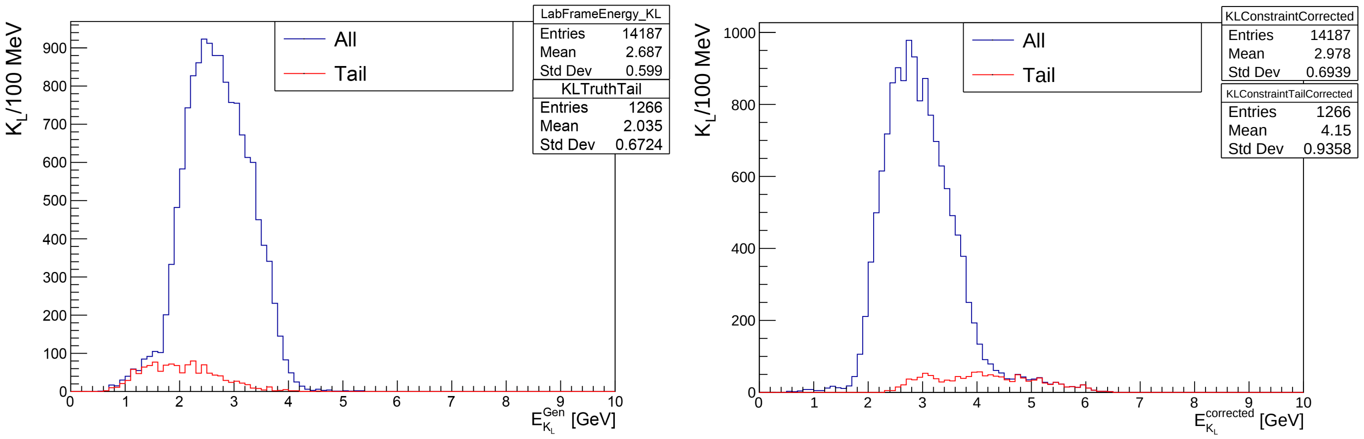

(a) MC generated K_L energy

(b) Reconstructed K_L energy, after the photon CMS energy correction is applied

Figure 5.10.: The K_L lab frame energy for all well-reconstructed events (blue) and the K_L lab frame energy for "tail" events (red), tail events being defined as events with K_L energy excess greater than 1 GeV. (a) shows the MC generated K_L energy and (b) shows the reconstructed K_L energy. Low MC generated K_L energy events return a high reconstructed K_L energy.

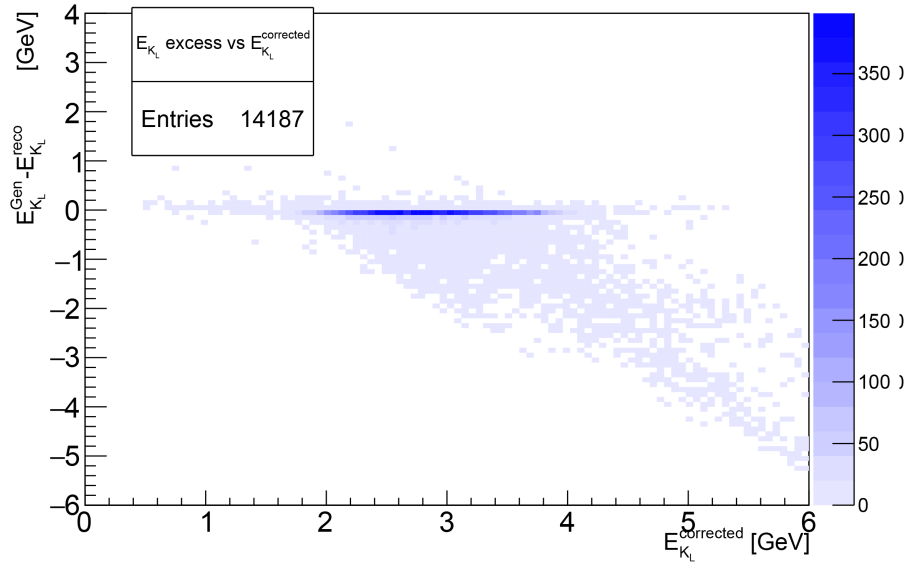

Figure 5.11.: The reconstructed K_L energy, after the photon CMS correction vs the difference between the MC generated and reconstructed K_L energy.

5.6.1. Upper K_L Energy Cut

From Figures 5.10 and 5.11 it can be seen that the low energy K_L are incorrectly returned as events with a large K_L energy. By not using the high energy K_L events, the worst of the K_L excess is removed with little loss of low energy, low excess events.

Figure 5.11 shows the relationship between the reconstructed K_L energy (after correction) and the reconstructed K_L energy excess. Above a K_L energy of 4.2 GeV, it is clear that the majority of events have an incorrect reconstructed K_L energy, even after correcting the photon energy. Figure 5.12 shows the effect that the implementation of a 4.2 GeV upper level K_L energy cut has on the reconstructed K_L energy excess after correction.

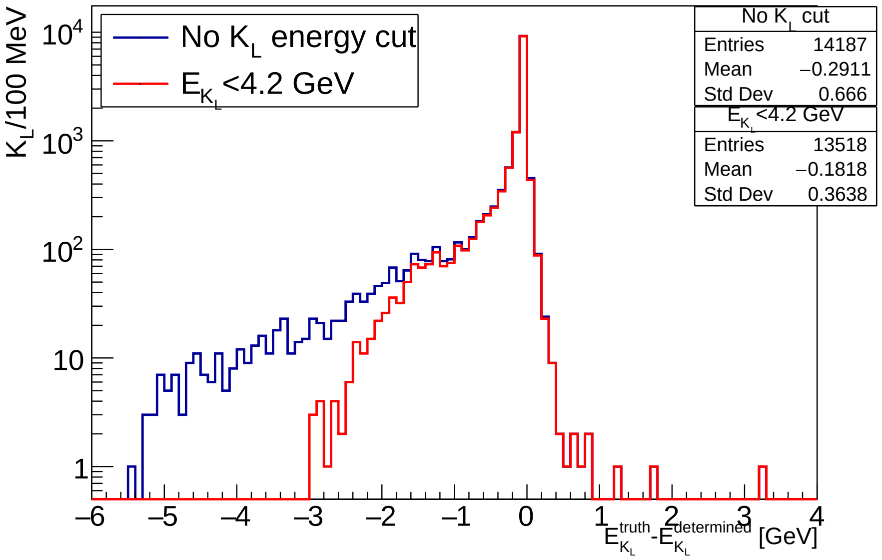

Figure 5.12.: The difference between MC generated K_L energy and the reconstructed K_L energy after the CMS photon correction, for all well-reconstructed events (blue) and for events where $E^{corrected}_{K_L} < 4.2$ GeV (red).

This cut removes the events with a reconstructed energy excess greater than 3 GeV ($E^{gen}_{K_L} - E^{corrected}_{K_L} < -3$ GeV), but the effect on events with an excess between 1 and 3 GeV could still be improved upon. This is because the 4.2 GeV cut does not take into account the boost into the CMS frame. Boosting an unknown and likely incorrect vector comes with a series of issues. It is simpler instead to use the angular information of the cluster left by the K_L to approximate the upper level of the distribution in Figure 5.13 (a).

Figure 5.13 shows the K_L $\cos(\theta_{lab})$ vs K_L energy distributions for generated energy in (a) and reconstructed energy in (b). The upper level of the generated population, curves upward, from around 2.7 GeV at $\cos(\theta_{lab}) = -1$ up to 4.2 GeV at $\cos(\theta_{lab}) = 1$. The distribution above this curve, in the reconstructed energy plot, will be populated with a majority of events with incorrectly reconstructed energy. This can be inferred from the fact that there is a low number of events in this region in the generated energy plot, Figure 5.13 (a), but a larger number of events in this region in the reconstructed energy plot, Figure 5.13 (b).

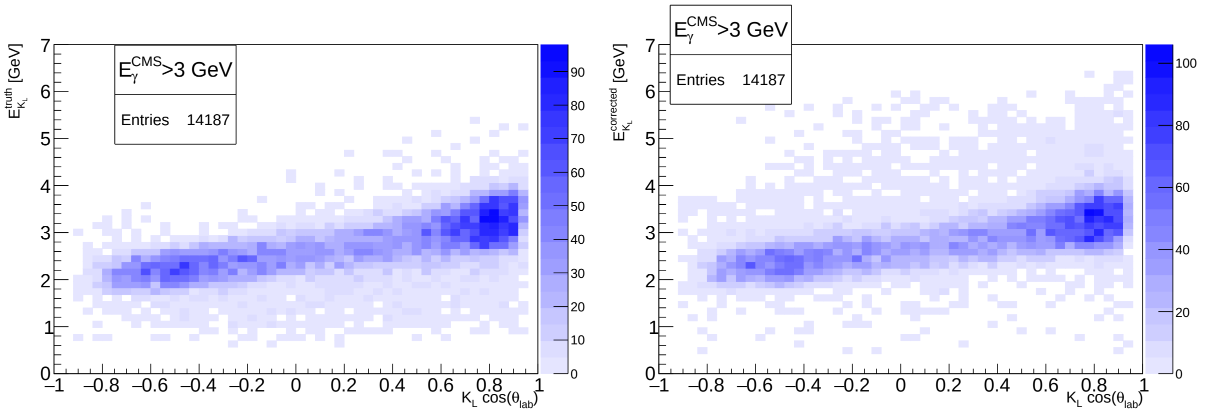

(a) K_L $\cos(\theta_{lab})$ vs generated K_L energy

(b) K_L $\cos(\theta_{lab})$ vs reconstructed K_L energy (after correction)

Figure 5.13.: MC generated $\cos(\theta_{lab})$ vs E_{K_L} for a 3 GeV ISR photon cut. (a) shows the MC generated K_L energy and (b) shows the reconstructed K_L energy. Events with incorrectly reconstructed E_{K_L} that are present in the lower energy area of the generated energy distribution in (a) are present in the upper energy area of the reconstructed energy distribution in (b)

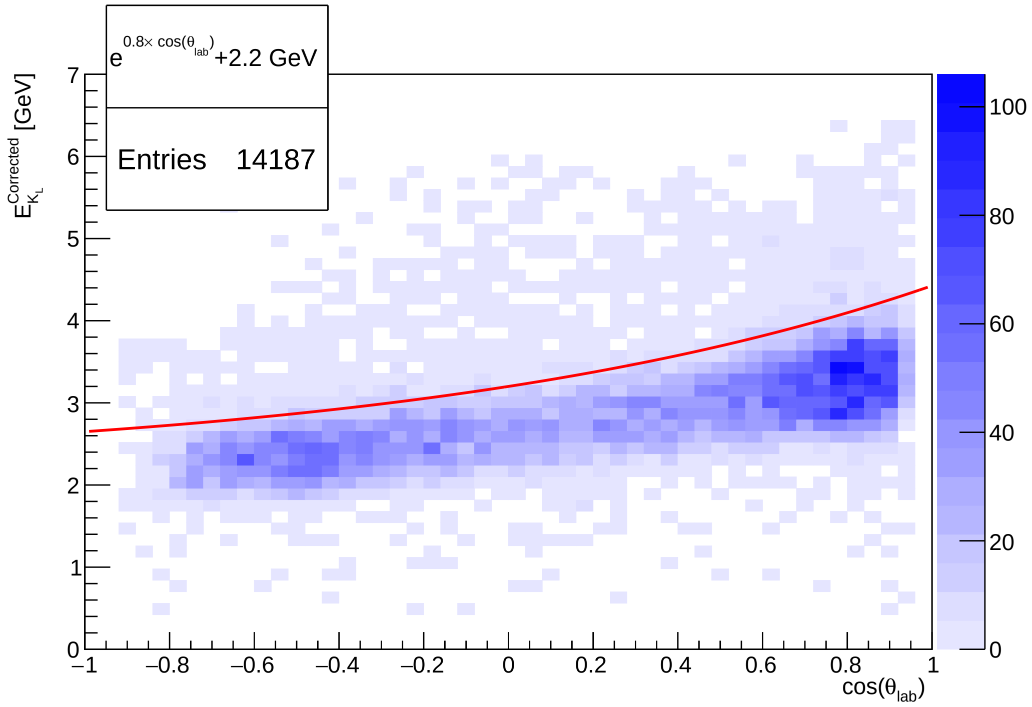

Figure 5.14.: MC generated K_L $\cos(\theta_{lab})$ vs reconstructed K_L energy after the photon CMS correction, with the function $E_{K_L} = (e^{0.8\cos(\theta_{lab})} + 2.2)$ GeV plotted. The majority of events above this line are known to have an inaccurate reconstructed K_L energy.

The upper level of this distribution was modelled with an exponential of $\cos(\theta_{lab})$ and events above this were removed. The events removed by this cut have a more

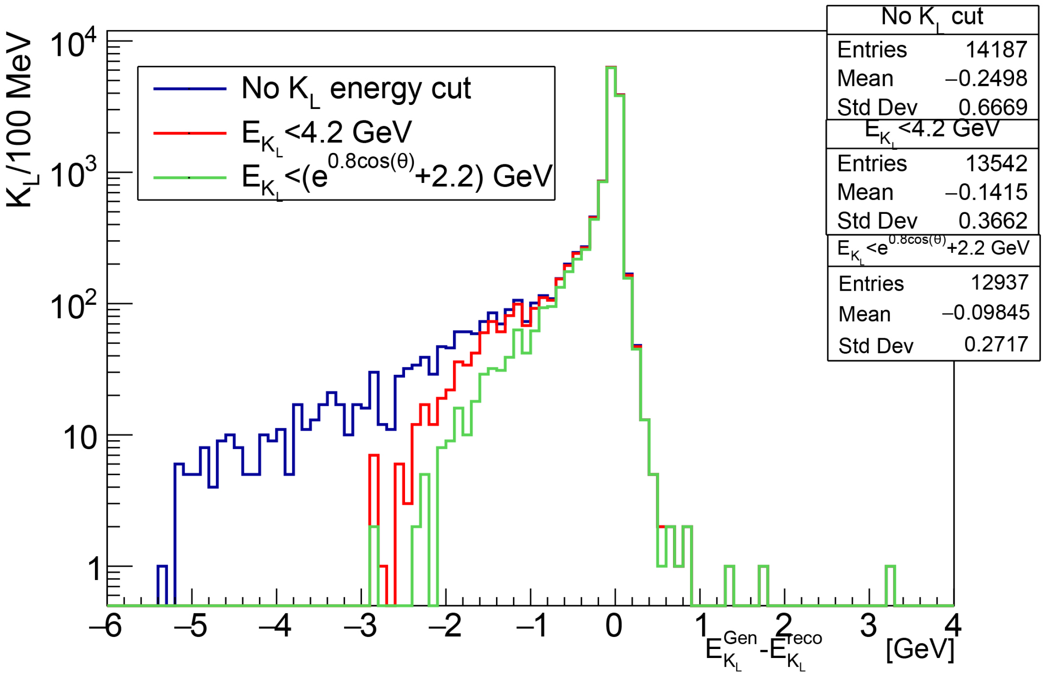

Figure 5.15.: The difference between generated and corrected K_L energy, for all well-reconstructed events, after the photon CMS correction, for all well-reconstructed events (blue) and then also for $E^{corrected}_{K_L} < 4.2$ GeV (red) and for events where $E^{corrected}_{K_L} < (e^{0.8\cos(\theta_{lab})} + 2.2)$ GeV (green).

significant effect on the tail. These events are also in the upper energy range and so less important to calibration. This fit was done by adjusting the fit parameters by eye. The function was determined to be $E_{K_L}^{corrected} = e^{0.8\cos(\theta_{lab})} + 2.2$ GeV. Figure 5.15 shows the improvement in reconstructed K_L energy for the cut using the exponential fit, over the 4.2 GeV energy cut, specifically between around 0.5 and 3 GeV K_L energy excess.

5.7. Reconstructed K_L Angle and Distance from KLM Cluster

In the previous section, the accuracy of the energy determination was discussed. If the same method is used to determine the K_L direction, using the 4-momentum constraints of the rest of the event, then there will, as with the reconstructed K_L energy, be an error in the K_L reconstructed angle due to missing photon energy. Figure 5.16 shows the difference in ϕ and θ between the generated MC K_L 4-vector and the K_L 4-vector reconstructed with the process described here. This is for well-reconstructed events, after the CMS photon energy correction is applied.

The difference in θ is larger than the difference in ϕ. This is explained by the fact that we expect a larger z component of the missing photon momentum than x or y. In Figure 5.16, the difference between the generated and reconstructed value for ϕ and θ both centre at 0, with a fairly small spread. This will be discussed further in the final section of this chapter.

5.7.1. KLM Cluster Angle

Figure 5.17 shows the polar and azimuthal angle difference between the generated K_L vector and the KLM cluster that is closest to the generated K_L vector. This distribution has a significant spread. The reason for this is that the formation of a hadronic cluster may not necessarily be symmetrical and thus the cluster centroid can be offset from the K_L vector. Hits in the KLM are grouped together into a cluster if they are within 5 degrees of each other and in the case of this channel, if the pions are close to the K_L, there is a chance that the pions may leave hits in the KLM that are grouped with the K_L cluster. This would cause the centroid of the cluster to shift away from the true K_L.

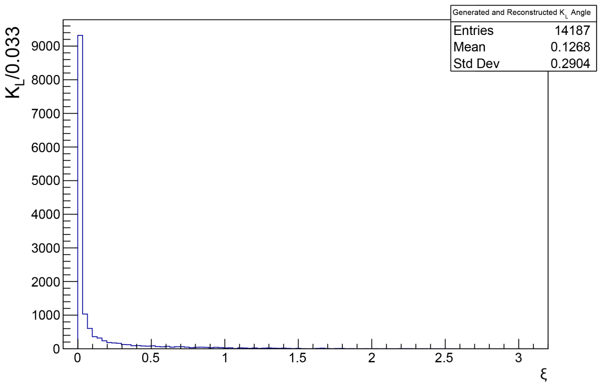

(a) The angle between the generated and reconstructed K_L vector (ξ)

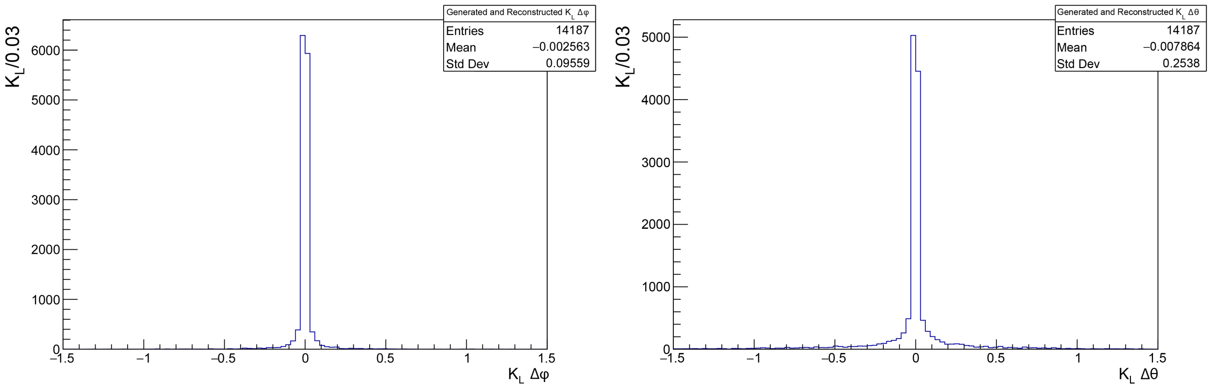

(b) $\phi^{gen}_{K_L} - \phi^{reco}_{K_L}$ **(c)** $\theta^{gen}_{K_L} - \theta^{reco}_{K_L}$

Figure 5.16.: The difference between the MC generated K_L angle and the reconstructed K_L angle, for all well-reconstructed events. (a) defines ξ as the angle between the generated K_L vector and the reconstructed K_L vector, (b) shows the difference in ϕ and (c) shows the difference in θ.

Figure 5.18 shows Figure 5.17 and 5.16 on the same plot. It can be seen that the angular separation of the reconstructed and generated K_L vector is, in general, much smaller than the angular separation of the generated K_L and the KLM cluster. The angle between the generated K_L and the reconstructed K_L momentum vector is on average much smaller than the angle between the generated K_L and the KLM cluster centroid, however the Belle II Technical Design report states that the K_L angular resolution for events with deposits only in the KLM is 3 degrees (0.06 radians).

The shape and number of energy deposits per cluster is currently being studied so that a more accurate determination of position and energy may be applied. This is part of the motivation for the analysis outlined in this thesis.

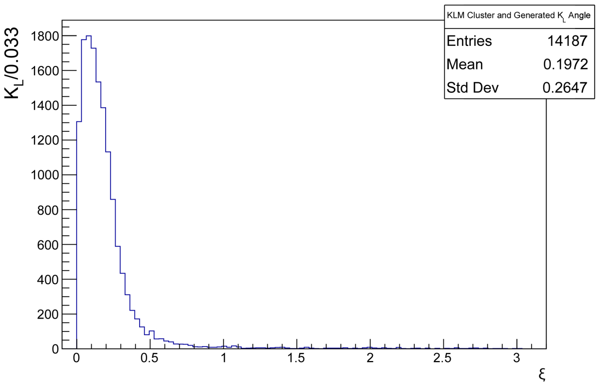

(a) Angular separation of the generated K_L and KLM cluster (ξ)

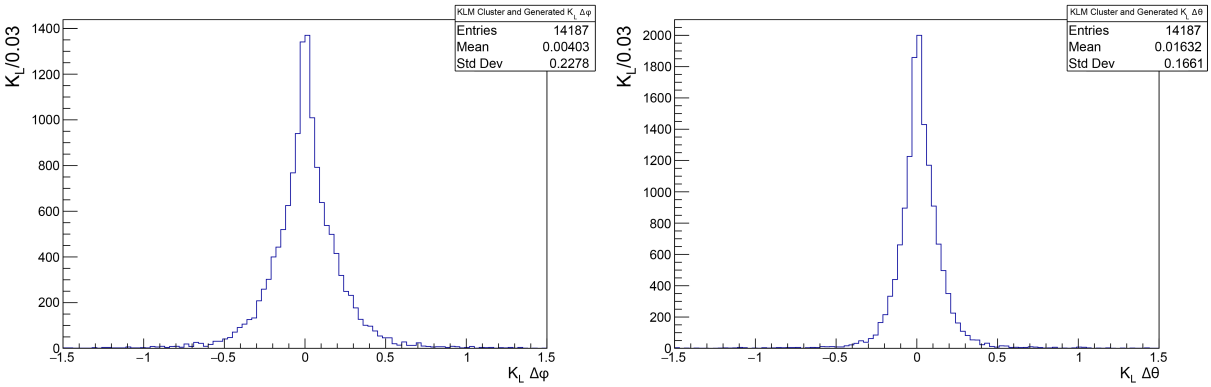

(b) $\phi^{gen}_{K_L} - \phi_{cluster}$ **(c)** $\theta^{gen}_{K_L} - \theta_{cluster}$

Figure 5.17.: The difference between the MC generated K_L angle and the KLM cluster closest to the reconstructed K_L 4-vector, for all well-reconstructed events. (a) defines ξ as the angle between the generated K_L vector and the KLM cluster, (b) shows the difference in ϕ and (c) shows the difference in θ.

5.8. Small $K_L K_S$ Opening Angle

The ϕ produced in this ISR process on average has a high momentum compared to particles in non-ISR processes. Since the ϕ mass is close to the mass sum of the kaon pair, the kaons will have low momenta in the ϕ rest frame. This means the kaon lab frame momentum is dominated by the ϕ meson boost, and so, the lab frame 4-vectors of the kaons will have a small angle between them. The pions decaying from the K_S, likewise, have small momenta in the K_S frame, so will have a small angular separation from the K_S vector. They will therefore also have a small angular separation from the K_L.

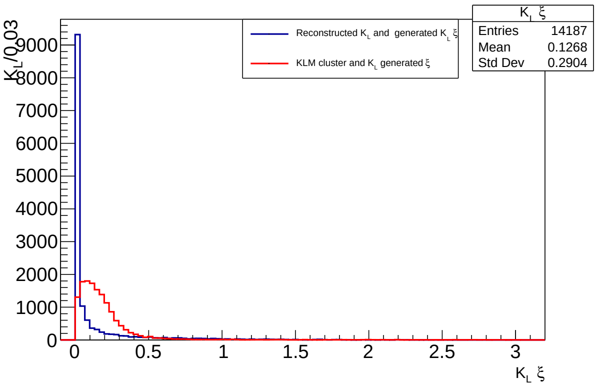

(a) Total angular separation (ξ)

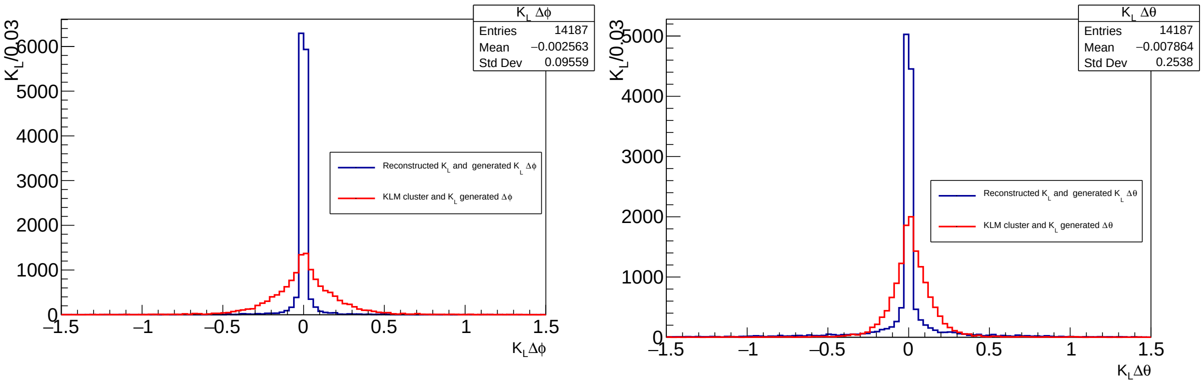

(b) $\Delta\phi$

(c) $\Delta\theta$

Figure 5.18.: The angular distance between the reconstructed K_L vector and the generated K_L vector (blue) and the closest KLM cluster (red). (a) shows the total angle (b) shows the separation in ϕ and (c) shows the separation in θ.

The issue associated with this is that one or both of the pions from the decay of the K_S may overlap with the KLM cells into which the K_L falls. If the pion leaves clusters in the same cell of the KLM, it is then likely very difficult to separate the resultant clusters of the K_L from those caused by the pions. Even though the pions are likely to only leave clusters in the first one or two layers of the KLM, the first two layers will likely be important if timing information is what will be used to measure K_L energy. If an overlapping pion were to not leave any clusters in the KLM, there is no way to know whether the KLM clusters seen are from the pion or K_L. Another issue is that the K_L identification process vetoes K_L candidates with a charged track entering the KLM within 15° of the KLM cluster.

Figure 5.19 shows the difference in the azimuthal angle and polar angle of the two generated kaons for a 3, 4 and 5.2 GeV E_{γ}^{CMS} cut. The distribution is indeed centred at zero with a very small average separation between the two.

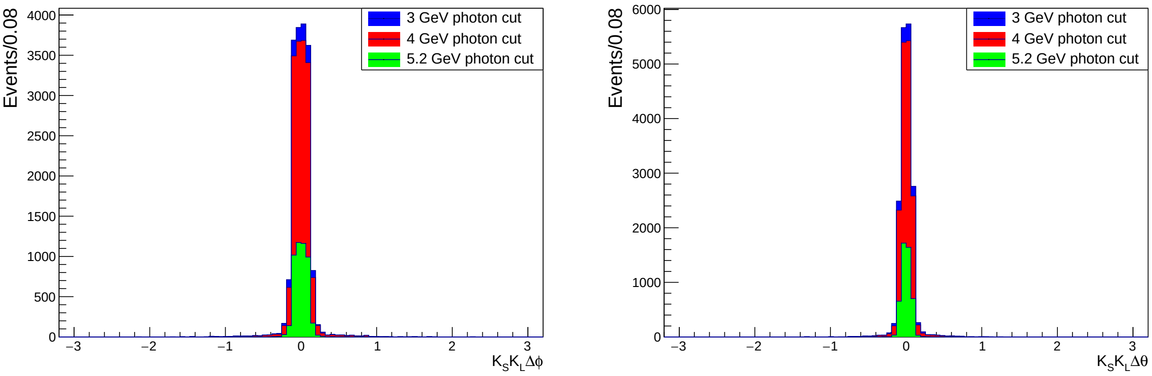

(a) Azimuthal angle ($\Delta\phi$). **(b)** Polar angle ($\Delta\theta_{lab}$).

Figure 5.19.: The MC generated angular separation between the K_S and the K_L in the lab frame.

Considering the kaon opening angle is not the full picture, the path of the pions must also be considered as well. The charged pions will not follow the straight path of their initial 4-momenta, as the neutral particles will; their path will be curved by the detector's magnetic field. The basf2 software in its current state does not provide the KLM entry point of the pions, so this information had to be determined in the following way.

The path of the pions is given by a helix offset from the origin by the decay vertex of the K_S. The (x, y, z) coordinates of the helix are given by Equations 5.8, 5.9 and 5.10, where the progression of the pion's path along the helix is parameterized by s [39]. (x_0, y_0, z_0) is the decay vertex of the K_S and so is also the initial position of the pion. In the $x - y$ plane, the pion moves in a circular motion. R is the radius of the cyclotron motion in the $x - y$ plane, given by Equation 5.11 where p_t is the relativistic, transverse momentum of the pion, B is the magnetic field strength and q is the magnitude of the charge. Φ_0 is the angle that describes the initial angular position on the circular path of the pion in the $x - y$ plane. $\Phi_0 = \frac{\pi}{2} + \arctan(p_y/p_x)$ where p_x and p_y are the x and y components of the pion's momentum. λ is the angle between the transverse and z momenta.

$$x(s) = x_0 + R[\cos\left(\Phi_0 + \frac{hs\cos(\lambda)}{R}\right) - \cos\Phi_0] \tag{5.8}$$

$$y(s) = y_0 + R[\sin\left(\Phi_0 + \frac{hs\cos(\lambda)}{R}\right) - \sin\Phi_0] \tag{5.9}$$

$$z(s) = z_0 + s\sin(\lambda) \tag{5.10}$$

$$R = \frac{p_t}{qB} \tag{5.11}$$

$h = \pm 1$, and is the parameter that defines the direction of rotation based on whether a π^+ or a π^- is being described. The magnetic field at Belle II points along the z axis and has a strength of 1.5 Tesla.

For each pion, the equation of the helix was solved for the value of s where $\sqrt{x(s)^2 + y(s)^2} =$ (radius of the KLM barrel) and for $z(s) =$ (the distance to the relevant endcap). Whichever resulted in a smaller value for s corresponded to the point where the pion entered the KLM. This was then used as the value for s which would give the coordinate position where the pion enters the KLM.

Mathematica was used to find the expression for s given $\sqrt{x^2 + y^2} =$ radius of the KLM [40]. The resulting expression was quite long so is shown in the appendix. If the helix never leaves the radius of the KLM for all s then this has no real solutions and instead, the pion will hit the endcap (assuming it does not go down the beam pipe). In these cases the value of s that gave z=(distance to the relevant endcap) was used.

To verify the validity of this method, the position of the pion cluster in the ECL was used. Testing both the z position and the radius of the cluster as inputs for determining s (as would be done with the radius and z coordinates of the KLM), the resulting predicted position vector was compared to the position vector of the cluster in ϕ, θ and radius, and found to be accurate. Plots of the difference between the angular values of the predicted helical position and the position of the ECL cluster are in the Appendix. The KLM dimensions are not included within the Belle II Technical Design Report. Instead this information was found by using the coordinates of the KLM clusters. The barrel radius was found by restricting the z coordinates to within the ECL barrel, so as to ensure that no endcap KLM clusters were in the sample, and then taking the minimum radius of the KLM cluster distribution. The z coordinates of the endcaps were found via the holes in the distribution due to the gaps between barrel and endcap. The KLM endcaps are at $z = (-200, 280)$cm, and the barrel has a radius of $r = 200$cm. Using this as the input for determining s, the position where the pions enter the KLM was determined. Figure 5.20 (a) shows the angle between the generated K_L vector and the determined intersection point of the pion's helical path with the KLM. Figure 5.20 (b) shows the difference in θ between the K_L and the pion's determined entrypoint of the KLM, and Figure 5.20 (c) shows the difference in ϕ. In Figure 5.20 (c), the two peaks either side of the origin are due to the magnetic field bending the oppositely charged pions in opposite directions in ϕ.

To determine if the pions were too close to the K_L to produce a well-reconstructed event, an angular veto was performed, requiring that the event have both K_S daughter pions intersect with the KLM at least 15° away from the generated K_L 4-vector. 15° was chosen because this is the cut that is applied to the K_L candidates during the charged track veto performed at Belle II. Table 5.3 shows the number of events that pass this veto for varying E_γ^{CMS} cuts. For a 3 GeV E_γ^{CMS} cut, 52% of all previously well-reconstructed events were vetoed, leaving an expected efficiency of $1.36 \pm 0.03\%$.

Table 5.3.: Events vetoed by pion and MC generated K_L overlap for different E_γ^{CMS} cuts. The fraction vetoed and efficiency show the Poisson uncertainties. The event is vetoed if the generated K_L 4-vector is less than 15° from the pion's predicted entry point of the KLM.

ISR Energy Cut	events before veto	events that pass veto	fraction vetoed	ϵ
3 GeV	14 187	6 816	$(52 \pm 1)\%$	$(1.36 \pm 0.03)\%$
4 GeV	13 310	6 293	$(53 \pm 1)\%$	$(1.26 \pm 0.03)\%$
5 GeV	8 702	3 865	$(56 \pm 2)\%$	$(0.773 \pm 0.02)\%$
5.2 GeV	3677	1567	$(57 \pm 2)\%$	$(0.313 \pm 0.01)\%$

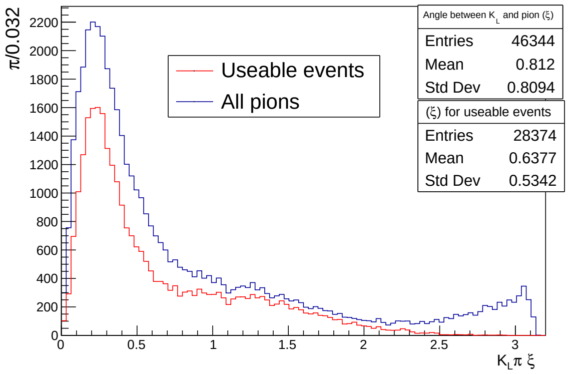

(a) The total angle between generated K_L vector and pion

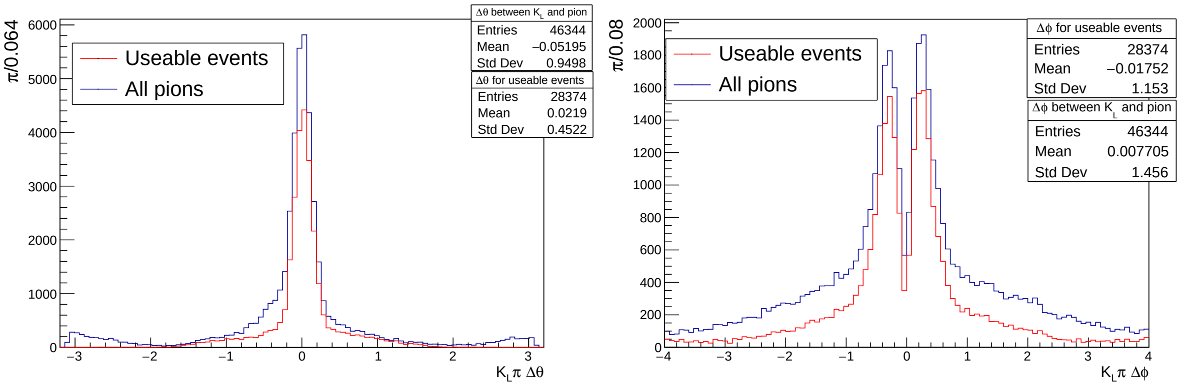

(b) Difference in θ between the MC generated K_L and pion

(c) Difference in ϕ between the MC generated K_L and pion

Figure 5.20.: The angular difference between the generated K_L and the intersection of the pion's predicted path with the KLM, (a) defines ξ as the total angle between the pion and KLM, (b) shows the difference in θ and (c) shows the difference in ϕ. The blue distribution is for K_S daughter pions from all correctly reconstructed K_S and the red distribution is for K_S daughter pions in all well-reconstructed events.

The same veto was tested using the nearest KLM cluster to the generated K_L instead of the generated K_L vector itself. Table 5.4 shows the number of events that pass the KLM cluster pion overlap veto.

The number of well-reconstructed events vetoed by using the closest KLM cluster method was found to be consistently lower than, but within Poisson fluctuations of, those results from the method using the generated K_L vector for the veto. The events in Table 5.3 and 5.4 include those removed by the previously mentioned upper K_L energy cut. The behaviour of the the pion cut once the upper K_L energy cut was implemented

Table 5.4.: Events vetoed by pion overlapping with the K_L KLM cluster, for different E_γ^{CMS} cuts. The fraction vetoed and efficiency both show the uncertainties due to Poisson fluctuations. The event is vetoed if the closest KLM cluster to the K_L 4-vector is less than 15 degrees from the pion's predicted entry point of the KLM.

ISR Energy Cut	events before veto	events that pass veto	fraction vetoed	ϵ
3 GeV	14 187	6 893	$(51 \pm 1)\%$	$(1.38 \pm 0.03)\%$
4 GeV	13 310	6 387	$(52 \pm 1)\%$	$(1.28 \pm 0.03)\%$
5 GeV	8 702	3 988	$(54 \pm 1)\%$	$(0.80 \pm 0.02)\%$
5.2 GeV	3677	1638	$(55 \pm 1)\%$	$(0.327 \pm 0.01)\%$

is shown in Table 5.5. After the upper K_L energy cut, for a 3 GeV E_γ^{CMS} cut, 54% of all well-reconstructed events (that were below the upper K_L energy cut) were vetoed by the pion KLM cluster overlap, leaving an expected efficiency of $1.18 \pm 0.03\%$. This shows that the pion veto is more likely to remove the events with a lower K_L energy excess than the large excess events removed by the upper K_L energy cut.

The numbers in Table 5.5 are the final number of well-reconstructed events once all cuts and corrections were considered.

Table 5.5.: Events vetoed by pion overlapping with the K_L KLM cluster after the upper level E_{K_L} cut, for different E_γ^{CMS} cuts. The fraction vetoed and efficiency both show the uncertainties due to Poisson fluctuations. The event is vetoed if the closest KLM cluster to the K_L 4-vector is less than 15 degrees from the pion's predicted entry point of the KLM. These are the final numbers for well-reconstructed events after all cuts and corrections are applied.

ISR Energy Cut	events before veto	events that pass veto	fraction vetoed	ϵ
3 GeV	12 937	5 926	$(54 \pm 1)\%$	$(1.18 \pm 0.03)\%$
4 GeV	12 319	5 613	$(54 \pm 1)\%$	$(1.12 \pm 0.03)\%$
5 GeV	8 341	3 698	$(56 \pm 1)\%$	$(0.740 \pm 0.02)\%$
5.2 GeV	3558	1 541	$(57 \pm 2)\%$	$(0.308 \pm 0.01)\%$

There are two possible analysis options in regards to the pion veto. The cluster veto may be used to select for events where the pion and K_L are likely not to interfere in the KLM, and can be separately considered for the purpose of isolated K_L calibration, however, if the constituents of the cluster may be considered separately; then a softer cut, using the generated/reconstructed K_L vector may be applied. This could be used to select for events where the constituents of the KLM cluster may be caused by the pion. If the KLM cluster can be separated into hits caused by the K_L (using the reconstructed K_L vector as a discriminator) and hits caused by the pion, then these events may become well-reconstructed. This could also allow the study of the behaviour of the KLM in cases where different particles overlap, and even perhaps allow the development of a method of possible separation of the KLM cluster constituents. This was deemed outside the scope of this project but is a promising area for future work.

5.9. Summary

5.9.1. Expected K_L Energy and Angular Uncertainty

Figure 5.21 shows the final generated minus reconstructed energy for the well-reconstructed K_L after all the cuts and corrections discussed previously were applied. To estimate the size of the spread of this distribution, this plot was fitted with the sum of two gaussians restricted between ± 0.02 GeV. This can be seen in Figure 5.22. The width of the narrower gaussian was used as the estimate for the Root Mean Squared (RMS) of this distribution. This describes the spread of the peak. This is only shown for the case where $E_\gamma^{CMS} > 3$ GeV. The fitted plots for other E_γ^{CMS} cuts are displayed in the appendix. The fit here is not intended to imply that the distribution is a double gaussian, but is used to estimate the width of the peak[2]. The expected difference between the reconstructed energy for the K_L and the true energy, for $E_\gamma^{CMS} > 3$, is ± 5 MeV. Table 5.6 shows the expected K_L error determined via this method for E_γ^{CMS} cuts of 3, 4, 5 and 5.2 GeV.

Figure 5.23 shows the angle between the generated K_L momentum vector and the reconstructed K_L momentum vector. The majority of events populate the bins below 0.02 radians or 1.1°. This is smaller than the 3° resolution that the Belle II technical design report claims for K_L with deposits in the KLM and the 1.5° resolution for K_L with deposits in the KLM and ECL. This means that this channel will provide a sample of K_L with enough angular resolution to verify the K_L reconstruction's angular determination, however, the angle between generated and reconstructed K_L

---

[2] The $E_\gamma^{CMS} > 5.2$ GeV data was found to be better approximated with a single gaussian restricted between -0.013 and 0.018 GeV.

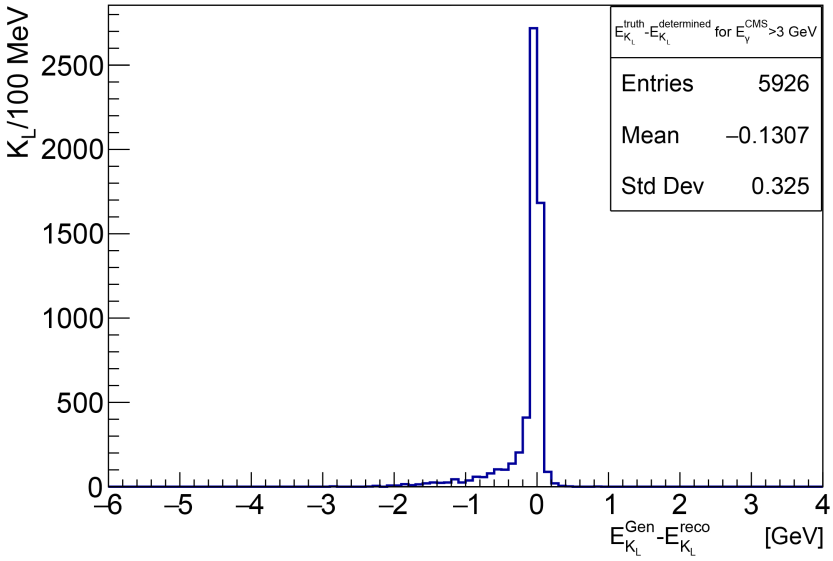

Figure 5.21.: $E_{K_L}^{gen} - E_{K_L}^{corrected}$ for $E_\gamma^{CMS} > 3$ GeV, with all previously discussed cuts and corrections applied to a sample of 500 000 events with beam background.

momentum vector is likely not small enough that this sample can be used to improve the angular resolution of the K_L reconstruction beyond the current level.

5.9.2. Expected Event Yield

After the K_L energy is corrected by adjusting the ISR photon CMS energy to 5.24 and requiring that each event have:

- An ISR photon in the CDC that passes the respective energy cut.
- A K_S in the reconstructed K_S list.
- A generated K_L within the KLM.
- $E_{K_L}^{reco} < e^{0.8\cos(\theta)} + 2.2$ GeV.
- Both of the pions used to construct the K_S entering the KLM at an angular distance greater than 15° away from the generated K_L.

The expected number of events useful for calibration and the expected K_L energy uncertainty is displayed in Table 5.6 for different E_γ^{CMS} cuts.

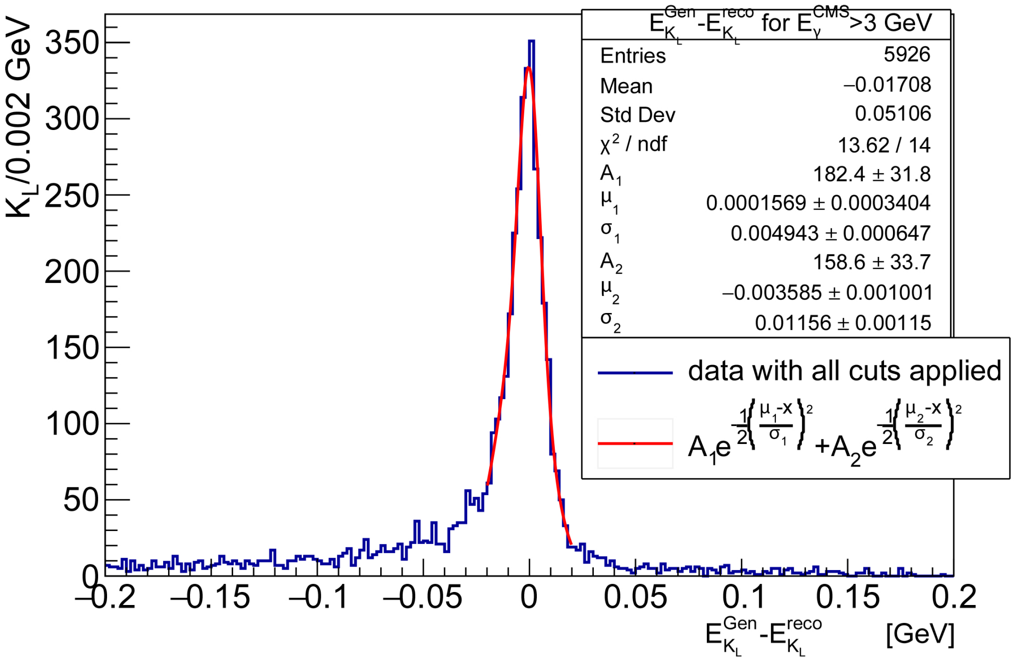

Figure 5.22.: $E_{K_L}^{gen} - E_{K_L}^{corrected}$ for $E_\gamma^{CMS} > 3$ GeV, with all cuts applied to a sample of 500 000 events with beam background. The distribution is fit with a double gaussian. The reduced $\chi^2 = 13.62/14$ per degree of freedom implying a good fit to the data. The width of the smaller gaussian (0.0049 ± 0.0006 GeV) is used as an estimate for the spread of the peak of this distribution.

Table 5.6.: Expected well-reconstructed events per fb^{-1} for different E_γ^{CMS} cuts.

E_γ^{CMS} cut	Expected Events per fb^{-1}	Estimated E_{K_L} Uncertainty
3 GeV	97	0.0049 GeV
4 GeV	92	0.0050 GeV
5 GeV	61	0.0055 GeV
5.2 GeV	25	0.0076 GeV

5.9.3. Effect of the Pion Veto on the K_L Energy Excess

A primary ISR event will contain a ϕ meson with a larger energy than a second order ISR event because the total energy is only divided between ϕ meson and the ISR photon. This means that the effect of the ϕ meson boost on the K_S daughter pions momentum is stronger for first order ISR, leading to, on average, a larger momentum for pions in first-order ISR events than second-order. A larger pion momentum means the path of the pion is curved less by the magnetic field and thus is separated less from

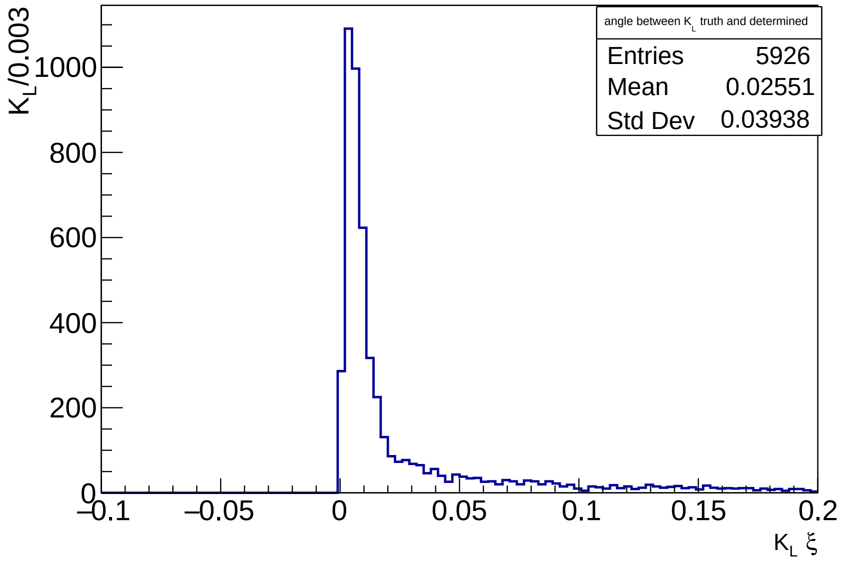

Figure 5.23.: The angle (ξ) between the generated K_L momentum vector and the reconstructed K_L momentum vector for $E_\gamma^{CMS} > 3$ GeV, with all previously discussed cuts and corrections applied to a sample of 500 000 events with beam background. The majority of events occupy the bins corresponding to an angle smaller than 0.02 radians or 1.1°.

the K_L. Because of this, the pion veto is more likely to remove primary ISR events that would have a low K_L energy excess and favours events such as back to back photon events, with a larger K_L excess. Due to this effect, the spread of the difference between K_L MC generated and reconstructed energy is larger once the pion veto is included. Before the pion veto was included, the spread of the distribution of $E_{K_L}^{gen} - E_{K_L}^{reco}$ was reduced as the E_γ^{CMS} cut was increased. Table 5.6 includes the pion veto, and shows that as the E_γ^{CMS} cut is increased, the estimated RMS increases. This is because the primary ISR events that the increased E_γ^{CMS} cut favours, are more likely to be vetoed by the pion kaon overlap than second order events that the lower cut allows into the sample. Given this effect the lower 3 GeV E_γ^{CMS} cut becomes the obvious choice, where before considering the pion veto, the larger E_γ^{CMS} cut seemed more attractive in terms of providing greater average K_L energy accuracy.

5.9.4. Final K_L $\cos(\theta)$ Distribution

The calibration of the detectors response to K_L will likely require that the barrel and endcaps are considered separately, due to the difference in geometry and design.

Figure 5.24 shows the final K_L $\cos(\theta)$ distribution for well-reconstructed events after all cuts and corrections are applied. The initial skew along the beam line that is present in the generated K_L $\cos(\theta)$ distribution for all events, although still present in the final well-reconstructed K_L sample, is less prominent, as the detector geometry and the cuts made throughout the analysis preferentially select for events with K_L in the barrel region. This evens out the $\cos(\theta)$ distribution of the K_L.

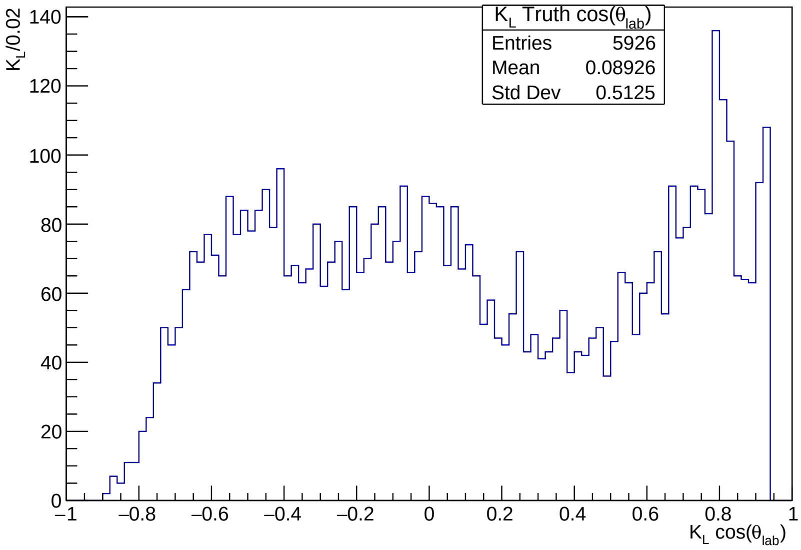

Figure 5.24.: The generated $\cos(\theta_{lab})$ distribution of K_L in the final sample of well-reconstructed events with all cuts and corrections applied, from the simulation of 500 000 ISR $K_S K_L$ events with beam background.

5.9.5. Comparison with Phase II Data

The purpose of this analysis was a feasibility study of this channel, but during 2018 a small sample of data was produced in the running of phase II. Although originally deemed out of scope, the cuts outlined here were tested on the recently released processing of the $472pb^{-1}$ of phase II data[3]. The simulation in this thesis indicates an expected 46 well-reconstructed events would be present in this sample. It was found that if only the relevant cuts made on the K_S and the ISR photon were applied (with a 3 GeV photon energy cut), and the K_L and the KLM clusters were not considered, that there were only 32 events. If it was required that the pions used to reconstruct the K_S

---

[3] The processing stored at KEK called prod5.

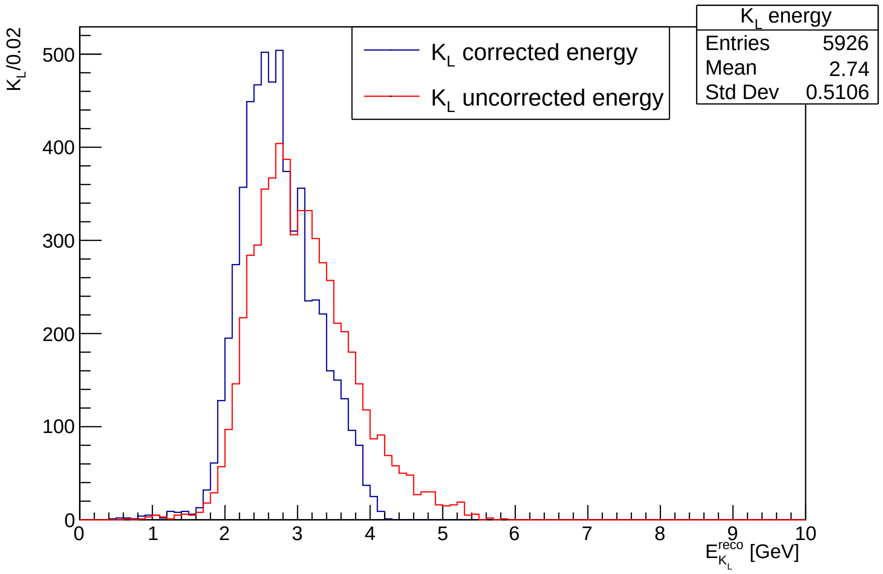

Figure 5.25.: The corrected and uncorrected K_L energy of the final sample of well-reconstructed K_L after all selections are applied.

not fall within 15 degrees of the KLM cluster closest to the reconstructed K_L vector, only 2 events remained.

The simulation estimates that requiring only a K_S and an ISR photon with more than 3 GeV in energy would result in 112 events, which is significantly more than the 32 events that were observed in the Phase II data. A likely reason for this, is the high level of beam background during Phase II. It is estimated that beam background in phase II was roughly of order 3 times the level that was expected, and so 3 times the nominal beam background in the ISR simulation presented here. This extra beam background would be expected to significantly reduce both the K_S and the ISR photon reconstruction efficiency, as was seen in the difference in photon and K_S reconstruction efficiency between the simulation of ISR with and without beam background presented in Chapter 4 of this thesis. This would explain the 32 events seen in data.

In the ISR simulation, if only the K_S and the ISR photon are considered, 112 events are expected in the phase II data, whereas considering the K_L and the pion veto as well, reduces the expected events for phase II to 46, removing roughly 60%.

Applying this same reduction to the 32 events observed with a K_S and a 3 GeV ISR photon would result in around 13 remaining events, but this assumes that the increased beam background has no effect on the KLM cluster formation and reconstruction. Two events is thus, not a totally unexpected yield, as the increased beam background would also likely affect the KLM cluster behaviour.

This implies that a reduction in beam background is particularly important for the this analysis. Methods of beam background reduction are currently being explored internally by the Belle II collaboration and it is likely that beam background levels in phase III onward will be lower than the level of beam background seen in phase II.

Concluding Remarks From the issues outlined in this section, it can be seen that this method of K_L calibration is mostly valuable for calibration in the energy range higher than that of the K_L produced by $B\overline{B}$ decays. The effect of the pion veto means that, where previously, the $E_\gamma^{CMS} > 5.2GeV$ cut yielded the most accurate energy determination, after the pion veto, the lower E_γ^{CMS} cuts result in a smaller spread of the difference between generated and reconstructed K_L energy. The efficiency is lower than would be hoped for and it can be inferred that the phase 2 data ($472pb^{-1}$) are not large enough to allow for a meaningful, accurate K_L calibration. In the future however, as Belle II produces more data, this method will become more viable.

Chapter 6.

Summary and Conclusion

6.1. Summary

The Belle II experiment is currently not well calibrated for the signatures from K_L mesons, which are left primarily in the KLM. The aim of this thesis was to determine the feasibility of the use of the ISR $K_S K_L$ channel as a source of K_L mesons for which the energy can be known. This channel is dominated by the ϕ meson resonance. By reconstructing the ISR photon and the K_S, then subtracting their 4-vectors from the initial state 4-vector, the K_L 4-vector may be in principal determined. To understand this process, two Monte-Carlo simulations of 500 000 events of ISR $K_S K_L$ production were produced with Phokhara and studied; one simulation with, and one without beam background. The $\cos(\theta)$ distribution of the the ISR photons, the K_S and the K_L, all had, on average, a trajectory close to the beam line. This meant that a majority of events contained at least one particle outside of the geometric acceptance of the detector.

This was further complicated by the presence of second order ISR, events where not one, but two ISR photons were emitted. These events comprised 64% of all simulated events. Assuming the $K_S K_L$ final state is produced via the ϕ resonance, in the frame of the centre-of-mass-system (CMS), a primary ISR photon has an energy of 5.24 GeV, corresponding to a ϕ and ISR photon with equal and opposite momentum. Second order ISR events fell into one of two categories: those where the ISR photons were emitted from the same incoming beam particle and had a combined CMS energy of 5.24 GeV, and those events where the ISR photons were back to back and emitted from a different particle beam. Back to back photon events are kinematically analogous to a three body decay of an initial state with the characteristics of an $\Upsilon(4S)$. In these events, the photons were able have a combined energy greater than 5.24 GeV and up to a combined energy of 9.56 GeV.

The presence of a second ISR photon further reduced the likelihood of reconstructing all particles, especially given the second order ISR photon's energy is on average low enough that the photon is hard to distinguish from beam background photons. This meant the second order ISR photons presented as missing photon energy. Accepting the loss of the second order photons, a 3 GeV cut on the photon CMS energy was found to be effective for, removing all of the photon candidates caused by beam background. Photon energy was also found to be lost via incomplete reconstruction of the EM shower that was used to determine that photon's energy. The combination of these two effects resulted in an excess in the predicted energy of the K_L when compared with the expected energy. It was found that by applying a minimum ISR CMS energy cut, the events with a low K_L energy excess could be isolated. This did however result in a significant loss of efficiency. Instead, to account for the photon loss, the photon energy was set to the expected value of 5.24 GeV in the CMS frame. This significantly reduced the K_L energy excess while allowing the use of second order events, which previously had a large K_L energy excess. This method was not effective at correcting the energy for the events with back to back photons. These events returned a K_L energy value that was significantly higher than the expected value. Given the high returned energy of these large K_L energy excess events, an upper level cut on the reconstructed K_L energy was able to remove many of the large K_L energy excess events. To compensate for the asymmetric lab frame energy of the system, and therefore the different upper level of final state K_L energy for different K_L polar angle in the lab frame (θ_{lab}), the upper level cut on reconstructed K_L energy was made as a function of the K_L $\cos(\theta_{lab})$.

The K_L energy distribution of events well-reconstructed for calibration was found to be higher than the average expected energy from K_L in B meson decays at Belle II. Higher energy K_L than the average K_L produced at Belle II are present in decays with the K_L higher in the decay chain, $B \to J/\psi K_L$ for example, but even for this decay channel, the majority of the K_L energy distribution still does not overlap with those produced in ISR $K_S K_L$ events.

The high average energy of the ϕ meson meant that the opening angle between the kaons and, subsequently, the opening angle between the K_S daughter pions and the K_L was found to be quite small. This presented an issue in that if the pions produced by the K_S decay were to overlap with the K_L in the KLM, then it would likely be difficult to separate the KLM clusters from the pions from those caused by the K_L. This would also likely result in a veto of the KLM cluster from being identified as a K_L candidate, due to the charged track of the pion being too close to the KLM cluster.

To predict the effect of this, the pions' helical path was extrapolated out to the KLM and then a cut was applied, requiring that the pion enter the KLM no closer than 15° away from the generated K_L vector. This vetoed 52% of well-reconstructed events for the case of the 3 GeV E_γ^{CMS} cut. The same veto was then applied, but to the nearest KLM cluster to the K_L vector, resulting in a similar veto rate. This was performed before the upper level cut on the reconstructed K_L energy was applied. When the K_L energy cut was included, it was found that the pion veto removed 54% of the well-reconstructed events that had already passed the K_L energy cut, leaving a final efficiency of $(1.18 \pm 0.03)\%$ of events well-reconstructed for calibration out of the total events produced, with a reconstructed K_L energy accurate to of order ± 5 MeV.

6.2. Future Work

6.2.1. KLM Cluster Study

Whether one wishes to apply the pion veto on the KLM cluster or on the K_L vector depends on whether one can separate out the detector hits that comprise the cluster or not. If one wishes to study the KLM response to K_L, independent of the pion effect, then the cluster veto would be used to ensure that the K_L alone is being studied. With the ISR sample, a study of the effects of an overlapping K_L and pion (whose momentum can be reconstructed from the charged track) could be conducted. This could help develop a better understanding of the shape of KLM clusters that originate from events with overlapping particles, perhaps allowing for the development of a method of separation of the cluster hits that result from different particles.

6.2.2. Upper K_L Energy Cut

Although the upper level cut on the K_L energy described in the previous chapter effectively removes events with a large excess in reconstructed K_L energy, it may be possible to separate this sample and correct the excess in K_L energy. Some attempt was made to do this, but the difference between generated and reconstructed K_L energy for these events was always found to be, on average, too large to be useful. To continue working on this would be particularly advantageous to this method of calibration, as these events have a true K_L energy that is generally lower than the K_L in the rest of the ISR $K_S K_L$ sample, and thus, would be suitable for calibrating the lower energy region that more aligns with K_L seen in $B\overline{B}$ decays at Belle II.

6.3. Conclusion

The initial goal of this project was to determine if the ISR $K_S K_L$ channel would provide a sample of K_L, with known energy and direction, that could be used for calibration of the Belle II detector's response to K_L. At the beginning of this project, the available K_L reconstruction algorithm was based on the Belle K_L reconstruction algorithm which only provided the K_L directional information. The Belle K_L reconstruction was not able to provide useful information about the K_L energy. This was because the number of hits in a cluster is not an accurate indicator of the energy of the associated K_L (the number of hits in a cluster is the discriminating variable used for measuring energy in ECL clusters) [1].

Members of the Belle II collaboration have been working on developing a new K_L reconstruction algorithm using the Belle II simulated data, but at the time of writing, have presented no significant, tangible solutions. Currently the K_L reconstruction is not considered reliable. This will likely change as more time is spent by the collaboration working on K_L reconstruction. A variety of approaches are being explored as possible ways of classifying KLM cluster formation, but to be properly validated, these methods require a dataset of real events on which they can be tested. Whether the ISR $K_S K_L$ channel provides enough such events depends on how many of these events are required for the chosen approach.

After all cuts and corrections, the efficiency of ISR $K_S K_L$ events, useable for calibration, was found to be of order 1% with an angular determination accurate to of order 1.1°, which is more accurate than the KLM cluster centroid; and an expected difference between generated and reconstructed K_L energy of order ± 5 MeV. The $\cos(\theta_{lab})$ distribution that the K_L are produced in is highly skewed towards the beam line i.e. the extremes of $\cos(\theta_{lab})$. The cuts made on the sample select for events with a

K_L in the barrel region, so the final sample of well-reconstructed K_L has a more even distribution of K_L in the barrel and endcaps.

One of the initial goals for this analysis was to be able to calibrate using the data from phase II running of Belle II, which occured in 2018. The expected integrated luminosity was 30 fb^{-1} so this may have been possible, however, phase II under-delivered and was only able to produce $472pb^{-1}$ of luminosity, which for the determined efficiency of 1.18% corresponds to around 50 expected well-reconstructed events for a $E_{\gamma}^{CMS} > 3$ GeV cut. This is clearly not enough for a meaningful calibration. Had the expected 30 fb^{-1} of luminosity been produced in phase II, then this would have corresponded to 2910 events. By the end of 2019, the Belle II experiment is expected to have produced 100 fb^{-1} of data which corresponds to an expected 9700 well-reconstructed ISR K_SK_L events and by the end of the total run of Belle II there is expected to be 50 ab^{-1} of data which corresponds to 4.85 million well-reconstructed events. It can be confidently stated that 4.85 million events is more than enough data to ensure that insufficient statistics will not be the limiting factor in a K_L calibration.

How long until there is sufficient data to effectively calibrate depends both on what kind of calibration will be carried out and how accurate the calibration must be, as the amount of data will likely determine the level of possible refining of the K_L reconstruction algorithm in question. It is known that to measure the energy of a K_L, simply counting hits in a cluster is insufficient. The use of a kinematic calibration, which uses the time difference between the first and last hit in a cluster to derive the gamma factor of the associated K_L, is currently being explored within the collaboration. This method, while likely effective when possible, depends on having multiple deposits so as to provide multiple space-time measurements of the K_L. Given the low interaction rate of the K_L, this is not always the case. Depending on the channel being studied, the K_L production vertex may be used as a second, space-time coordinate. This would likely only work for events where the K_L is early in the decay chain, and produced close in time and position to the interaction point. These kinds of K_L are also likely to be higher in energy and therefore closer to the energy range for which the ISR K_SK_L channel is best at calibrating.

Another alternative for the determination of K_L energy and angle is the use of a machine learning algorithm for classifying K_L based on cluster shape and formation. A machine learning algorithm requires a sample of K_L with known energy that can be used to train the algorithm to be able to recognize and classify K_L energy based on the shape and timing information of the cluster. This method also requires a separate sample for testing the trained algorithm. As such, it is likely that this method will require a much larger dataset than a kinematic calibration. Monte-Carlo generated K_L can be used to train machine learning algorithms, but this depends on the accuracy of the simulation of these K_L, which is not necessarily reliable, and so a sample of K_L in real data is preferable.

To improve the detector's angular determination of K_L with the ISR $K_S K_L$ channel is less likely to be fruitful than for energy determination. The Belle II Technical Design Report states that there is already an angular resolution of 3° for K_L with deposits in just the KLM and 1.5° for K_L with a deposits in the KLM and ECL. The average angle between the true K_L vector and the reconstructed K_L vector, 1.1°, is a similar size to the current resolution. Any attempt at K_L angular calibration with this method will likely not be able to improve on the current angular resolution, as the K_L vectors in the sample used to calibrate would need to be known to a much greater resolution than the current K_L reconstruction method to be able to significantly improve that method. The ISR $K_S K_L$ sample will however, be able to serve as a sample for validation of the current K_L reconstruction's angular resolution.

The events vetoed by the presence of a pion overlapping with the K_L cluster are a significant concern, vetoing roughly half of the otherwise well-reconstructed events. This effect further increases the need for a larger dataset. If one were able to develop a method of separating the KLM hits caused by the pion from those associated with the K_L, then the well-reconstructed dataset would increase significantly. These vetoed events could perhaps even be used as a sample for the development of a method of separating hits in a KLM cluster caused by two different particles.

Due to the higher than expected level of beam background during the running of phase II, the preliminary study of the phase II data conducted in this thesis yielded significantly fewer well-reconstructed events than the expected number. Moving forward, reducing beam background will likely be of particular importance to the feasibility of this analysis.

Demonstrated here are the primary issues associated with using the ISR $K_S K_L$ channel for K_L calibration: the high energy range in which we expect the K_L to be produced and the low efficiency, which when combined with the pion K_L overlap veto leads to a low number of well-reconstructed events. While the phase II data may not be sufficient to carry out this calibration, as more data is produced, the use of this channel for the development of a K_L calibration becomes more realistic.

Appendix A.

Appendix

A.1. Lab Frame E_γ Cut

The decision to use the CMS energy of the photon and not the lab frame energy was due to the approach of starting at a 5.2 GeV CMS cut and then reducing this threshold. From the plots in Chapter 3, Figure 4.7, it might seem like a lab frame cut would result in a higher efficiency whilst still removing all beam background. After all of the cuts and corrections, the differences in final yield is negligible.

Requiring a reconstructed K_S and ISR photon and a K_L in the KLM, the yield is 14 187 events for the CMS γ cut and 14148 events for the lab frame cut. When the $e^{0.8\cos(\theta)} + 2.2$ GeV upper level cut on determined K_L energy is applied the yield is 12 984 events for the CMS γ cut and 12 960 for the lab Frame. These numbers are within poisson fluctuations. Even though from Figure 4.7 it would appear that a lab frame cut would result in a higher photon efficiency, when other cuts are taken into account this cut results in a negligible difference.

Figure A.1.: T$E_{K_L}^{truth} - E_{K_L}^{corrected}$ for different E_γ^{CMS} cuts, with all cuts and corrections applied to a sample of 500 000 events with beam background. The distribution is fit with a double gaussian restricted between ± 0.02 GeV. The fit parameters are displayed in the upper right window. The reduced χ^2 is a measure of the goodness of the fit. For the $E_\gamma^{CMS} > 5.2$ GeV case, it was found that a single gaussian restricted from -0.013 GeV to 0.018 GeV provided a better fit, so this is used.

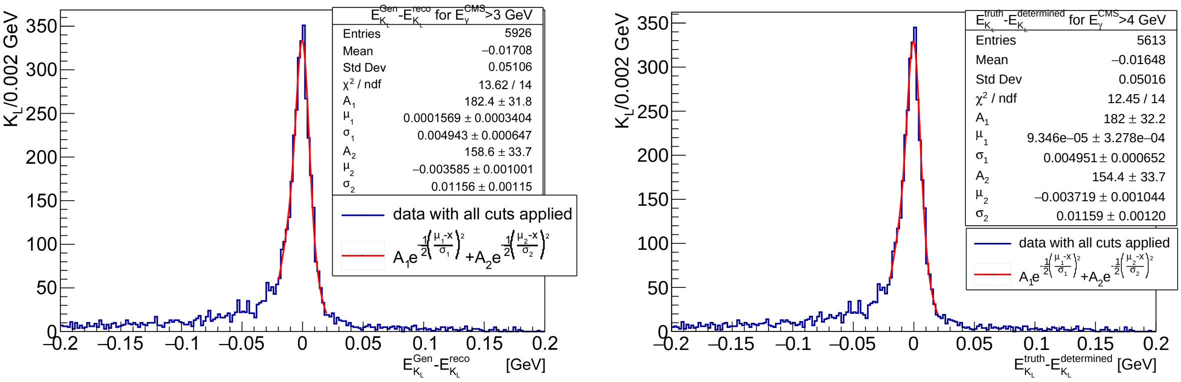

(a) 3 GeV ISR CMS cut

(b) 4 GeV ISR CMS cut

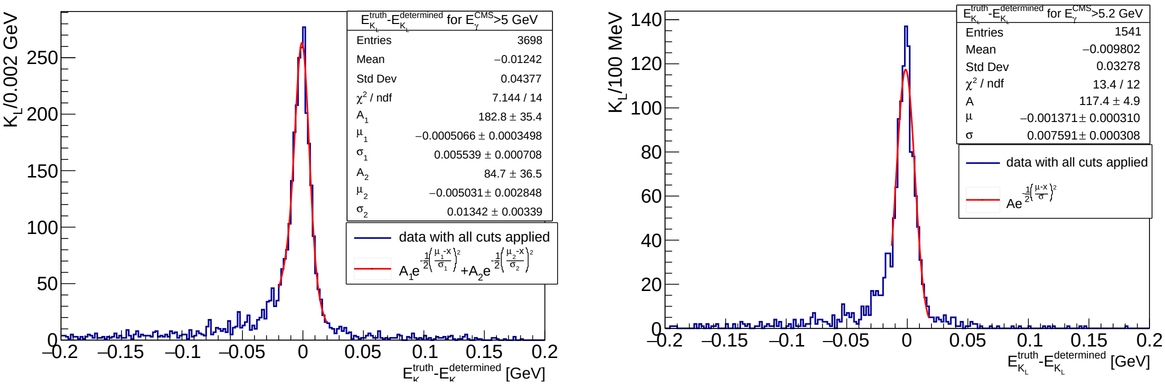

(c) 5 GeV ISR CMS cut

(d) 5.2 GeV ISR CMS cut

A.2. Plots of the Double Gaussian Fit for Other E_γ^{CMS} Cuts

A.3. Pion KLM Entry Point

The set of parameterized helical equations in section 5.8 were solved for the value of the parameter s that gave a specific radius m. This was done with Mathematica [40].

So that these equations may fit on a page, K is defined by equation A.3. If $K > 0$ then there are four real solutions for s, two of these being negative. Requiring real positive solutions for s (as s is analogous to a time variable), the solution that gives the smallest value of s is the one chosen. In the $x - y$ plane, these solutions give the intersection of two circles, the circular pion path and the circular inner radius of the KLM. The larger solution corresponds to the point where, after intersecting with the KLM, the helical path intersects with the KLM inner radius a second time. Equation A.1 is the solution for the π^+ and Equation A.2 is the solution for the π^- (noting $h = -1$ for the π^+ and $h = 1$ for the π^-).

$$K=-(y_0\cos(\Phi_0)-x_0\sin(\Phi_0))^2\left(x_0^4+2y_0^2x_0^2-2m^2x_0^2+2R^2x_0^2-4y_0R\sin(\Phi_0)x_0^2-4\left(x_0^2+y_0^2-m^2\right)R\cos(\Phi_0)x_0+\right.$$
$$\left.4\,y_0R^2\sin(2\Phi_0)x_0+y_0^4+m^4-2y_0^2m^2+2y_0^2R^2-4m^2R^2+2\left(x_0^2-y_0^2\right)R^2\cos(2\Phi_0)-4y_0^3R\sin(\Phi_0)+4y_0m^2R\sin(\Phi_0)\right)$$

$$s=\frac{R\cos^{-1}\left(\frac{2x_0^2R\cos^2(\Phi_0)-x_0\left(x_0^2+y_0^2-m^2+4R^2-4y_0R\sin(\Phi_0)\right)\cos(\Phi_0)+2y_0^2R\sin^2(\Phi_0)-y_0\left(x_0^2+y_0^2-m^2+4R^2\right)\sin(\Phi_0)+R\left(x_0^2+y_0^2-m^2+2R^2-\sqrt{\frac{K}{R^2}}\right)}{2R\left(x_0^2-2R\cos(\Phi_0)x_0+y_0^2+R^2-2y_0R\sin(\Phi_0)\right)}\right)}{hL} \tag{A.1}$$

$$s=-\frac{R\cos^{-1}\left(\frac{2x_0^2R\cos^2(\Phi_0)-x_0\left(x_0^2+y_0^2-m^2+4R^2-4y_0R\sin(\Phi_0)\right)\cos(\Phi_0)+2y_0^2R\sin^2(\Phi_0)-y_0\left(x_0^2+y_0^2-m^2+4R^2\right)\sin(\Phi_0)+R\left(x_0^2+y_0^2-m^2+2R^2+\sqrt{\frac{K}{R^2}}\right)}{2R\left(x_0^2-2R\cos(\Phi_0)x_0+y_0^2+R^2-2y_0R\sin(\Phi_0)\right)}\right)}{hL} \tag{A.2}$$

To test the validity of these equations, the position of the ECL cluster associated with the pion was used. Figures A.2 and A.3 show the angular difference between the position determined by the predicted helical path of the pion and the ECL cluster's position. Figure A.2 uses the cluster radius as an input and Figure A.3 uses the clusters z position as an input. This is because using the KLM radius and KLM endcap's z position is the input that this method uses to determine the KLM entry point. The spread of this angular difference is quite small and centred at zero, so it can be inferred that this method is accurate enough to determine the pion position in the KLM for the purposes of the pion kaon overlap veto.

The non-zero spread of the difference between predicted pion and cluster position is likely due to the spread of the ECL cluster. That is, the ECL cluster has some width, where the cluster position refers to the coordinates of the cluster centroid. In the basf2 system, the cluster position has an error variable associated with each coordinate, but this variable was found to be equal to 0 for all cases, which implies that this was not coded properly at the time of writing.

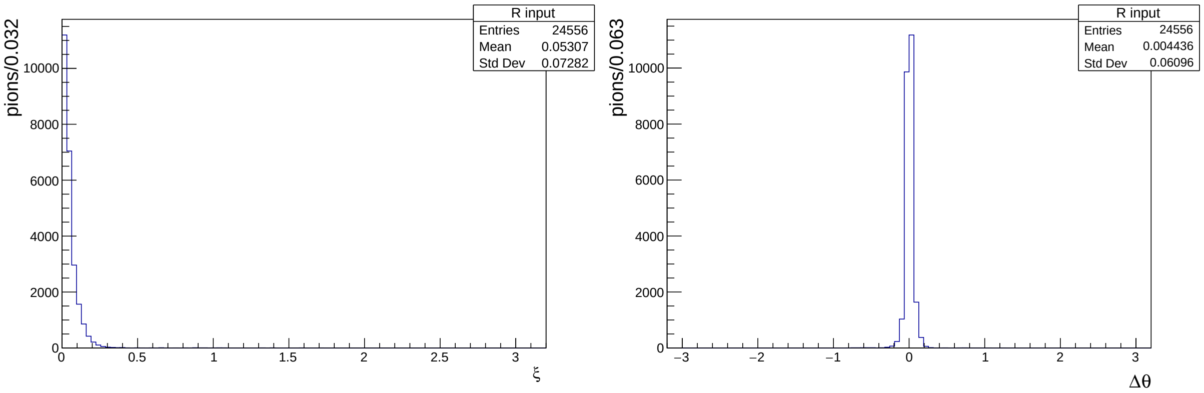

(a) Angle between cluster and predicted position.

(b) The difference in polar angle between cluster and predicted position.

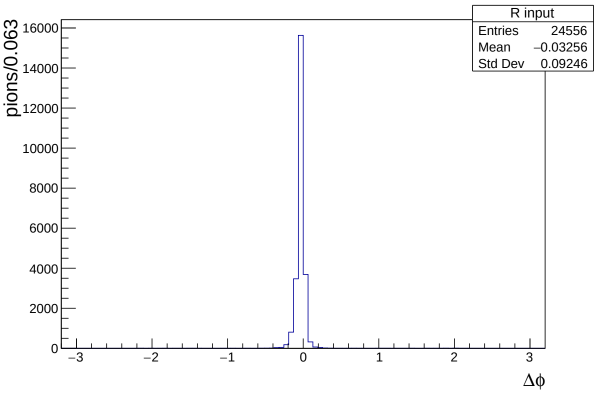

(c) The difference in azimuthal angle between cluster and predicted position.

Figure A.2.: The angular difference between the position of the pion's associated ECL cluster and the position determined via the helical equations of motion. These plots use the cluster radius as the input to find all coordinates. ξ is defined as the total angle between the true cluster position and the predicted position.

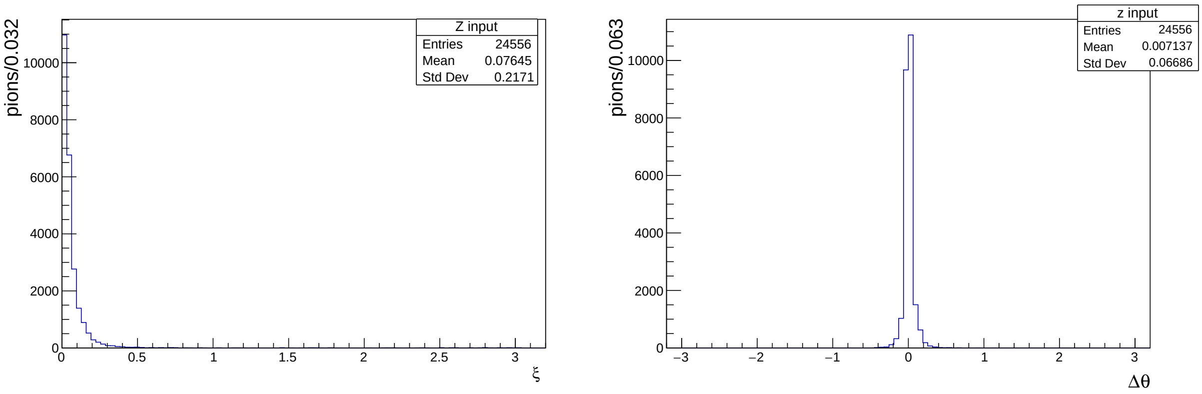

(a) Angle between cluster and predicted position.

(b) The difference in polar angle between cluster and predicted position.

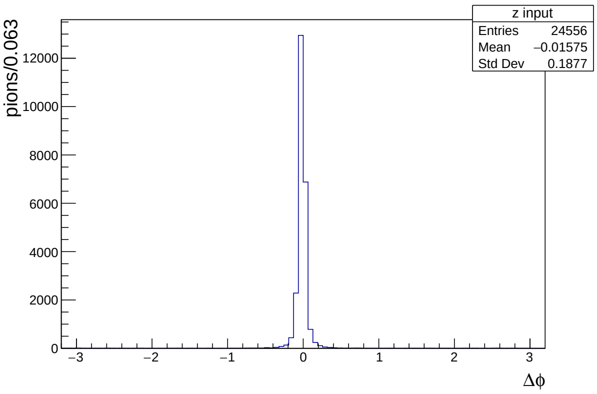

(c) The difference in azimuthal angle between cluster and predicted position.

Figure A.3.: The angular difference between the position of the pion's associated ECL cluster and the position determined via the helical equations of motion. These plots use the cluster z position as the input to find all coordinates. ξ is defined as the total angle between the true cluster position and the predicted position.

Colophon

This thesis was made in LaTeX 2$_\varepsilon$ using the “hepthesis” class [**?**].

Bibliography

[1] Belle-II, T. Abe *et al.*, Belle II Technical Design Report, (2010), physics.ins-det/1011.0352.

[2] H. CzyÅij, M. Gunia, and J. H. KÃijhn, Simulation of electron-positron annihilation into hadrons with the event generator PHOKHARA, JHEP **0**8, 110 (2013), hep-ex/1306.1985.

[3] GEANT4, S. Agostinelli *et al.*, GEANT4: A Simulation toolkit, Nucl. Instrum. Meth. **A**506, 250 (2003).

[4] A. Moll, The software framework of the Belle II experiment, J. Phys. Conf. Ser. **3**31, 032024 (2011).

[5] A. Ryd *et al.*, EvtGen: A Monte Carlo Generator for B-Physics, (2005).

[6] R. Brun and F. Rademakers, ROOT: An object oriented data analysis framework, Nucl. Instrum. Meth. **A**389, 81 (1997).

[7] Belle, BaBar, G. Marchiori, Search for CP violation and new physics in rare B decays at the B factories, in *Proceedings, 10th Conference on Flavor Physics and CP Violation (FPCP 2012): Hefei, Anhui, China, May 21-25, 2012*, 2012, hep-ex/1208.5614.

[8] G. Ciezarek *et al.*, A Challenge to Lepton Universality in B Meson Decays, Nature **5**46, 227 (2017), hep-ex/1703.01766.

[9] Belle, K. Abe *et al.*, Measurement of CP violation parameter $sin^2(\phi_1)$ with 152 million B anti-B pairs, in *Proceedings, 21st International Symposium on Lepton and Photon Interactions at High Energies (LP 03): Batavia, ILL, August 11-16, 2003*, 2003, hep-ex/0308036.

[10] Heavy Flavor Averaging Group, Y. Amhis *et al.*, Averages of b-hadron, c-hadron, and τ-lepton properties as of summer 2016, Eur. Phys. J. **C**77,

895 (2017), hep-ex/1612.07233, updated results and plots available at https://hflav.web.cern.ch.

[11] E. Noether, Invariant Variation Problems, Gott. Nachr. **1**918, 235 (1918), physics/0503066, [Transp. Theory Statist. Phys.1,186(1971)].

[12] H. YUKAWA, On the interaction of elementary particles. I, Nippon Sugaku-Buturigakkwai Kizi Dai 3 Ki **17**, 48 (1935).

[13] S. H. Neddermeyer and C. D. Anderson, Note on the nature of cosmic-ray particles, Phys. Rev. **51**, 884 (1937).

[14] C. M. G. Lattes, H. Muirhead, G. P. S. Occhialini, and C. F. Powell, PROCESSES INVOLVING CHARGED MESONS, Nature **1**59, 694 (1947), [,42(1947)].

[15] D. J. Griffiths, *Introduction to elementary particles; 2nd rev. version*Physics textbook (Wiley, New York, NY, 2008).

[16] G. Arnison *et al.*, Experimental observation of isolated large transverse energy electrons with associated missing energy at s=540 gev, Physics Letters B **122**, 103 (1983).

[17] M. Banner *et al.*, Observation of single isolated electrons of high transverse momentum in events with missing transverse energy at the cern pp collider, Physics Letters B **122**, 476 (1983).

[18] ATLAS, G. Aad *et al.*, Observation of a new particle in the search for the Standard Model Higgs boson with the ATLAS detector at the LHC, Phys. Lett. **B**716, 1 (2012), hep-ex/1207.7214.

[19] CMS, S. Chatrchyan *et al.*, Observation of a new boson at a mass of 125 GeV with the CMS experiment at the LHC, Phys. Lett. **B**716, 30 (2012), hep-ex/1207.7235.

[20] R. Descartes*Principles of Philosophy* Vol. 1 (Cambridge University Press, 1985), .

[21] A. D. Sakharov, Violation of CP Invariance, C asymmetry, and baryon asymmetry of the universe, Pisma Zh. Eksp. Teor. Fiz. **5**, 32 (1967), [Usp. Fiz. Nauk161,no.5,61(1991)].

[22] K. S. Babu *et al.*, Working Group Report: Baryon Number Violation, in *Proceedings, 2013 Community Summer Study on the Future of U.S. Particle Physics: Snowmass on the Mississippi (CSS2013): Minneapolis, MN, USA, July 29-August 6, 2013*, 2013,

hep-ph/1311.5285.

[23] S. D. Bass, Electroweak baryon number non-conservation and topological condensates in the early universe, Czech. J. Phys. **5**5, B619 (2005), hep-ph/0407245.

[24] V. A. Rubakov and M. E. Shaposhnikov, Electroweak baryon number nonconservation in the early universe and in high-energy collisions, Usp. Fiz. Nauk **1**66, 493 (1996), hep-ph/9603208, [Phys. Usp.39,461(1996)].

[25] Belle, BaBar, A. J. Bevan *et al.*, The Physics of the B Factories, Eur. Phys. J. **C**74, 3026 (2014), hep-ex/1406.6311.

[26] Particle Data Group, K. A. Olive *et al.*, Review of Particle Physics, Chin. Phys. **C**38, 090001 (2014).

[27] T. Kuhr, Flavor physics at the Tevatron, Springer Tracts Mod. Phys. **2**49, 1 (2013).

[28] LHCb, R. Aaij *et al.*, Measurement of CP violation in $B^0 \to J/\psi K_S^0$ decays, Phys. Rev. Lett. **1**15, 031601 (2015), hep-ex/1503.07089.

[29] BaBar, B. Aubert *et al.*, Observation of CP violation in the B^0 meson system, Phys. Rev. Lett. **8**7, 091801 (2001), hep-ex/0107013.

[30] V. Baier and V. Fadin, Radiative corrections to the resonant particle production., Phys. Lett., 27B: 223-5(July 8, 1968). .

[31] M. Benayoun, S. I. Eidelman, V. N. Ivanchenko, and Z. K. Silagadze, Spectroscopy at B factories using hard photon emission, Mod. Phys. Lett. **A**14, 2605 (1999), hep-ph/9910523.

[32] BaBar, J. P. Lees *et al.*, Cross sections for the reactions $e^+e^- \to K_S^0K_L^0$, $K_S^0K_L^0\pi^+\pi^-$, $K_S^0K_S^0\pi^+\pi^-$, and $K_S^0K_S^0K^+K^-$ from events with initial-state radiation, Phys. Rev. **D**89, 092002 (2014), hep-ex/1403.7593.

[33] BaBar, J. P. Lees *et al.*, Cross sections for the reactions $e^+e^- \to K_S^0K_L^0\pi^0$, $K_S^0K_L^0\eta$, and $K_S^0K_L^0\pi^0\pi^0$ from events with initial-state radiation, Phys. Rev. **D**95, 052001 (2017), hep-ex/1701.08297.

[34] S. F. Koch, Dial-A-State: Computation and Applications of Theoretical Particle Production Cross-Sections, 2015.

[35] B. Golob, Beauty and charm results from B-factories, in *Heavy quark physics. Proceedings, Helmholtz International School, HQP08, Dubna, Russia, August 11-21,*

2008, pp. 123–144, 2009, hep-ex/0901.1443.

[36] V. Aulchenko *et al.*, Electromagnetic calorimeter for Belle II, in *Journal of Physics: Conference Series* Vol. 587, 2015.

[37] C. Bernardini *et al.*, Lifetime and beam size in a storage ring, Phys. Rev. Lett. **10**, 407 (1963).

[38] E. Kou *et al.*, The Belle II Physics book, (2018), hep-ex/1808.10567.

[39] F. Ragusa, An introduction to charged particles tracking, http://www0.mi.infn.it/ ∼ ragusa/tracking_sns_28.05.2014.pdf .

[40] W. R. Inc., Mathematica, Version 11.3, Champaign, IL, 2018.

List of figures

List of tables